ICARUS 103, 163–214 (1993)

# Geometry of the Saturn System from the 3 July 1989 Occultation of 28 Sgr and Voyager Observations

RICHARD G. FRENCH,[1] PHILIP D. NICHOLSON,[2] MAREN L. COOKE,[3] J. L. ELLIOT,[3,4] KEITH MATTHEWS,[5] OLGA PERKOVIĆ,[2] ERIC TOLLESTRUP,[6] PAUL HARVEY,[7] NANCY J. CHANOVER,[8] MARY ANN CLARK,[9] EDWARD W. DUNHAM,[10] WILLIAM FORREST,[11] JOSEPH HARRINGTON,[3] JUDITH PIPHER,[11] ANDRÉ BRAHIC,[12] ISABELLE GRENIER,[12] FRANÇOISE ROQUES,[12] AND MARTINA ARNDT[6]

[1]*Astronomy Department, Wellesley College, Wellesley, Massachusetts 02181;* [2]*Astronomy Department, Cornell University, Ithaca, New York 14853;* [3]*Department of Earth, Atmospheric, and Planetary Sciences, Massachusetts Institute of Technology, Cambridge, Massachusetts 02139;* [4]*Department of Physics, Massachusetts Institute of Technology, Cambridge, Massachusetts 02139;* [5]*Palomar Observatory, California Institute of Technology, Pasadena, California 91125;* [6]*Smithsonian Astrophysical Observatory, Center for Astrophysics, Harvard University, Cambridge, Massachusetts 02138;* [7]*Astronomy Department, University of Texas, Austin, Texas 78712;* [8]*Astronomy Department, New Mexico State University, Las Cruces, New Mexico 88001;* [9]*Department of Art, Kansas State University, Manhattan, Kansas 66506;* [10]*NASA Ames Research Center, Moffett Field, California 94035;* [11]*Department of Astronomy, University of Rochester, Rochester, New York 14627; and* [12]*Observatoire de Paris, F92195, Meudon, France*

Received August 31, 1992; revised March 1, 1993

Observations of the 3 July 1989 Saturn occultation of 28 Sgr are combined with Voyager 1 and 2 occultation measurements to determine Saturn's pole direction and the radius scale for the ring system. Measurements of event times for circular ring features are presented for 3.9-$\mu$m imaging measurements from the Palomar 5-m telescope, 2.1-$\mu$m imaging measurements using the McDonald Observatory 2.7-m telescope, 3.3-$\mu$m imaging results (Harrington *et al.* 1993, this issue) from the NASA Infrared Telescope Facility and 3.4-$\mu$m aperture photometry from the European Southern Observatory 2.2- and 1-m telescopes. An atlas of ring features is provided, extending the catalog of P. D. Nicholson, M. L. Cooke, and E. Pelton (1990b, *Astron. J.* **100**, 1339–1362) to include B Ring features. Voyager 1 radio science and Voyager 2 Photopolarimeter (PPS) occultation observations were reanalyzed by converting the optical depth profiles to intensity profiles expected for the 28 Sgr occultation geometry. Ring feature times were measured from these rescaled lightcurves, including new measurements of B Ring features from the PPS data. Measurements of 30 presumed circular features, together with additional 28 Sgr observations from Catalina Station, Kitt Peak, San Pedro Mártir, United Kingdom Infrared Telescope, and Cerro Tololo Interamerican Observatory, described by Hubbard *et al.* (1993, this issue), were used to determine ring radii and Saturn's pole direction. Two separate techniques for computing ring orbit models are described: a sky-plane method, in which individual ring features are projected into the plane of the sky perpendicular to the star direction, and a solar system barycentric vector approach, which retains explicitly the 3-dimensional nature of the problem. The results of the two methods agree to high precision. The pole direction and radius scale cannot be accurately determined from 28 Sgr observations alone. The theoretical period of the forced precession of Saturn's pole due to solar torques on both Saturn's oblate figure and the equatorial satellites is estimated to be $1.76 \times 10^6$ year. A joint solution including both 28 Sgr and Voyager measurements, and accounting for this polar precession, gives a pole direction of $\alpha_P(B1950.0) = 38.4168° \pm 0.0035$ and $\delta_P(B1950.0) = 83.32329° \pm 0.00017$ ($\alpha_P(J2000.0) = 40.5955° \pm 0.0036$, $\delta_P(J2000.0) = 83.53812° \pm 0.00018$) at a reference epoch of 1980 November 12 at 23:46:32 UTC, consistent with the pole derived by P. D. Nicholson, M. L. Cooke, and E. Pelton (1990b, *Astron J.* 100, 1339–1362) from Voyager data alone. The pole uncertainty in this joint solution is dominated by uncertainties in the Voyager 1 and 2 trajectories. The ring radius scale is systematically about 1 km smaller than that found by P. D. Nicholson, M. L. Cooke, and E. Pelton (1990b, *Astron. J.* **100**, 1339–1362). If the a priori Voyager trajectory uncertainties are assumed to be negligible, then the observations can be used to determine the precession rate of Saturn's pole about the invariable pole of the Solar System. The corresponding rate of motion of Saturn's pole on the sky is found to be $0.86 \pm 0.31$ times the predicted rate of $0.339''$ year$^{-1}$. 

## 1. INTRODUCTION

The Voyager 1 and 2 encounters with Saturn (Smith *et al.* 1981, 1982) revealed a complex ring system: the classical A, B, and C Rings were found to be etched with wave features, demarcated by gaps and ringlets, and attended by a retinue of small satellites and a set of diffuse outer rings. These spacecraft observations provided a detailed snapshot of density and bending waves, noncircular ring features, and clues about the composition and particle size distributions of the rings, but additional observations would be necessary to refine the determination of ring orbits, the planetary gravitational field, and the opacity of the rings at a variety of wavelengths. Although Earth-based occultations have been successfully



0019-1035/93 $5.00

employed many times to study the rings of Uranus and Neptune (see Nicholson *et al.* 1990a, French *et al.* 1991, and Sicardy *et al.* 1991 for recent reviews), stellar occultations by Saturn are much more difficult to observe because of the brightness of the rings in reflected sunlight. The 3 July 1989 occultation of 28 Sgr by the Saturn system provided the first opportunity since the Voyager 1 and 2 encounters to observe the structure of Saturn's rings at high spatial resolution with good signal to noise.

A worldwide observing campaign was mounted to provide as complete coverage as possible of this rare occultation of such a bright star. Ground-based observations of the ring occultations of 28 Sgr were successfully carried out under good conditions from many major observatories in North and South America and in the Pacific (Brahic *et al.* 1989, DiCicco and Robinson 1989, Dunham *et al.* 1989, French *et al.* 1989, Harrington *et al.* 1989, Hubbard *et al.* 1989, and Porco *et al.* 1989). Intercomparison of these observations with Voyager 1 and 2 and Hubble Space Telescope (HST) (Elliot *et al.* 1992) observations of a later stellar occultation promises to yield a rich harvest of information about the dynamics, radial structure and particle sizes of the rings, and the gravitational harmonics of Saturn itself. As a preliminary step to these efforts, it is important to determine the radial scale of the rings and the direction of Saturn's pole as precisely as possible. Nicholson *et al.* (1990b) (hereafter referred to as NCP) derived an absolute radius scale for Saturn's rings based on radio and stellar occultations by the Voyager spacecraft, but it remained to be seen whether their results would be consistent with the 28 Sgr observations—Hubbard *et al.* (1990) had obtained a significantly different pole direction, based on a preliminary analysis of 28 Sgr observations from five stations.

Here, we present a comprehensive analysis of the astrometry of the 28 Sgr occultation, combined with Voyager 1 and 2 occultation observations, to determine the geometry of Saturn's ring system. Our analysis utilizes a large set of measurements of sharp-edged, quasicircular ring features observed by us from Palomar Observatory, McDonald Observatory, the NASA Infrared Telescope Facility (IRTF), and the European Southern Observatory (ESO), as well as observations from additional sites described in the adjoining paper by Hubbard *et al.* (1993), henceforth referred to as H93. In addition, we have remeasured the times of ring features observed in the Voyager 1 radio (RSS) occultation and the Voyager 2 ultraviolet (PPS) stellar occultation of δ Sco to put them on a common basis with the groundbased data.

The reduction of the 28 Sgr occultation observations and the astrometric analysis of the ring measurements are complex undertakings. Because of the large quantity of data to be analyzed for this effort and the importance of independent checks of our results, two separate groups have undertaken to determine the Saturn pole and ring plane radius scale from the full set of available 28 Sgr observations. For convenience, we shall refer to our group as the NE (northeast) group and the contingent represented by H93 as the SW (southwest) group, so named for the geographical locations of our home institutions. Each group has measured the times of sharp-edged ring features in their own occultation data and provided these measurements to the other group. Thus, both groups have begun with an identical set of groundbased occultation measurements for the astrometric solution. However, the formalism for the occultation geometry and astrometric reduction of the observations has been derived separately by each group, and the ring features actually fitted by H93 are a subset of the features fitted in the present paper. Our independent conclusions are presented here, and those of the SW group are presented in H93.

Our results are organized as follows. In Section 2 we describe the observations we have incorporated into the full ring orbit model. Next, in Section 3, we present an expanded catalog of ring features, along with measurements for more than 30 quasi-circular features from the 28 Sgr and Voyager occultations. These, combined with the 28 Sgr measurements of the SW group, are the observations that were fitted for the ring radius scale and Saturn's pole. In Section 4 we describe the geometry of both the 28 Sgr and Voyager occultations, outline our methods for determining ring orbits from the joint analysis of Earth-based and Voyager observations, and compute the forced precession of Saturn's pole. In Section 5 we present the results of our fits and our derived Saturn pole and radius scale. In the final section we compare these results with other determinations and present our conclusions. Two appendixes contain detailed descriptions of the astrometric methods employed in our solutions, sample calculations to facilitate comparisons with other methods, and comparison of results obtained with several independent computer codes.

## 2. OBSERVATIONS

### *2.1. The Occultation of 28 Sgr*

The 3 July 1989 occultation of 28 Sgr, first predicted by Taylor (1983) was notable not only for the brightness of the occulted star [$m(2.2\ \mu m) = 1.48$, $m(3.8\ \mu m) = 1.27$, as determined from photometric observations at Palomar Observatory during 1988], but also for the favorable geometry of the event, which allowed broad coverage of the ring and planet occultations from major observatories in Hawaii, western North America, and South America. The global geometry of the occultation is depicted in Fig. 1, which includes representative chords for northern and

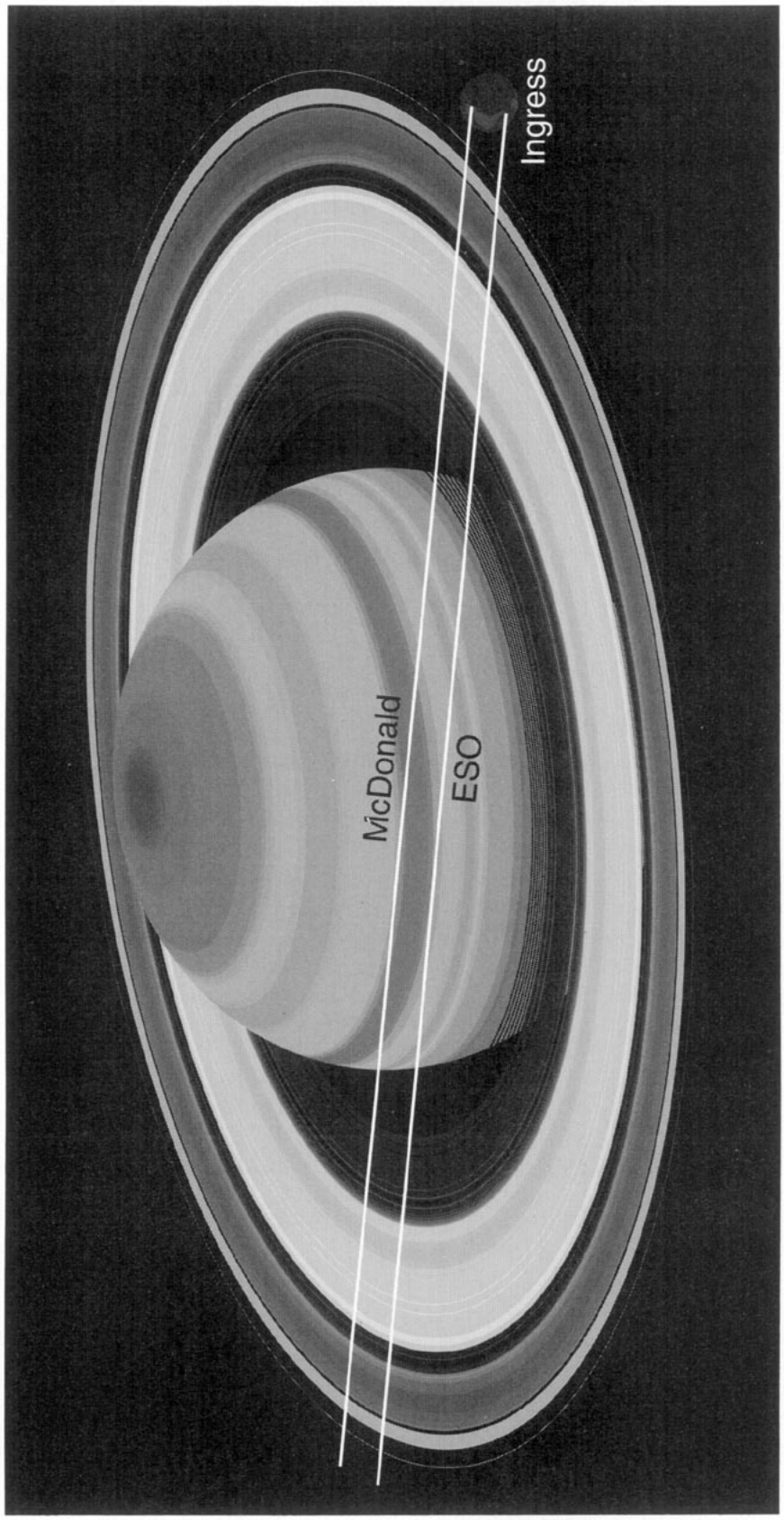


FIG. 1. Geometry of the 3 July 1989 occultation of 28 Sgr by Saturn and its rings. The apparent path of the occulted star is shown for two observatories: a representative northern hemisphere site (McDonald Observatory) and an extreme southern location (ESO). The sky-plane projection of the Earth is shown to scale in the lower right. The large north–south separation of the chords by terrestrial standards nevertheless samples only a small swath across Saturn. Note that during ingress along the McDonald chord, the occultation by the C Ring region (the innermost rings shown) was completed before the onset of the refractive atmospheric occultation. From ESO, however, atmospheric immersion began in the midst of the C Ring occultation, making it difficult to identify inner C Ring features in these data.

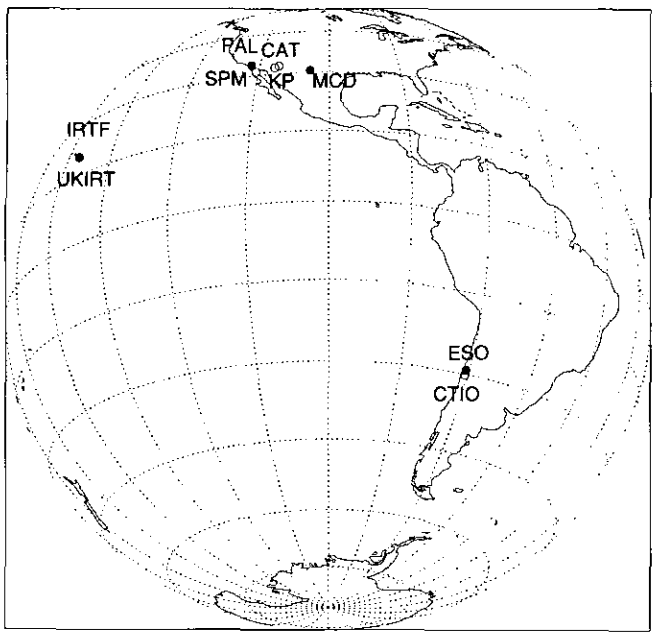


FIG. 2. Saturnicentric view of the Earth during the 28 Sgr occultation. Observations used for the present work were obtained by the NE group at stations marked by filled circles, and by the SW group from sites marked by open circles.

southern hemisphere sites. Figure 2 shows the saturnicentric view of the Earth at the geocentric mid-time of the occultation, along with the locations of the observatories represented in our analysis. For later reference, Table I contains the names, abbreviations, and coordinates of these sites.

Collectively, the NE group observed the 28 Sgr occultation from Palomar Observatory, McDonald Observatory, the IRTF (Harrington *et al.* 1993), and ESO. Detailed descriptions of the individual observations will be presented elsewhere. Here we give brief summaries of the observations, with an emphasis on the quality of the data and the overall timing accuracy for each station. As we shall see below, accurate absolute timing of all data sets is essential for proper reconstruction of the event astrometry and the determination of reliable orbit models for the rings.

*2.1.1. Palomar Observatory.* The 28 Sgr occultation was observed at the 5-m Hale telescope on Palomar Mountain, using the Cassegrain IR camera (Nicholson *et al.* 1991). This instrument employs a 58 × 62-pixel InSb detector array with a circular variable filter (CVF) (see Nicholson and Matthews 1991). The CVF, with a spectral resolution $\Delta\lambda/\lambda = 0.0155$, was tuned to a central wavelength of $\lambda = 3.9$ $\mu$m in order to avoid saturation of the detector by the bright star while maximizing the contrast between it and the icy rings. A total of 64,000 frames were recorded, each with an integration time of 0.15 sec. At this wavelength and exposure time in mid-summer, the thermal sky background was ~4000 DN per pixel, or 40% of the detector full-well level, whereas the signal from the rings was at most 40 DN per pixel. The integrated unocculted stellar signal was $1.1 \times 10^5$ DN. Both ingress and egress ring occultations were observed, but with 1.5- to 3.5-min data gaps every 20 min associated with opening new disk files. Observing conditions were excellent during ingress, but became partly cloudy during egress observations of the B and A Rings. The clouds, however, did not affect the identification and measurement of sharp-edged features in these data. An offset guider controlled the telescope pointing throughout the occultation, and the stellar image generally remained stationary on the array to within ±2 pixels.

Feature locations were determined from a preliminary

TABLE I
Observatory Coordinates

| Observatory | Group | Code | Aperture | $\phi$ Geodetic Latitude | $\lambda$ East Longitude | $h$ Altitude (m) | Geocentric Coordinates (km)[c] $x$ | $y$ | $z$ | $a\rho$ |
|---|---|---|---|---|---|---|---|---|---|---|
| Mt. Palomar | NE | PAL | 5 m | 33° 21′ 22″ | −116° 51′ 50″ | 1706 | −2410.418 | −4758.623 | 3487.953 | 6373.416 |
| Catalina Station | SW | CAT | 1.54 m | 32° 25′ 00″7 | −110° 43′ 55″1 | 2510 | −1908.587 | −5042.418 | 3400.889 | 6374.538 |
| Kitt Peak (Steward Observatory) | SW | KPi[a] | 2.3 m | 31° 57′ 47″ | −111° 35′ 57″8 | 2076 | −1994.441 | −5037.540 | 3358.056 | 6374.256 |
| | SW | KPe[b] | | | | | | | | |
| Mt. Hopkins | SW | MMT | MMT | 31° 41′ 19″6 | −110° 53′ 04″3 | 2608 | −1937.316 | −5077.444 | 3332.486 | 6374.880 |
| San Pedro Mártir | SW | SPM | 2.1 m | 31° 02′ 38″0 | −115° 27′ 47″0 | 2830 | −2352.532 | −4940.382 | 3271.523 | 6375.315 |
| McDonald | NE | MCD | 2.7 m | 30° 40′ 17″7 | −104° 01′ 17″60 | 2075 | −1330.746 | −5328.790 | 3235.689 | 6374.682 |
| United Kingdom IR Telescope | SW | UKIRT | 3.8 m | 19° 49′ 32″ | −155° 28′ 23″ | 4198 | −5464.312 | −2493.142 | 2151.363 | 6379.876 |
| Infrared Telescope Facility | NE | IRTF | 3 m | 19° 49′ 46″ | −155° 28′ 29″ | 4182 | −5464.386 | −2493.368 | 2150.964 | 6379.893 |
| European Southern Observatory | NE | ESO1 | 1 m | −29° 15′ 23″99 | −70° 44′ 18″33 | 2321 | 1837.774 | −5259.163 | −3099.886 | 6375.383 |
| | NE | ESO2 | 2.2 m | −29° 15′ 28″05 | −70° 44′ 11″96 | 2317 | 1837.915 | −5259.046 | −3099.993 | 6375.378 |
| Cerro Tololo Interamerican Obs. | SW | CTIO | 4 m | −30° 09′ 57″8 | −70° 48′ 53″6 | 2235 | 1814.305 | −5214.338 | −3187.425 | 6375.006 |

[a] Ingress observations
[b] Egress observations
[c] Reduction from geodetic to geocentric coordinates was performed according to the procedure and notation in Section K of the 1989 *Astronomical Almanac*, using the equatorial radius and flattening of the reference spheroid as given in Table VII. The geocentric radius of the station is given by $a\rho$.

reduction of the images consisting of sky-frame subtraction, flat-fielding, and simple aperture photometry on the flattened images. The ingress photometric quality is very high, as illustrated by the inner C Ring scan shown in Fig. 3a. The rms noise per 0.15-sec data point of the unocculted stellar flux, measured over 2500 frames, is 1.2% prior to A Ring ingress and 1.0% after Saturn egress and before the C Ring egress occultation. The A and B Ring egress data are noisier due to the clouds.

Absolute timing of the occultation was provided by driving the telescope's chopping secondary mirror 2″ north for exactly 2 sec (13.3 frames) at intervals of 1 min, and for exactly 4 sec on the hour, using trigger pulses from a crystal-oscillator continuously synchronized with shortwave radio time signals from WWVB. The propagation time uncertainty is ~5 msec. Individual frames recorded during the chopper transition show "double exposures" of the stellar image due to the rapid displacement (~1 msec) of the chopper, which permit the absolute occultation timing to be reconstructed with an accuracy of about $\frac{1}{3}$ frame, or 0.05 sec. As the stellar image remained on the array, this timing procedure resulted in no loss of photometric data. Timing pulses at the beginning and end of continuous 8000-frame files permitted the actual frame rate to be calibrated with an accuracy of $\pm 6$ $\mu$sec, but no measurable deviations from the nominal 150-msec rate were detected over any of the eight files of images recorded during the event.

A rather subtle problem in timing IR array observations is the "skew" introduced by the sequential readout of the array. At the 18-$\mu$sec per pixel-pair readout rate of the Palomar camera, it takes 32 msec to read an entire image. Since there is no shutter, the instant of readout effectively restarts the next integration on that pixel, with the result that integrations on the last column of pixels are delayed by ~32 msec relative to the first column. A

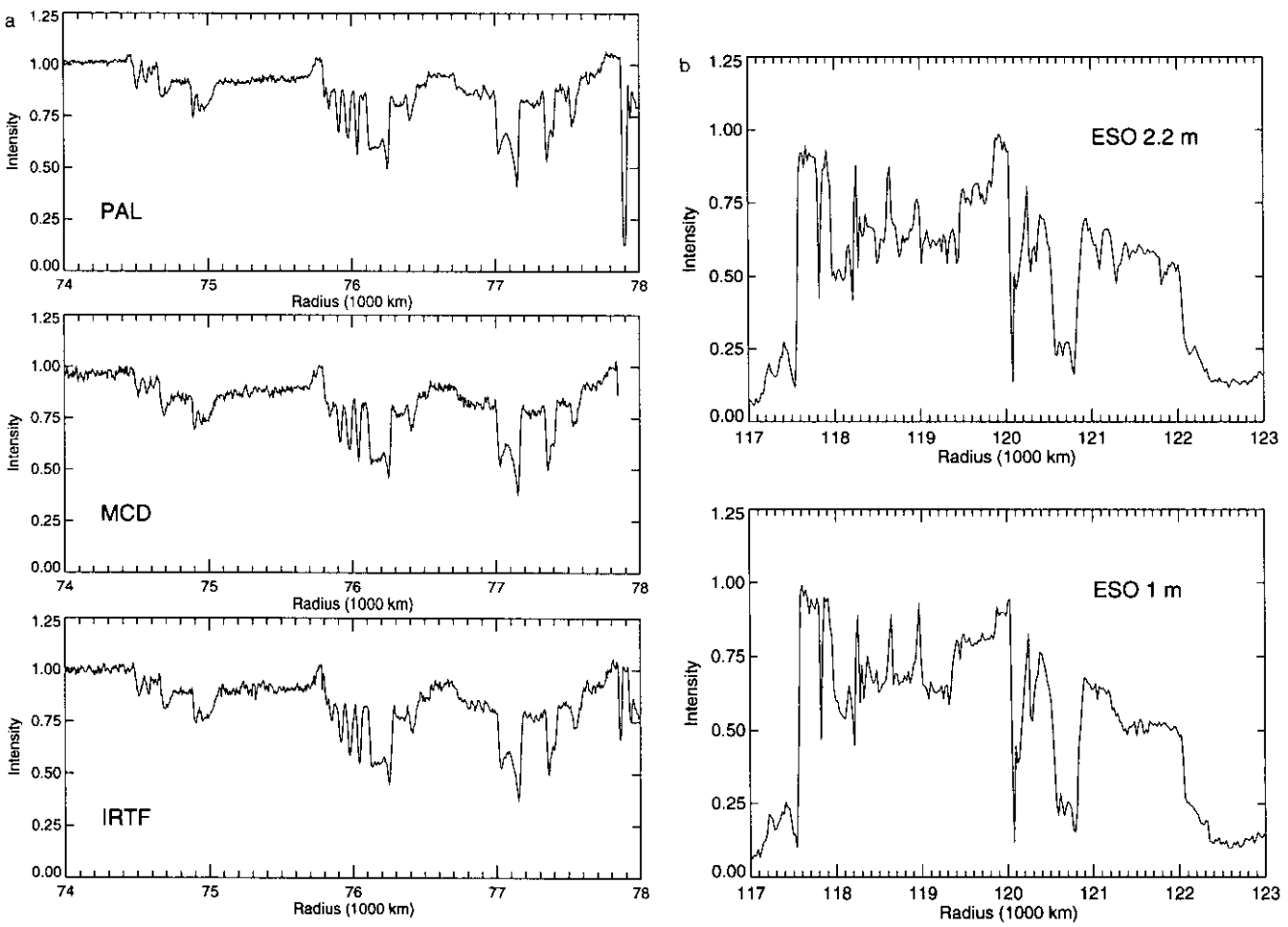


FIG. 3. Representative 28 Sgr occultation data obtained by the NE group. (a) Observations of the inner C Ring in the data from Palomar Observatory 5 m (PAL), McDonald Observatory 2.7 m (MCD), and the IRTF. Circular features 44, 40, and 39 are shown, as well as the Titan Ringlet (features 63, 62). (b) The Cassini Division, as observed from the ESO 2.2- and 1-m telescopes. A host of circular (features 20, 16, 13, 15, 12, and 11) and noncircular features are shown, including the Huygens Ringlet (features 53, 54), the 1.960 $R_S$ ringlet (features 17, 18), and the gap edge at feature 19. (See Fig. 4 and **Table II**.)

fraction of this delay must be taken into account in all absolute timing calibration schemes which involve the initial electronic trigger time of a frame. In the case of the Palomar data no such skew was introduced, as the star centroid remained on the same column of pixels throughout the observation.

Because each file of 8000 (or occasionally 6000) images was calibrated independently to UTC as described above, there is also no possibility of unmodeled timing drifts or glitches in the Palomar data larger than ~0.05 sec. (There may, however, exist smaller [<0.05 sec] errors in the absolute timing calibration which vary randomly from one file of images to the next.) The "hard-wired" nature of the Palomar timing calibration is completely independent of the camera's triggering, readout, or buffering electronics and software.

*2.1.2. McDonald Observatory.* Observations from McDonald Observatory were carried out from the 2.7-m telescope using a 58 × 62 InSb IR array and from the 2.1-m telescope using a four-channel visual aperture photometer (French *et al.* 1989, 1990). The IR observations were made at $\lambda = 2.1$ $\mu$m, where the planet was dark due to absorption by methane in Saturn's atmosphere and the star was relatively bright compared to reflected sunlight from the rings. The entire ring system and atmosphere occultations were observed continuously for ingress and for egress at a time resolution of 0.2 sec per frame. The occultation light curve was obtained from automated digital photometry of nearly 40,000 individual frames. Because the reflected sunlight from the rings contributed measurably to the total flux, care was taken to compensate for slight guiding errors by aligning each individual frame to a common template before measuring the stellar flux in each image. The typical rms noise per 0.2-sec data point of the unocculted stellar flux is 1.5%. Figure 3a shows a scan of the inner C Ring from the McDonald 2.7-m ingress observations.

Absolute timing of the IR array observations was determined as follows. A portable oven-stabilized quartz oscillator-driven clock (Baron 1989) was synchronized to UTC using the McDonald Observatory cesium clock just prior to the observations. Observations with the array were initiated with the 1-Hz signal from the portable clock and throughout the observation period the drift rate between the oscillator on the array controller and the portable clock were monitored on an oscilloscope. The drift rate was constant throughout the entire occultation, and the true integration time per image was found to be $(1 + 2.267 \times 10^{-5}) \times 0.2$ sec. Failure to compensate for this oscillator drift would have introduced errors of several km into the derived occultation chord length for the McDonald station.

An independent check of the timing accuracy was provided by the aperture photometry at visual wavelengths obtained simultaneously from the nearby 2.1-m telescope. Time signals were recorded as part of the data train at high time resolution, providing absolute timing directly in the data. Although the observations were noisy due to significant scattered light from Saturn and the rings at visual wavelengths, the stellar signal could be retrieved by taking advantage of the color differences between the star and rings, and forming ratios of appropriate linear combinations of observations at two wavelengths. The edge of Saturn's A Ring was clearly identified on both ingress and egress, and the observed event times agreed to within a few hundredths of a second with the times measured from the IR array observations.

The atmosphere occultations were observed both for ingress and egress and showed strong intensity spikes due to the nonisothermal characteristics of Saturn's atmosphere. The spikes in the McDonald observatory 2.7-m atmosphere light curves were used as an independent set of fiducial features to determine correction factors to the instrumental timing of several 28 Sgr data sets obtained by the SW group, as described by H93.

*2.1.3. NASA IRTF.* The occultation was observed from the IRTF using the University of Rochester 62 × 58-pixel InSb array camera (Dunham *et al.* 1989, Harrington *et al.* 1989, 1991; see Harrington *et al.* 1993 for additional detail on these observations). The IRTF observations spanned the inner C Ring on ingress and the complete ring system on egress (problems with the telescope control system prevented an earlier start). No clouds were seen overhead and the relative humidity was <5% when data recording began. The reflected signals from the rings and planet were minimized by observing at $\lambda = 3.255$ $\mu$m, $\Delta\lambda = 0.230$ $\mu$m, near the edge of a water ice absorption band and within a methane band.

Three 1/12-sec exposures were averaged to form each stored image, for an effective time resolution of 0.25 sec. From each image, a sub-frame of 12 rows containing the star was retained. The lightcurve was generated from aperture photometry performed on the bias-corrected, linearized, flat-fielded, sky-subtracted images. In the clear regions between the rings and planet on ingress and egress and exterior to the F Ring on egress, the standard deviation of the unocculted stellar flux (per 0.25-sec integration) was 1.7, 1.5, and 1.0% of the flux, respectively. Since the star position was stable to within ~2 pixels, no significant differential time skew was introduced by the array's sequential readout. The high quality of the data is evident in the ingress inner C Ring scan shown in Fig. 3a.

Absolute timing was provided by a calibrated, oven-stabilized, quartz-oscillator-driven clock (Baron 1989). Rather than running the camera from the computer's clock and placing external timing signals in the data, the IRTF observers replaced the computer's native bus interrupt circuit with one driven directly by the quartz clock.

Thus, each frame readout represents an event whose absolute timing accuracy is better than 60 $\mu$sec. This uncertainty arises from variations in the length of interrupt service routines in the computer and from the stability of the interrupt-generating circuit.

The quartz clock was compared frequently during the event to a rubidium standard provided by the WWVH station at Barking Sands, Kauai, Hawaii; the total drift between these two clocks during the observations was 200 nsec. After the event, the offset and frequency drift of the Rb clock relative to the WWVH primary standard were determined; the offset measurement was used to reconstruct the absolute timing and the drift was found to be less than 100 nsec/day.

In the course of our astrometric analysis, we discovered significant inconsistencies in the locations tabulated in the *Astronomical Almanac* and in several observatory handbooks. The problem is particularly acute for telescopes on Mauna Kea: for example, the IRTF and CFHT Handbooks list respective positions that would put the IRTF nearly 0.5 km south of the CFHT, when in fact it is north of the CFHT. The observatory coordinates listed in Table I were derived as follows: The position for the University of Hawaii 88″ telescope (UH88) given in the 1981 *Astronomical Almanac* was used as a reference point, and the positions of the other telescopes relative to the UH88 were measured on the site plan given in Fig. 1.5 of the University of Hawaii Users Manual (3rd edition, 1990 January). To obtain observatory coordinates that would at least be self-consistent, the measured coordinates were converted to differences in longitude and latitude and added to the UH88 position. The results were rounded to an arcsecond (about 30 m) to avoid overinterpretation.

*2.1.4. ESO.* Ring occultation observations at ESO (Brahic *et al.* 1989) were carried out from both the 2.2- and the 1-m telescopes at $\lambda = 3.4$ $\mu$m, using identical InSb nitrogen-cooled aperture photometers in the chopping mode. On the larger telescope, the chopping frequency was 8.8 Hz, with a 98-arcsec throw in the E–W direction; chopping on the 1-m telescope was at 8 Hz with a 68-arcsec E–W throw. The effective focal ratio of both systems was f/35, and 5-arcsec diaphragms were used on both telescopes to minimize background noise. Data were recorded digitally at 100 Hz.

Observing conditions were good throughout the occultation: the average seeing was 1.2 arcsec in the visible and 1.4 arcsec in the infrared. The signal quality was good throughout much of the event, but was substantially degraded at the 2.2-m telescope by the end of the occultation due to drifting of the star out of the small aperture. Telescope pointing was controlled by an optical guide star, and as Saturn was setting the infrared field of view of the photometer aperture drifted slightly off the star because of differential atmospheric refraction. Additionally, atmospheric immersion occurred during the C Ring occultation (see Fig. 1), commingling ring features with the spikes in the atmosphere occultation light curve. Nevertheless, identifiable ring features could be measured throughout most of the ingress and egress occultations in the data from both telescopes. The ingress Cassini Division observations were particularly clean for both ESO telescopes, as shown in Fig. 3b.

There is some evidence of timing problems with both ESO data sets. A common clock was used to drive both observations, and comparison of the light curves from the two telescopes shows that they are indeed on a common time base. However, during the summer of 1989, ESO technicians reported intermittent problems with the time service (Sicardy, private communication). Comparison with the well-calibrated observations obtained at the nearby Cerro Tololo Interamerican Observatory (CTIO; H93) shows that the observed ESO ring event times systematically lagged behind predicted event times by about 0.21 sec for both ESO telescopes. The effective time constant of the IR electronics of both ESO systems was found both by direct fits to calibration data and by power spectral analysis to be approximately 0.07 sec for a double-pole filter, too small to account for the large lag time inferred from comparisons between the ESO and CTIO times. In the absence of more detailed information about the nature of the timing problems at ESO, we have treated the ESO observations as providing accurate *relative* measurements of the times of ring features, but not accurate *absolute* ring event times.

The observatory coordinates for the two ESO telescopes used for these observations were provided by P. Bouchet of the ESO observatory staff, based on GPS readings taken on 27 February 1992. The estimated accuracy is 0.5″.

*2.1.5. Other 28 Sgr Observations.* In addition to the observations described above, high-quality ring occultation observations from the 28 Sgr event have been reported from Las Campanas and CTIO in Chile, the United Kingdom Infrared Telescope (UKIRT) on Mauna Kea, the Multiple Mirror Telescope (MMT) on Mt. Hopkins, the Kitt Peak 2.3-m and Catalina Station 1.54-m telescopes in southern Arizona (Porco *et al.* 1989), as well as from San Pedro Mártir in Baja California (H93), Lick Observatory (R. Stover, private communication), and Lowell observatory (R. Millis, private communication). In the adjoining paper, H93 present ring feature measurements from IR imaging observations at Kitt peak and UKIRT, as well as aperture photometry observations at Catalina Station, San Pedro Mártir, the MMT and CTIO.

According to H93, reliable timing calibrations were available for the CTIO and UKIRT observations, and we

have adopted their tabulated ring event times as accurate absolute times. For each of the other four stations, however, there is some uncertainty about the reliability of the absolute timing calibration. H93 have cross-correlated the spikes in the atmosphere immersion and emersion occultation light curves to determine timing offsets with respect to the McDonald Observatory 2.7-m atmosphere observations, which have a well-calibrated time base as described previously. By comparing observed and predicted spike arrival times based on a model of uniform atmospheric layering, they derived correction factors to apply to the nominal start times of each of the data sets in question.

Although we agree that the atmospheric spike correlation technique provides a rough measure of the time corrections for these stations, it has some limitations: (i) it is model-dependent, and assumes that the oblateness of the atmosphere is known at the probed level and that the spike-producing features in the atmosphere are parallel to the assumed oblate surface over the separation distance between the observatories; and (ii) only a few spikes are present in each of the light curves, resulting in an uncertainty in the derived offset times as large as ~0.05 sec.

We have taken an alternative approach to determining the absolute timing for these observations. We have used the full set of ring measurements themselves as fiducials to be coaligned by a proper choice of a single station offset time. This avoids making any assumptions about the atmospheric structure and assumes instead that the ring features we are using in our orbit fits are circular. Examination of the patterns of ring orbit residuals with ring longitude can be used a posteriori to test the viability of this assumption.

To summarize, we have adopted the ring event times given in Table III of H93 as accurate absolute times for UKIRT and CTIO. For the Catalina Station, KPNO (ingress and egress treated separately), San Pedro Mártir, and MMT observations we have determined best-fitting constant offset times to the event times given in their Table III. Since these tabulated times have already been corrected on the basis of the atmospheric cross-correlation lag measurements, our derived offset time for each station represents an *additional* small correction. Thus, our offset times can perhaps best be thought of as refinements to the offsets determined from the atmospheric correlation technique. As we shall see, these additional corrections are for the most part relatively small, but not negligible.

### 2.2 Voyager Observations

During the 13 November 1980 Saturn encounter, Voyager 1 carried out a RSS occultation observation in which the entire radial extent of the rings was probed during egress at $\lambda = 3.6$ cm and $\lambda = 13$ cm (Tyler *et al.* 1983). By combining the intensity and phase information of the recorded occultation signal, the effects of diffraction could be removed, resulting in high-resolution optical depth profiles of the rings from the 3.6-cm data for all but the most opaque parts of the A and B Rings (Marouf *et al.* 1986).

During the Voyager 2 encounter on 25/26 August 1981, the egress ring occultation of δ Sco was observed with two ultraviolet instruments: the Photopolarimeter (PPS) (Lane *et al.* 1982, Esposito *et al.* 1983, 1987) and the Ultraviolet Spectrometer (UVS) (Sandel *et al.* 1982, Holberg 1982, Holberg *et al.* 1982). Both instruments obtained high SNR data, although the PPS observations had a much shorter integration time, providing significantly better radial resolution of the rings than the UVS profiles.

Simpson *et al.* (1983) (hereafter referred to as STH) used the RSS and UVS observations to determine the radius scale of the ring system. More recently, NCP combined the RSS and PSS observations to determine the pole direction and radius scale even more precisely by including more features than used by STH and by employing the higher resolution PPS ultraviolet observations. Although only two occultation chords were observed with Voyager 1 and 2, the very different viewing geometries of the two events provided nearly orthogonal constraints. The rings were nearly edge-on during the RSS occultation, making these observations very sensitive to the pole direction; the δ Sco occultation was more indicative of the radial scale of the rings. In the end, uncertainties in the Voyager 1 and 2 trajectories were the dominant source of error in NCP's derived pole and radius scale.

For our present purposes, we treat the RSS and PPS occultations on an equal footing with the 28 Sgr data sets and regard the measured times of edges of sharp circular ring features as the fundamental observations to be matched by a model for the ring orbits and pole direction. In order to remeasure the event times for ring features in the Voyager data, we obtained high-resolution RSS and PPS optical depth profiles of the rings as a function of time from Standford University and from NASA's Planetary Data System Rings Node at the NASA Ames Research Center.

## 3. RING FEATURES

### 3.1. Ring Feature Catalog

For each of the observations described above, the first task was to identify a set of quasi-circular ring features throughout the main rings and measure their event times for use in the ring orbit-fitting procedure. Most of the features are sharp optical depth transitions at gap or ring edges, or between dense "plateau" regions and a low-optical depth "background." A few of our selected fea-

tures are prominent peaks (or dips) in the optical depth profile, with measured locations corresponding to the deepest (or highest) point in the light curve, area-weighted for the noisier profiles.

Our starting point for this selection was NCP's systematic survey of ring features visible in both the RSS and the PPS data sets. They catalogued both apparently circular and many decidedly noncircular features in the A Ring, the Cassini Division, and the C Ring, and for ease of comparison with their work we have adopted their numbering scheme, while adding several new features evident in the B Ring. An atlas of the 66 presently numbered ring features is shown in Fig. 4, with radii listed in Table II. Abbreviations indicating the basic feature type are used in the table as follows: major ring sections, narrow ringlets, and plateau regions have been grouped together and their inner and outer edges designated IER and OER, respectively. The edges of gaps and low-$\tau$ regions are likewise designated IEG and OEG, and the narrow, approximately symmetrical features described above (whose centers or cores are measured) are given the label COR. Although such designations are not always unique (an IEG could also be called an OER, and an OEG an IER), these codes should aid in the identification of individual features in other occultation profiles of the rings.

In the NCP nomenclature, numbers under 50 were reserved for features which appeared circular, whereas those above 50 were assigned to known noncircular features: eccentric ringlets (e.g., the Maxwell and Titan ringlets (Porco *et al.* 1984a)), and gap or ring edges perturbed by satellite resonances (e.g., the outer edges of the A and B Rings; Porco *et al.* 1984b). Features were numbered radially inward, corresponding to an ingress occultation. Although further studies have since shown some low-numbered features to be noncircular, we have retained the original NCP designations. These include features 2 (the inner edge of the Keeler Gap; Cooke 1991) and 19 (the inner edge of the gap at 1.960 $R_S$; Flynn and Cuzzi 1989). Other features which showed unusually large residuals either in the NCP study or in our own comparisons of 28 Sgr data, but which have not been subjected to detailed study, are 9, 10, 14, 17, and 18. Feature 6 of NCP was deemed to be ambiguous and too subtle to detect in the 28 Sgr data. All the above were excluded from our list of quasi-circular features to be fitted.

Several new features have been added to the NCP list: 13 (a narrow gap edge in the Cassini Division), 22 (the inner edge of the B Ring), 41 and 42 (the outer edges of two plateau features in the C Ring), 43 (the outer edge of the Colombo Gap), and 44 (the inner edge of the C Ring). All these features are visible in both the RSS and PPS data, but were not used by NCP because of the abundance of nearby features.

Because of the extremely oblique incidence of the beam during the Voyager 1 radio occultation experiment, virtually no signal was detected through the optically thick B Ring. Although candidate features were visible in the corresponding section of the PPS profile, these were omitted from the NCP analysis which rested on an intercomparison of the two Voyager profiles. With the advent of multiple data sets from the 28 Sgr occultation, however, many reproducible features were found in the inner B Ring and subsequently identified in the PPS profile. These features have been numbered 71–83.

### *3.2. Measurement of 28 Sgr Ring Features*

The specification of ring feature event times depends upon the precise definition one adopts for an edge, such as the half-intensity or half-$\tau$ point in the data, as pointed out by NCP. Furthermore, although Voyager RSS and PPS occultation observations indicate that many of the ring features studied here are quite sharp, both Fresnel diffraction and the finite angular extent of the occulted star make the observed transitions in stellar intensity quite gradual (~1 sec) for the 28 Sgr features. *We assume that the time of half-intensity of the observed signal change corresponds to the location of the geometric edge of a 28 Sgr ring feature.* In principle, this could lead to a substantial systematic error in the determination of ring feature positions, since diffraction effects are ignored. For a point source, the normalized intensity of the diffraction pattern at the geometric shadow is 0.25, not 0.5, and the observed half-intensity point could be displaced substantially from the geometric edge, depending on the Fresnel scale of the observations. Additional smearing of the light curve due to the finite size of the stellar disk further complicates things.

We have investigated the importance of both diffraction and stellar diameter on individual feature measurements with a series of model calculations illustrated in Fig. 5. The left panels in this figure show straight-edge diffraction patterns computed for the geometry of the 28 Sgr occultation, for projected stellar diameters of 0, 2, 5, 10, and 20 km at wavelengths of 1 and 4 $\mu$m. The shaded region is the geometric shadow. Notice that the half-intensity points are systematically displaced away from the ring material. The right panels show the displacement as a function of projected star diameter. If the occulted star had had a projected diameter of only a few kilometers, the systematic errors in feature locations would have been substantial for long-wavelength observations. However, for the ~20 km projected stellar diameter of 28 Sgr, systematic errors are $<0.1$ km for $\lambda \leq 4$ $\mu$m. To this level of precision, diffraction effects may be neglected when determining feature locations.

We tested two procedures for the actual measurement of the large set of ring features in the NE data sets. First,

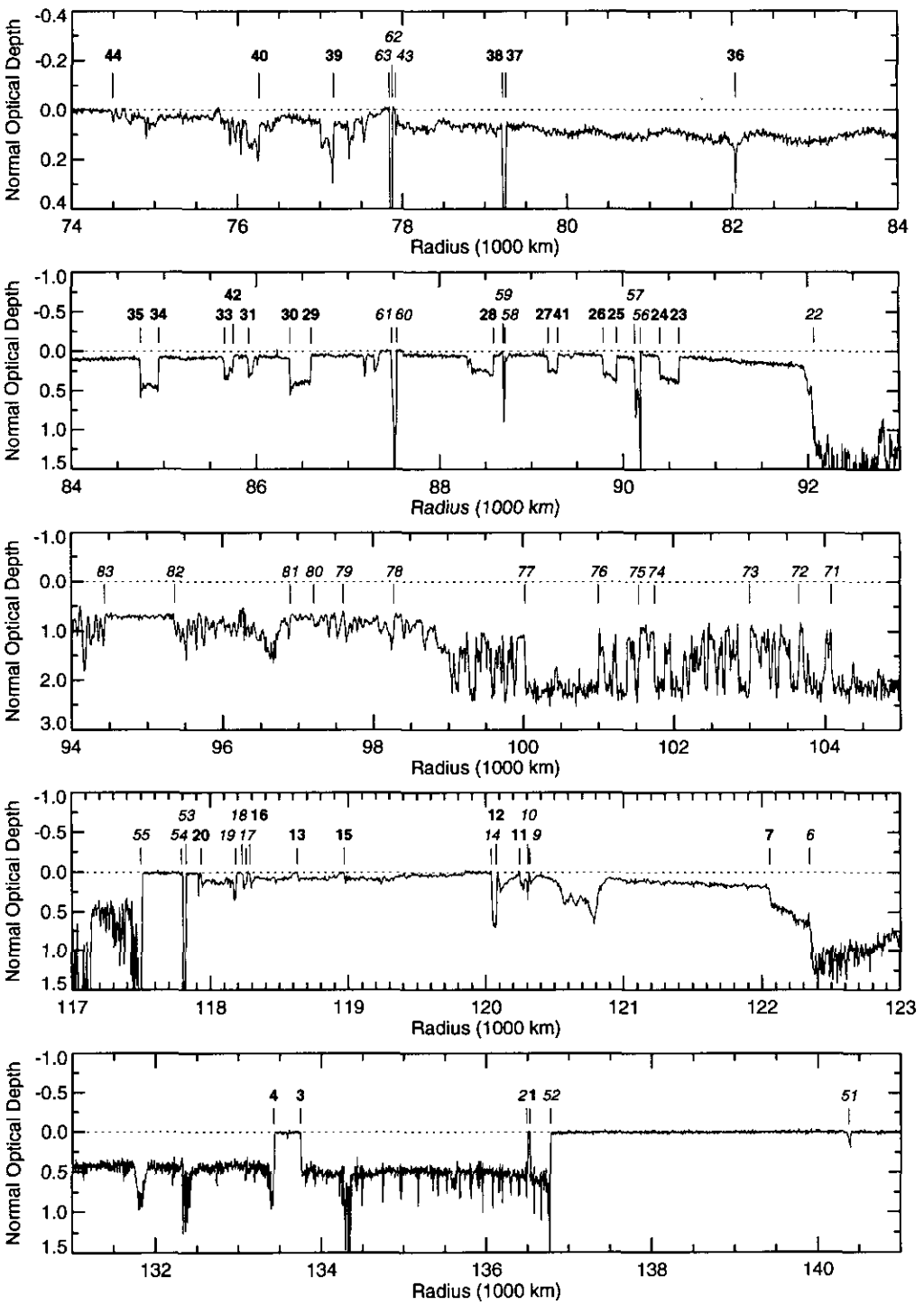


FIG. 4. Atlas of ring feature designations. The features listed in **Table II** are identified in the Voyager 2 PPS stellar occultation trace. The numbering scheme is consistent with that of NCP, but has been extended to include additional B Ring features (see text). The set of quasi-circular features used in our final fit for Saturn's pole and the ring radius scale are labeled in bold face; all others are in oblique text.

we selected several isolated ringlets and fitted for the edge times using a square-well model for the rings, incorporating the effects of diffraction and the finite stellar angular diameter, in the same fashion used for fits of Uranian ring occultations (Elliot *et al.* 1984). From these fits, we found that the projected stellar diameter of 28 Sgr was somewhat less than 20 km for a uniformly bright disk, but that the fitted feature times did not depend

TABLE II
Voyager Observations of Saturn Ring Features

| Feature[a] | Radius[b] (km) | V1 RSS[c] (ERT) | V2 PPS[d] (SCET) | Code[e] | Description |
|---|---|---|---|---|---|
| 51 | 140461.0 | 4:59:13.01 | 1:51:00.01 | COR | F Ring (core) |
| 52 | 136774.4 | 4:58:27.80 | 1:44:20.38 | OER | A Ring outer edge[f] |
| 1* | 136522.0 | 4:58:24.68 | 1:43:53.59 | OEG | Keeler Gap[g] |
| 2 | 136488.2 | 4:58:24.23 | 1:43:50.30 | IEG | Keeler Gap[g] |
| 3* | 133745.2 | 4:57:51.10 | 1:38:54.58 | OEG | Encke Gap[h] |
| 4* | 133423.5 | 4:57:47.19 | 1:38:20.39 | IEG | Encke Gap[h] |
| 7* | 122052.5 | 4:55:27.33 | 1:18:51.75 | IER | A Ring inner edge (Cassini outer edge) |
| 9 | 120316.5 | 4:55:05.61 | 1:15:59.40 | OEG | 1.994 Rs gap[i] |
| 10 | 120305.7 | 4:55:05.50 | 1:15:58.13 | OER | 1.994 Rs ringlet[i] |
| 11* | 120245.0 | 4:55:04.71 | 1:15:52.33 | IER | 1.994 Rs ringlet[i] |
| 12* | 120076.3 | 4:55:02.59 | 1:15:35.66 | OER | 1.990 Rs ringlet[i] |
| 14 | 120039.0 | 4:55:02.14 | 1:15:31.84 | IER | 1.990 Rs ringlet[i] |
| 15* | 118968.3 | 4:54:48.66 | 1:13:46.31 | OEG | |
| 13* | 118629.1 | 4:54:44.38 | 1:13:12.97 | OEG | |
| 16* | 118283.9 | 4:54:40.02 | 1:12:39.08 | OEG | |
| 17 | 118256.5 | 4:54:39.64 | 1:12:36.67 | OER | 1.960 Rs ringlet[i] |
| 18 | 118229.3 | 4:54:39.27 | 1:12:34.20 | IER | 1.960 Rs ringlet[i] |
| 19 | 118183.2 | 4:54:38.76 | 1:12:29.12 | IEG | [i] |
| 20* | 117932.2 | 4:54:35.60 | 1:12:04.41 | OEG | [j] |
| 53 | 117833.7 | 4:54:34.54 | 1:11:53.30 | OER | Huygens Ringlet |
| 54 | 117814.4 | 4:54:34.30 | 1:11:51.39 | IER | Huygens Ringlet |
| 55 | 117516.0 | 4:54:30.49 | 1:11:22.44 | OER | B Ring outer edge (Cassini inner edge)[f] |
| 71† | 104083.4 | | 0:49:56.10 | OEG | |
| 72† | 103673.2 | | 0:49:17.50 | IEG | |
| 73 | 103009.2 | | 0:48:15.10 | OER | |
| 74 | 101741.5 | | 0:46:16.20 | OEG | |
| 75† | 101549.3 | | 0:45:58.20 | IEG | |
| 76† | 101009.7 | | 0:45:07.70 | IEG | |
| 77 | 100024.1 | | 0:43:35.60 | OEG | |
| 78† | 98287.2 | | 0:40:53.70 | OER | |
| 79 | 97600.3 | | 0:39:49.80 | COR | |
| 80 | 97212.9 | | 0:39:13.80 | IER | |
| 81† | 96899.6 | | 0:38:44.70 | IEG | |
| 82† | 95358.3 | | 0:36:21.74 | OEG | B Ring "flat spot" |
| 83† | 94444.1 | | 0:34:57.11 | IEG | B Ring "flat spot" |
| 22 | 91983.2 | 4:48:47.55 | 0:31:10.00 | IER | B Ring inner edge (C Ring outer edge) |
| 23* | 90614.9 | 4:48:27.53 | 0:29:03.72 | OER | |
| 24* | 90405.7 | 4:48:24.44 | 0:28:44.48 | IER | |
| 56 | 90197.3 | 4:48:21.40 | 0:28:25.02 | OER | 1.495 Rs Ringlet[k] |
| 57 | 90133.7 | 4:48:20.45 | 0:28:19.22 | IER | 1.495 Rs Ringlet[k] |
| 25* | 89938.8 | 4:48:17.53 | 0:28:01.46 | OER | |
| 26* | 89788.3 | 4:48:15.29 | 0:27:47.65 | IER | |
| 41* | 89295.3 | 4:48:07.94 | 0:27:02.30 | OER | |
| 27* | 89190.4 | 4:48:06.38 | 0:26:52.60 | IER | |
| 58 | 88720.3 | 4:47:59.31 | 0:26:09.51 | OER | 1.470 Rs ringlet[k] |
| 59 | 88701.7 | 4:47:59.05 | 0:26:07.67 | IER | 1.470 Rs ringlet[k] |
| 28* | 88594.3 | 4:47:57.43 | 0:25:57.83 | OER | |
| 60 | 87557.9 | 4:47:42.06 | 0:24:20.67 | OER | Maxwell Ringlet[l] |
| 61 | 87486.3 | 4:47:40.74 | 0:24:15.47 | IER | Maxwell Ringlet[l] |
| 29* | 86602.4 | 4:47:27.09 | 0:22:54.98 | OER | |
| 30* | 86371.9 | 4:47:23.53 | 0:22:33.85 | IER | |
| 31* | 85923.6 | 4:47:16.59 | 0:21:52.70 | IER | |
| 42* | 85758.7 | 4:47:14.03 | 0:21:37.56 | OER | |
| 33* | 85661.5 | 4:47:12.52 | 0:21:28.61 | IER | |
| 34* | 84949.2 | 4:47:01.35 | 0:20:23.41 | OER | |
| 35* | 84750.3 | 4:46:58.22 | 0:20:05.15 | IER | |
| 36* | 82041.6 | 4:46:14.62 | 0:15:57.20 | COR | |
| 37* | 79265.1 | 4:45:27.85 | 0:11:43.39 | OER | |

TABLE II—*Continued*

| Feature | Radius (km) | V1 RSS (ERT) | V2 PPS (SCET) | Code | Description |
|---|---|---|---|---|---|
| 38* | 79221.0 | 4:45:27.11 | 0:11:39.25 | IER | |
| 43 | 77918.0 | 4:45:04.32 | 0:09:40.59 | OEG | Titan Gap outer edge |
| 62 | 77872.1 | 4:45:03.39 | 0:09:36.26 | OER | Titan Ringlet[l] |
| 63 | 77854.9 | 4:45:03.11 | 0:09:34.56 | IER | Titan Ringlet[l] |
| 39* | 77164.4 | 4:44:50.73 | 0:08:31.39 | OER | |
| 40* | 76262.9 | 4:44:34.24 | 0:07:09.00 | OER | |
| 44* | 74490.0 | 4:44:00.64 | 0:04:26.95 | IER | C Ring inner edge |

[a] Feature numbers are based on the nomenclature of Nicholson *et al.* (1990b). A Ring, Cassini Division, and C Ring features assumed to be circular for this analysis are marked with an asterisk; B Ring circular features are marked by a †.
[b] Radii were determined using NCP pole (Fit 1, **Table IX**).
[c] Earth received time (ERT) of Voyager 1 Radioscience (RSS) $\lambda = 3.6$ cm ring egress occultation.
[d] Spacecraft event time (SCET) of Voyager 2 ultraviolet Photopolarimeter (PPS) egress occultation of $\delta$ Sco.
[e] Three-letter codes for feature type: IER (OER), inner (outer) edge of ring, ringlet, or plateau; IEG (OEG), inner edge of gap; COR, core or center of an optical depth dip or peak
[f] Porco *et al.* (1984b)
[g] Cooke (1991)
[h] Cuzzi and Scargle (1985), Showalter *et al.* (1986)
[i] Nicholson *et al.* (1990b)
[j] Flynn and Cuzzi (1989)
[k] Porco and Nicholson (1987)
[l] Porco *et al.* (1984a)

strongly on the adopted stellar diameter. This is consistent with the models in Fig. 5. These results will be described in more detail elsewhere. (The SW group (H93) obtained very similar results and determined the projected diameter of 28 Sgr to be 18.0 ± 0.6 km.)

Next, we tested a simple graphical technique to estimate the times of half-intensity directly from plots of the same data and found in all cases that the differences between the fitted and hand-measured feature locations were <0.05 sec, corresponding to <1 km in ring plane radius. Since many ring features are not isolated, but instead are superimposed on regions of slowly varying optical depth, the primary practical problem then consists of estimating reliably what the background levels are on either side of the sharp edge being measured. We decided to use the graphical technique for our complete set of measurements rather than the square-well model, as it was easier to perform, the results were reproducible, and the background levels (although sometimes subjectively estimated) could be consistently matched from one data set to another. Most of the measurements were made interactively, using a simple computer routine to determine the half-flux point once the background levels had been established by eye.

Using these procedures, and intercomparing light curves from all observatories to maintain consistency in the identification of features, we measured event times for up to 65 features in each ingress or egress light curve from Palomar, McDonald, the IRTF (Harrington *et al.* 1993), and both ESO telescopes. The results for the 38 quasi-circular features are presented in Tables III–VI. Combined with the event times in H93, they represent the full set of 28 Sgr observations used in our circular ring orbit fits. In addition to the suspected noncircular features listed above, we have also excluded from our fits (and from the data tables) features 22 and 43 because of frequent difficulties encountered in obtaining accurate measurements (which may indicate noncircularity). Features 1 and 12, excluded by NCP from their Voyager-based fit because of proximity to noncircular features, have been reinstated here after preliminary fit residuals using this much larger data set were found to be no larger than those of typical "circular" features. In the case of the Keeler Gap, independent evidence is mounting (e.g., Cooke 1991) that the resonant interactions driving the inner edge (feature 2) do not affect the outer edge (feature 1), so the latter feature can be counted among the scant circular features in the outer A Ring.

Our final set thus consists of 38 putatively circular features: 26 from NCP, less features 6 and 19, and with the addition of features 1, 12, 13, 41, 42, and 44 (noted by an asterisk in the first column of Table II), and B Ring features 71, 72, 75, 76, 78, and 81–83 (noted by the † symbol in Table II). The remaining 28 numbered features are noncircular, difficult to measure reliably in the 28 Sgr data, or both. A total of 240 usable measurements of

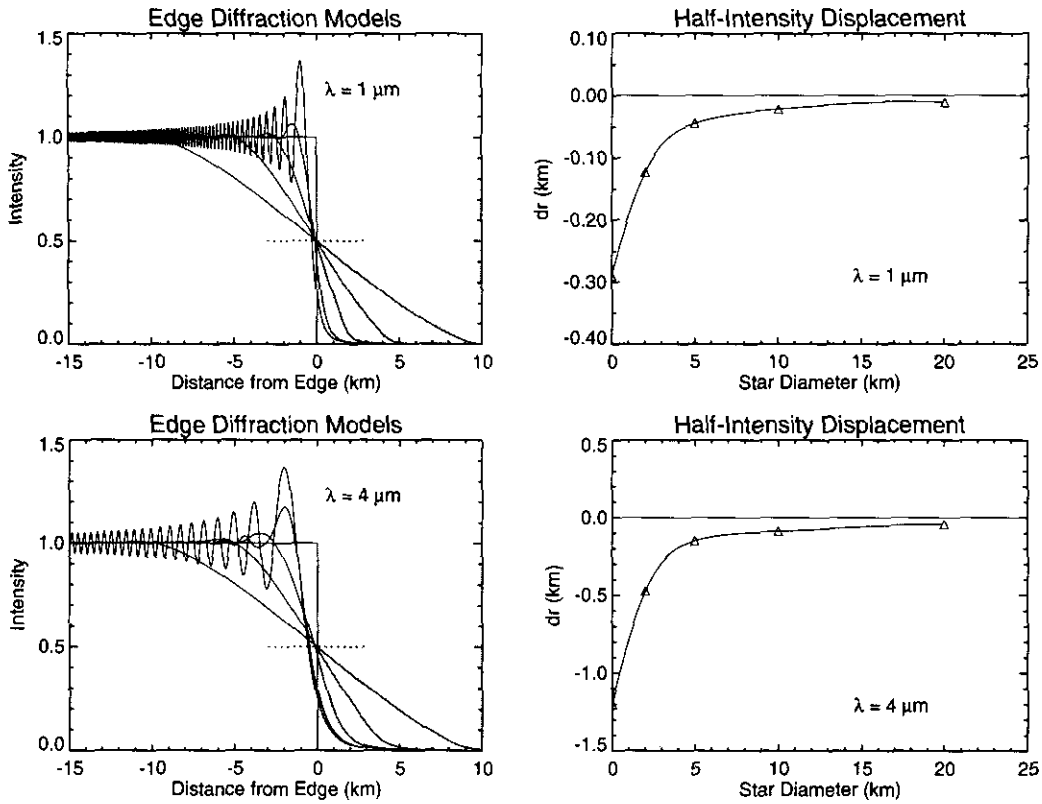


FIG. 5. Models illustrating the effects of diffraction and the projected stellar diameter at Saturn on ring feature positions for the 28 Sgr occultation. See text for details.

these circular features were obtained from the five NE data sets, including 42 of the eight chosen B Ring features. The SW data set employed here consists of 140 measurements of a subset of 22 circular features as reported by H93. The two Voyager occultations yielded a further 72 measurements of these features, for a grand total of 452 data points to be fitted. The number of points per feature ranges from 5 to 19.

### *3.3. Remeasurement of Voyager RSS and PPS Features*

Our analysis of the 28 Sgr data started with the Saturn pole vector and absolute ring radius scale determined by NCP. However, their analysis was based on measured radial offsets $\Delta R_0 = R_{RSS} - R_{PPS}$ between features using the previously published radius scales for both data sets, rather than on individual half-flux or half-optical-depth measurements. In order to obtain a set of Voyager data which could be included in our model fits, it was necessary therefore to remeasure both the RSS and the PPS occultation profiles in a manner which would be consistent with the half-flux measurements obtained from the 28 Sgr light curves. At the same time, we took the opportunity to add additional features to our ring catalog, as described above.

Because our astrometric model recomputes the radii of all features as a function of the assumed Saturn pole direction and possible corrections to the spacecraft trajectories, we chose to remeasure the RSS and PPS feature locations in time rather than in (nominal) radius. Both data sets had a radial resolution of ~1 km. In addition, as the 28 Sgr measurements refer to the half-flux points of abrupt optical depth transitions, we first converted the published Voyager optical depth profiles to predicted flux for the geometry of the 28 Sgr occultation, i.e., a ring opening angle $B = 25.404°$. The half-flux points were then determined from these rescaled light curves using the same procedure employed for the 28 Sgr data.

*3.3.1. Voyager 1 RSS data.* Measurements of feature locations in the Voyager 1 RSS occultation were based on the Export Tape produced by P. Rosen at Stanford University, which includes both raw and processed data, as well as ancillary information such as the Earth receive time and ring intercept time of the signal. We used the diffraction-corrected $X$-band optical depth profile for our

TABLE III
Mt. Palomar Observations of Saturn Ring Features

| | Ingress | | | | Egress | | | |
|---|---|---|---|---|---|---|---|---|
| Feature | UTC[a] | Longitude[b] | $\Delta R$ (km)[c] | $\Delta t$ (s)[c] | UTC[a] | Longitude[b] | $\Delta R$ (km)[c] | $\Delta t$ (s)[c] |
| 1 | 6:02:16.58 | 34.66 | 0.53 | −0.02 | 9:24:55.76 | 223.36 | −0.94 | −0.04 |
| 3 | 6:04:20.78 | 34.57 | 0.67 | −0.03 | 9:22:50.92 | 223.45 | −1.42 | −0.06 |
| 4 | 6:04:35.18 | 34.56 | 0.33 | −0.01 | 9:22:36.52 | 223.46 | −0.19 | −0.01 |
| 7 | | | | | 9:14:05.30 | 223.84 | −0.04 | 0.00 |
| 11 | | | | | 9:12:44.28 | 223.91 | 0.70 | 0.03 |
| 12 | | | | | 9:12:36.40 | 223.92 | −1.70 | −0.08 |
| 15 | 6:15:22.09 | 34.06 | −0.61 | 0.03 | 9:11:46.62 | 223.96 | −1.37 | −0.06 |
| 13 | 6:15:37.23 | 34.05 | −1.29 | 0.06 | 9:11:31.45 | 223.97 | −1.26 | −0.06 |
| 16 | 6:15:52.63 | 34.03 | −0.53 | 0.02 | 9:11:15.96 | 223.99 | −1.02 | −0.05 |
| 20 | 6:16:08.37 | 34.02 | −1.14 | 0.05 | 9:11:00.22 | 224.00 | −0.12 | −0.01 |
| 71[d] | 6:26:28.41 | 33.39 | −1.45 | 0.07 | 9:00:37.56 | 224.63 | −2.97 | −0.13 |
| 72[d] | 6:26:47.64 | 33.37 | −0.45 | 0.02 | 9:00:18.40 | 224.65 | 1.21 | 0.05 |
| 75[d] | 6:28:22.32 | 33.26 | 0.42 | −0.02 | 8:58:43.23 | 224.76 | −0.99 | −0.04 |
| 76[d] | 6:28:46.61 | 33.23 | −0.57 | 0.03 | 8:58:18.98 | 224.79 | 0.90 | 0.04 |
| 78[d] | | | | | 8:56:16.29 | 224.95 | −2.09 | −0.09 |
| 81[d] | 6:31:50.82 | 32.99 | −2.88 | 0.13 | 8:55:14.21 | 225.03 | 0.78 | 0.04 |
| 82[d] | 6:32:59.40 | 32.90 | −1.33 | 0.06 | 8:54:05.32 | 225.12 | 0.74 | 0.03 |
| 83[d] | 6:33:40.89 | 32.84 | −0.59 | 0.03 | 8:53:23.67 | 225.18 | 1.07 | 0.05 |
| 23 | 6:36:32.53 | 32.59 | −1.46 | 0.07 | | | | |
| 24 | 6:36:42.03 | 32.58 | −2.34 | 0.10 | | | | |
| 25 | 6:37:02.87 | 32.54 | −1.86 | 0.08 | | | | |
| 26 | 6:37:09.69 | 32.53 | −1.33 | 0.06 | | | | |
| 41 | 6:37:31.78 | 32.50 | −1.72 | 0.08 | 8:49:31.99 | 225.52 | −0.71 | −0.03 |
| 27 | 6:37:36.54 | 32.49 | −1.30 | 0.06 | 8:49:27.20 | 225.53 | −0.62 | −0.03 |
| 28 | 6:38:03.24 | 32.45 | −1.75 | 0.08 | | | | |
| 29 | 6:39:32.72 | 32.30 | −1.40 | 0.06 | 8:47:30.66 | 225.72 | −0.64 | −0.03 |
| 30 | 6:39:43.07 | 32.29 | −1.37 | 0.06 | 8:47:20.30 | 225.74 | −0.12 | −0.01 |
| 31 | 6:40:03.28 | 32.25 | −2.14 | 0.10 | 8:47:00.05 | 225.77 | −0.41 | −0.02 |
| 42 | 6:40:10.53 | 32.24 | −0.76 | 0.03 | 8:46:52.71 | 225.78 | −0.53 | −0.02 |
| 33 | 6:40:14.94 | 32.23 | −1.01 | 0.04 | 8:46:48.29 | 225.79 | −0.71 | −0.03 |
| 34 | 6:40:46.93 | 32.18 | −1.92 | 0.09 | 8:46:16.24 | 225.85 | −0.81 | −0.04 |
| 35 | 6:40:55.90 | 32.16 | −1.66 | 0.07 | 8:46:07.25 | 225.86 | −0.39 | −0.02 |
| 36 | 6:42:57.56 | 31.94 | −0.32 | 0.01 | 8:44:05.19 | 226.08 | 0.02 | 0.00 |
| 37 | | | | | 8:41:59.99 | 226.33 | −1.61 | −0.07 |
| 38 | 6:45:04.39 | 31.69 | −1.05 | 0.05 | 8:41:58.04 | 226.33 | 0.12 | 0.01 |
| 39 | 6:46:36.83 | 31.50 | −0.35 | 0.02 | 8:40:25.28 | 226.52 | −0.71 | −0.03 |
| 40 | 6:47:17.36 | 31.42 | −0.34 | 0.01 | 8:39:44.65 | 226.61 | −0.54 | −0.02 |
| 44 | 6:48:37.08 | 31.24 | 1.85 | −0.08 | 8:38:24.64 | 226.78 | −0.21 | −0.01 |

[a] 3 July 1989
[b] Measured in degrees from the ascending node of Saturn's equatorial plane (from Fit 13) on the Earth's B1950.0 equator.
[c] Residuals from Fit 13. See Table X.
[d] B Ring feature – not included in fit for pole and radius scale.

measurements, with a processing resolution of 1 km and a sampling interval of 0.5 km. This is the same dataset employed by NCP. The extinction efficiency of the processed RSS data ($Q_{RSS}$) was equal to 2, due to the separation of the Doppler-shifted scattered signal from the coherent directly transmitted signal (Marouf *et al.* 1983). Preliminary analysis of the Palomar 28 Sgr data (Nicholson *et al.* 1991) also indicated that $Q_{28Sgr} \approx 2$ for much of the C Ring and Cassini Division (where most of our features reside). Moreover, the abrupt signal changes at edges are almost entirely due to the direct signal, as the scattered (or diffracted) signal averages over a much wider region of the rings. Based on these considerations, we retained the RSS normal optical depths "as measured," and modeled the simulated light curve as

$$I_{RSS}(t) = e^{-\tau_{RSS}/\mu} \quad (1)$$

TABLE IV
McDonald Observatory 2.7-m Observations of Saturn Ring Features

| | Ingress | | | | Egress | | | |
|---|---|---|---|---|---|---|---|---|
| Feature | UTC[a] | Longitude[b] | $\Delta R$ (km)[c] | $\Delta t$ (s)[c] | UTC[a] | Longitude[b] | $\Delta R$ (km)[c] | $\Delta t$ (s)[c] |
| 1 | 6:01:29.70 | 34.54 | 0.55 | −0.03 | 9:24:18.33 | 223.83 | −0.98 | −0.04 |
| 3 | 6:03:33.88 | 34.45 | 0.40 | −0.02 | 9:22:13.16 | 223.92 | 0.03 | 0.00 |
| 4 | 6:03:48.30 | 34.44 | −0.27 | 0.01 | 9:21:58.67 | 223.93 | 0.23 | 0.01 |
| 7 | 6:12:17.07 | 34.03 | 1.01 | −0.04 | 9:13:25.81 | 224.35 | 0.26 | 0.01 |
| 11 | 6:13:37.77 | 33.96 | 1.06 | −0.05 | 9:12:04.45 | 224.42 | −0.98 | −0.04 |
| 12 | 6:13:45.48 | 33.95 | 1.70 | −0.08 | 9:11:56.59 | 224.43 | −2.21 | −0.10 |
| 15 | 6:14:35.06 | 33.90 | 1.78 | −0.08 | 9:11:06.72 | 224.48 | −0.37 | −0.02 |
| 13 | 6:14:50.21 | 33.89 | 0.96 | −0.04 | 9:10:51.52 | 224.49 | 0.13 | 0.01 |
| 16 | 6:15:05.62 | 33.88 | 1.50 | −0.07 | 9:10:35.92 | 224.50 | −0.99 | −0.04 |
| 20 | 6:15:21.35 | 33.86 | 1.17 | −0.05 | 9:10:20.08 | 224.52 | −1.21 | −0.06 |
| 71[d] | 6:25:41.72 | 33.19 | −1.80 | 0.08 | 8:59:55.92 | 225.20 | 6.20 | 0.28 |
| 72[d] | 6:26:00.76 | 33.16 | 3.56 | −0.16 | 8:59:36.18 | 225.22 | −1.24 | −0.06 |
| 75[d] | 6:27:35.78 | 33.04 | −2.01 | 0.09 | 8:58:00.79 | 225.34 | −1.66 | −0.07 |
| 76[d] | 6:28:00.04 | 33.01 | −1.98 | 0.09 | 8:57:36.39 | 225.37 | −1.45 | −0.07 |
| 78[d] | 6:30:02.23 | 32.85 | −1.96 | 0.09 | 8:55:33.59 | 225.54 | 1.76 | 0.08 |
| 81[d] | 6:31:04.08 | 32.76 | 2.06 | −0.09 | 8:54:30.89 | 225.63 | −4.63 | −0.21 |
| 82[d] | 6:32:13.10 | 32.66 | −4.88 | 0.22 | 8:53:22.08 | 225.73 | 1.87 | 0.08 |
| 83[d] | 6:32:54.53 | 32.60 | −2.21 | 0.10 | 8:52:40.19 | 225.79 | −0.06 | 0.00 |
| 23 | 6:35:46.10 | 32.33 | 1.76 | −0.08 | 8:49:47.45 | 226.06 | −0.49 | −0.02 |
| 24 | 6:35:55.59 | 32.31 | 1.20 | −0.05 | 8:49:38.00 | 226.08 | 0.96 | 0.04 |
| 25 | 6:36:16.50 | 32.28 | 0.63 | −0.03 | 8:49:16.95 | 226.11 | −0.24 | −0.01 |
| 26 | 6:36:23.33 | 32.27 | 0.98 | −0.04 | 8:49:10.06 | 226.12 | −0.15 | −0.01 |
| 41 | 6:36:45.45 | 32.23 | 0.39 | −0.02 | 8:48:47.80 | 226.16 | −1.07 | −0.05 |
| 27 | 6:36:50.25 | 32.22 | 0.02 | 0.00 | 8:48:43.03 | 226.17 | −0.20 | −0.01 |
| 28 | 6:37:16.92 | 32.17 | 0.79 | −0.04 | 8:48:16.16 | 226.21 | −0.64 | −0.03 |
| 29 | 6:38:46.48 | 32.02 | 1.56 | −0.07 | 8:46:46.10 | 226.37 | −0.58 | −0.03 |
| 30 | 6:38:56.87 | 32.00 | 0.94 | −0.04 | 8:46:35.70 | 226.39 | −0.30 | −0.01 |
| 31 | 6:39:17.10 | 31.96 | 0.20 | −0.01 | 8:46:15.40 | 226.43 | −0.10 | −0.01 |
| 42 | 6:39:24.31 | 31.95 | 2.64 | −0.12 | 8:46:08.05 | 226.44 | 0.12 | 0.01 |
| 33 | 6:39:28.82 | 31.94 | 0.27 | −0.01 | 8:46:03.61 | 226.45 | −0.22 | −0.01 |
| 34 | 6:40:00.81 | 31.88 | 0.12 | −0.01 | 8:45:31.44 | 226.51 | −0.68 | −0.03 |
| 35 | 6:40:09.80 | 31.86 | 0.16 | −0.01 | 8:45:22.42 | 226.52 | −0.27 | −0.01 |
| 36 | 6:42:11.63 | 31.63 | 0.93 | −0.04 | 8:43:19.87 | 226.76 | −1.86 | −0.08 |
| 37 | 6:44:16.59 | 31.37 | 0.23 | −0.01 | 8:41:14.35 | 227.02 | −1.23 | −0.06 |
| 38 | 6:44:18.61 | 31.36 | 0.34 | −0.02 | 8:41:12.40 | 227.02 | 0.73 | 0.03 |
| 39 | 6:45:51.18 | 31.16 | 1.20 | −0.05 | 8:39:39.31 | 227.23 | −0.51 | −0.02 |
| 40 | 6:46:31.73 | 31.07 | 2.07 | −0.09 | 8:38:58.51 | 227.32 | −1.04 | −0.05 |
| 44 | 6:47:51.73 | 30.88 | 0.72 | −0.03 | 8:37:38.34 | 227.51 | 1.81 | 0.08 |

[a] 3 July 1989
[b] Measured in degrees from the ascending node of Saturn's equatorial plane (from Fit 13) on the Earth's B1950.0 equator.
[c] Residuals from Fit 13. See **Table X**.
[d] B Ring feature – not included in fit for pole and radius scale.

where $\mu = \sin B = 0.4290$ for the 28 Sgr occultation and $t$ refers to Earth receive time of the signal. No averaging of the data was performed, and our measured half-flux times were interpolated between the 0.5 km ≃ 0.01 sec samples in the original file.

A total of 52 features were measured in the A and C Rings and in the Cassini Division, including the new features 13, 22, and 41–44. None of the B Ring features identified in the 28 Sgr data were unambiguously visible in the RSS data. A comparison of the half-flux times for the 46 features which were also measured by NCP (see their Tables III and VI) reveals differences ranging from −0.04 to +0.02 sec, but with 36 of the features falling within ±0.01 sec of the NCP times. We estimate the accuracy of the remeasured RSS times to be ±0.01 sec.

*3.3.2. Voyager 2 PPS data.* Measurements of feature locations in the Voyager 2 PPS data were based on the final calibrated data set delivered to the Planetary Data

TABLE V
IRTF Observations of Saturn Ring Features

| | Ingress | | | | Egress | | | |
|---|---|---|---|---|---|---|---|---|
| Feature | UTC[a] | Longitude[b] | $\Delta R$ (km)[c] | $\Delta t$ (s)[c] | UTC[a] | Longitude[b] | $\Delta R$ (km)[c] | $\Delta t$ (s)[c] |
| 1 | | | | | 9:28:12.25 | 223.82 | 1.18 | 0.05 |
| 3 | | | | | 9:26:08.12 | 223.92 | 0.03 | 0.00 |
| 4 | | | | | 9:25:53.81 | 223.93 | 1.35 | 0.06 |
| 7 | | | | | 9:17:25.33 | 224.41 | 0.60 | 0.03 |
| 11 | | | | | 9:16:04.75 | 224.50 | 2.02 | 0.09 |
| 12 | | | | | 9:15:56.94 | 224.51 | 0.41 | 0.02 |
| 15 | | | | | 9:15:07.46 | 224.56 | 1.91 | 0.09 |
| 13 | | | | | 9:14:52.34 | 224.57 | 1.54 | 0.07 |
| 16 | | | | | 9:14:36.88 | 224.59 | 0.72 | 0.03 |
| 20 | | | | | 9:14:21.23 | 224.61 | 1.82 | 0.08 |
| 71[d] | | | | | 9:04:01.29 | 225.39 | 0.02 | 0.00 |
| 72[d] | | | | | 9:03:42.01 | 225.42 | −0.25 | −0.01 |
| 75[d] | | | | | 9:02:07.48 | 225.56 | 4.24 | 0.19 |
| 76[d] | | | | | 9:01:43.18 | 225.60 | 3.11 | 0.14 |
| 78[d] | | | | | 8:59:40.91 | 225.79 | 0.17 | 0.01 |
| 81[d] | | | | | 8:58:38.89 | 225.89 | 0.05 | 0.00 |
| 82[d] | | | | | 8:57:30.37 | 226.00 | 3.60 | 0.16 |
| 83[d] | | | | | 8:56:48.74 | 226.08 | 1.79 | 0.08 |
| 23 | | | | | 8:53:57.00 | 226.39 | 1.20 | 0.05 |
| 24 | | | | | 8:53:47.53 | 226.41 | 1.10 | 0.05 |
| 25 | | | | | 8:53:26.66 | 226.45 | 1.18 | 0.05 |
| 26 | | | | | 8:53:19.79 | 226.46 | 0.72 | 0.03 |
| 41 | | | | | 8:52:57.67 | 226.50 | 0.26 | 0.01 |
| 27 | | | | | 8:52:52.90 | 226.51 | 0.44 | 0.02 |
| 28 | | | | | 8:52:26.24 | 226.57 | 1.53 | 0.07 |
| 29 | | | | | 8:50:56.63 | 226.75 | 0.85 | 0.04 |
| 30 | | | | | 8:50:46.28 | 226.77 | 1.14 | 0.05 |
| 31 | | | | | 8:50:26.13 | 226.81 | 2.27 | 0.10 |
| 42 | | | | | 8:50:18.74 | 226.83 | 0.83 | 0.04 |
| 33 | | | | | 8:50:14.31 | 226.84 | 0.25 | 0.01 |
| 34 | | | | | 8:49:42.34 | 226.91 | 0.52 | 0.02 |
| 35 | | | | | 8:49:33.36 | 226.93 | 0.92 | 0.04 |
| 36 | 6:47:08.59 | 29.68 | −0.70 | 0.03 | 8:47:31.48 | 227.20 | 1.06 | 0.05 |
| 37 | 6:49:14.09 | 29.38 | −1.89 | 0.09 | 8:45:26.50 | 227.50 | 0.96 | 0.04 |
| 38 | 6:49:16.06 | 29.37 | −0.59 | 0.03 | 8:45:24.52 | 227.51 | 1.87 | 0.08 |
| 39 | 6:50:49.00 | 29.14 | 0.47 | −0.02 | 8:43:51.86 | 227.75 | 1.56 | 0.07 |
| 40 | 6:51:29.66 | 29.03 | 2.64 | −0.12 | 8:43:11.25 | 227.85 | 1.64 | 0.07 |
| 44 | 6:52:50.15 | 28.80 | −1.92 | 0.09 | 8:41:51.19 | 228.07 | 0.20 | 0.01 |

[a] 3 July 1989. After Harrington *et al.* (1993).
[b] Measured in degrees from the ascending node of Saturn's equatorial plane (from Fit 13) on the Earth's B1950.0 equator.
[c] Residuals from Fit 13. See **Table X.**
[d] B Ring feature – not included in fit for pole and radius scale.

System's Ring Discipline Node at NASA Ames Research Center in 1991. This is essentially identical to the data set used by NCP. These data are in the form of stellar photon counts, corrected for background radiation from Saturn and the rings as described by Esposito *et al.* (1983), at the original sampling interval of 0.010 sec or ~0.1 km. These data were first averaged into nonoverlapping samples $n(t)$ every 0.09 sec, corresponding to an average radial resolution of 1 km. An absolute time scale was generated, based on the Flight Data System time tags in the original Experiment Records and the timing calibration described by NCP. (As discussed in Section II C and Appendix A of NCP, this involved a systematic correction of −1.19 sec relative to the original analyses of the PPS data.) The times refer to the spacecraft receive time of the photons.

Unlike the RSS data, the extinction efficiency of the PPS data is of order unity ($Q_{PPS} \simeq 1$) in most locations in the rings, due to the narrowness of the diffraction cone at

TABLE VI
ESO Observations of Saturn Ring Features

| Feature | Ingress | | | | Egress | | | |
|---|---|---|---|---|---|---|---|---|
| | UTC[a] | Longitude[b] | $\Delta R$ (km)[c] | $\Delta t$ (s)[c] | UTC[a] | Longitude[b] | $\Delta R$ (km)[c] | $\Delta t$ (s)[c] |
| ESO 1-m | | | | | | | | |
| 1 | 6:04:25.13 | 28.95 | 0.18 | −0.01 | 9:25:59.49 | 230.16 | 0.24 | 0.01 |
| 3 | 6:06:31.71 | 28.73 | −2.74 | 0.12 | 9:23:51.17 | 230.38 | 1.26 | 0.06 |
| 4 | 6:06:46.25 | 28.71 | −0.32 | 0.01 | 9:23:36.17 | 230.41 | −1.55 | −0.07 |
| 11 | 6:16:47.87 | 27.52 | 0.88 | −0.04 | | | | |
| 12 | 6:16:55.88 | 27.51 | −1.21 | 0.06 | 9:13:17.95 | 231.62 | −0.68 | −0.03 |
| 15 | 6:17:46.66 | 27.39 | −2.45 | 0.11 | | | | |
| 13 | 6:18:02.01 | 27.36 | 0.01 | 0.00 | 9:12:10.91 | 231.77 | −0.03 | 0.00 |
| 20 | 6:18:33.91 | 27.29 | −0.41 | 0.02 | | | | |
| 78[d] | 6:33:39.10 | 24.82 | 2.12 | −0.10 | | | | |
| 23 | | | | | 8:50:22.48 | 235.59 | 1.48 | 0.07 |
| 25 | | | | | 8:49:50.57 | 235.71 | −0.01 | 0.00 |
| 26 | | | | | 8:49:43.39 | 235.74 | 0.17 | 0.01 |
| 41 | | | | | 8:49:20.28 | 235.83 | 1.87 | 0.09 |
| 28 | | | | | 8:48:47.06 | 235.96 | −1.41 | −0.07 |
| 29 | | | | | 8:47:12.91 | 236.35 | −1.13 | −0.05 |
| 31 | | | | | 8:46:40.67 | 236.48 | −2.96 | −0.14 |
| 42 | | | | | 8:46:33.01 | 236.52 | −2.02 | −0.10 |
| 33 | | | | | 8:46:28.52 | 236.54 | 1.05 | 0.05 |
| 34 | | | | | 8:45:54.83 | 236.68 | 0.80 | 0.04 |
| 37 | 6:48:28.42 | 21.20 | 0.85 | −0.04 | 8:41:24.69 | 237.94 | 0.11 | 0.01 |
| 38 | 6:48:30.59 | 21.19 | −0.06 | 0.00 | 8:41:22.47 | 237.95 | −1.48 | −0.07 |
| 39 | | | | | 8:39:44.37 | 238.46 | −0.01 | 0.00 |
| 40 | | | | | 8:39:01.21 | 238.69 | −1.18 | −0.06 |
| ESO 2-m | | | | | | | | |
| 1 | 6:04:25.14 | 28.95 | −0.31 | 0.01 | 9:25:59.47 | 230.17 | 0.04 | 0.00 |
| 3 | 6:06:31.60 | 28.73 | −0.60 | 0.03 | | | | |
| 4 | 6:06:46.19 | 28.71 | 0.73 | −0.03 | | | | |
| 7 | 6:15:25.43 | 27.70 | −0.92 | 0.04 | | | | |
| 11 | 6:16:47.81 | 27.52 | 1.94 | −0.09 | 9:13:25.91 | 231.60 | −1.75 | −0.08 |
| 12 | 6:16:55.85 | 27.51 | −0.80 | 0.04 | | | | |
| 13 | 6:18:01.90 | 27.36 | 2.16 | −0.10 | | | | |
| 16 | 6:18:17.78 | 27.32 | 0.34 | −0.02 | | | | |
| 20 | 6:18:33.83 | 27.29 | 1.09 | −0.05 | | | | |
| 72[d] | 6:29:30.50 | 25.59 | −2.84 | 0.13 | | | | |
| 81[d] | 6:34:43.09 | 24.60 | 4.62 | −0.21 | | | | |
| 23 | 6:39:35.53 | 23.55 | 0.10 | 0.00 | 8:50:22.37 | 235.59 | −0.56 | −0.03 |
| 25 | 6:40:07.12 | 23.43 | −1.14 | 0.05 | 8:49:50.56 | 235.71 | 0.07 | 0.00 |
| 41 | 6:40:37.08 | 23.31 | 1.59 | −0.07 | 8:49:20.15 | 235.83 | −0.59 | −0.03 |
| 29 | 6:42:43.34 | 22.79 | −3.15 | 0.15 | 8:47:12.94 | 236.35 | −0.19 | −0.01 |
| 35 | | | | | 8:45:45.31 | 236.72 | 0.08 | 0.00 |
| 37 | | | | | 8:41:24.87 | 237.94 | 4.20 | 0.20 |
| 38 | | | | | 8:41:22.52 | 237.95 | −0.12 | −0.01 |

[a] 3 July 1989
[b] Measured in degrees from the ascending node of Saturn's equatorial plane (from Fit 13) on the Earth's B1950.0 equator.
[c] Residuals from Fit 13. See **Table X**.
[d] B Ring feature – not included in fit for pole and radius scale.

$\lambda = 0.27$ $\mu$m and the 1° field of view of the PPS instrument. For compatibility with the 28 Sgr data, therefore, we doubled the measured PPS optical depths before converting them to a synthetic light curve,

$$I_{\mathrm{PPS}}(t) = e^{-2\tau_{\mathrm{PPS}}/\mu}, \tag{2}$$

where the normal optical depth measured by the PPS instrument is given by (Esposito *et al.* 1983)

$$\tau_{PPS} = -\sin B_{PPS} \ln[n(t)/n_*]. \quad (3)$$

(Here, $n_* = 39.0$ is the unocculted stellar count rate and the factor of $\sin B_{PPS} = \sin 28.7° = 0.4802$ accounts for the incidence angle of the PPS experiment.) Our measured half-flux points were interpolated between samples of $I_{PPS}(t)$ to a precision of 0.01 sec.

A total of 65 features were measured in the PPS data, including 13 newly identified features in the inner B Ring. A comparison with the times for the 46 features measured by NCP, as listed in their Tables III and VI, showed differences ranging from −0.16 to +0.25 sec, but with a mean of −0.01 sec and a standard deviation of 0.09 sec, corresponding to ~1.0 km. The agreement is thus comparable to that found for the RSS data. As an additional consistency check with previous work, we remeasured 14 features in the older 1-km-resolution PPS data file used for the NCP analysis, finding an insignificant mean difference from the present results of $-0.002 \pm 0.037$ sec.

The remeasured half-flux times for both RSS and PPS data are given in Table II, along with our adopted a priori radii for these features (see below).

*3.3.3. Sensitivity to resolution.* It was shown above that the effect of the comparatively large angular diameter of 28 Sgr on the locations of the half-flux points for infinitely sharp edges is negligible (see Fig. 5). However, by no means are all the features in our ring catalog "infinitely sharp" on a scale of 1 km, and it might be suspected that measurements in Voyager data at 1-km resolution would differ in a systematic way from those obtained with the ~20-km resolution 28 Sgr data. In order to guard against this possibility, we also generated smoothed versions of the RSS and PPS synthetic light curves by convolving the functions $I_{RSS}(t)$ and $I_{PPS}(t)$ with the light distribution corresponding to a 20-km-diameter non-limb-darkened stellar disk. Figure 6 shows the resulting smoothed light curves for two ring features: the narrow ringlet in the C Ring at 1.470 $R_S$ and the Keeler Gap in the outer A Ring, overplotted on the 1-km-resolution data used for our measurements. Also plotted at the same scale are the Palomar ingress data for 28 Sgr, adjusted to the NCP radius scale. A close examination of this figure reveals that, as expected for these very sharp features, the half-flux points in the smoothed light curves coincide almost perfectly with the half-flux points in the original data, even though the width of the 1.47 $R_S$ ringlet is comparable to the projected stellar diameter and the Keeler Gap is not much wider. The similarity of the 28 Sgr light profile to the smoothed Voyager profiles is also striking.

Having established the basic similarity of the smoothed and 28 Sgr light curves, we then remeasured ~20 of our features using the smoothed Voyager data, including many of the less-sharp features in the C Ring. For the less-noisy RSS data, we found maximum shifts from the times in Table II of ±0.04 sec (~3 km), but 2/3 of the points fell within 0.01 sec of the previous results. For these more diffuse edges, there is a small systematic shift toward the low optical depth side, attributable to differences in the inferred "high" signal level. The largest shifts occurred for plateau features with sharp (~2 km wide) spikes in optical depth immediately adjacent to the edge, such as features 24 and 40. The spike disappears in the smoothed data, raising the "low" signal level as well. For the very sharp edges of isolated ringlets and narrow gaps, such as the example in Fig. 6, and for unresolved features such as 36, identical results were obtained from the 1-km and smoothed data.

The smoothed PPS data yielded very similar results, but with somewhat greater scatter attributable to the noisier nature of these data at the low optical depths which characterize the C Ring and Cassini Division. Maximum shifts were ±0.20 sec (2 km), but 2/3 of the points fell within 0.10 sec of the times in Table II. The same small systematic effects were noted in diffuse edges, whereas the sharpest edges gave shifts of ≤0.05 sec.

We conclude that no substantial *systematic* error is incurred by using RSS and PPS feature times derived from 1 km resolution data together with the 20 km resolution 28 Sgr measurements. An additional advantage of using the higher resolution Voyager times is that the same data may be used in analyses of future Earth-based occultation data, such as those recently acquired by HST (Elliot *et al.* 1992), for which the stellar angular diameters may be substantially smaller than that of 28 Sgr.

## 4. OCCULTATION GEOMETRY

Given the full set of ring event times for the 28 Sgr and Voyager occultations, the next step in the analysis was to determine the ring plane radius probed by each ring event as a function of the assumed pole direction of Saturn. Conceptually, the problem is quite straightforward: from the known position of the star, the observer, and the planet, one simply reconstructs the path of the unique ray from the star (or spacecraft) reaching an observer at a given time and computes the corresponding ring plane intercept point. One then adjusts the assumed direction of the planetary pole, the ring feature radii, and offsets to the planetary ephemeris to provide the best match between the observations and the modeled Saturn system geometry.

### *4.1. Geometric Algorithms*

The actual implementation of this procedure is quite a bit more complex. Among the complications are general

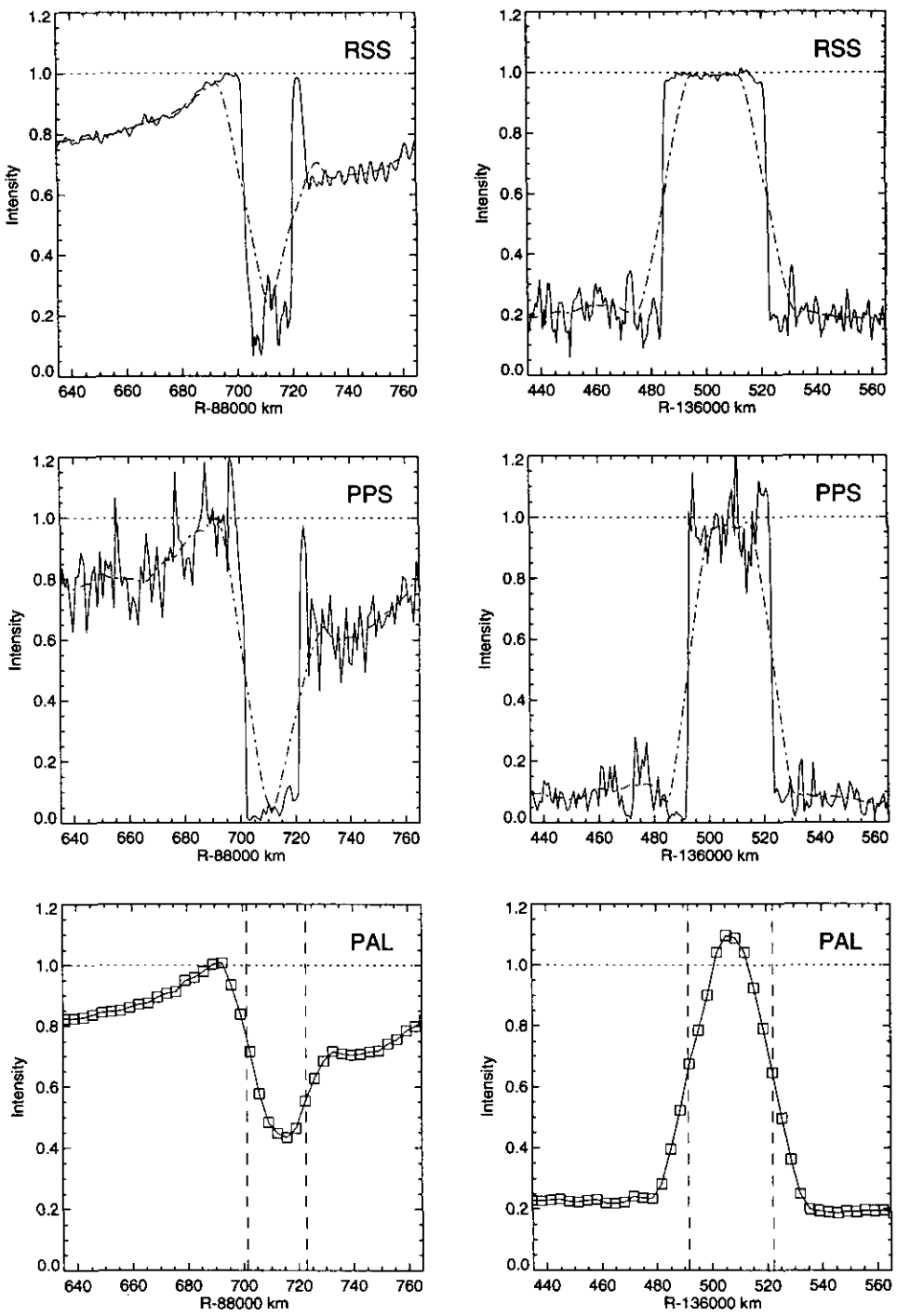


FIG. 6. Comparison of morphology of ring features from Voyager and 28 Sgr observations. The left column of figures shows occultation scans of the ringlet at 1.470 $R_S$ in the outer C Ring (features 58 and 59) from Voyager 1 RSS, Voyager 2 PPS, and 28 Sgr Palomar observations. The RSS and PPS profiles have been converted from optical depth to synthetic light curves appropriate to the geometry of the 28 Sgr occultation, and the smoothed profiles superimposed on the Voyager data simulate the effects of convolution with the 20-km projected diameter of 28 Sgr. Significant structural detail is lost in the smoothing process, but the convolved profiles closely resemble the 28 Sgr observations. The right column of figures shows the Keeler Gap (features 1 and 2). The measured half-intensity points for these features in the Palomar profiles are shown by vertical dashed lines. All data have been adjusted to the NCP radius scale.

relativistic bending of the rays by an oblate planet, resulting in transverse displacements of the ring intercept point by 38–42 km for rays grazing Saturn's limb; the motion of Saturn with respect to the system barycenter induced by the satellites, especially Titan; and the proper treatment of precession, nutation, aberration and the light travel time from the ring plane intercept point to the topocentric location of the observer. Historically, most Earth-based stellar occultation observations have been reduced using a "sky-plane" approximation, based on the "fundamental plane" described by Smart (1977) for lunar occultations and adapted for stellar occultations by Elliot *et al.* (1978) and others. As long as the angular diameter of the ring system is small, and the light travel time from the sky-plane to the ring plane is negligible—as is the case for Uranian ring occultations, for example—then the straightforward sky-plane approximation is quite adequate.

Saturn's rings, however, subtend an angular diameter of $\theta_R \simeq 42$ arcsec, or $2 \times 10^{-4}$ radians, and the light travel time from sky-plane to rings $\delta t$ can be as much as 0.41 sec (although at most 0.23 sec for 28 Sgr, at C Ring ingress). At a typical sky-plane velocity of the star relative to Saturn of $v_{sky} = 20$ km/sec and a distance of $\Delta = 9.0$ AU, neglect of these effects can lead to errors of $O(0.25\Delta\theta_R^2) \simeq 14$ km and $O(v_{sky}\delta t) \simeq 8$ km. In order, therefore, to achieve sub-km accuracy in the reconstruction of an occultation chord spanning the full ring system (~280,000 km), it was necessary to reconsider carefully the approximations implicit in our preexisting computer models.

Initial comparisons of astrometric calculations using independent computer codes written by three coauthors and the SW group showed an unacceptably large scatter (i.e., several kilometers) in computed ring plane radii, prompting us to examine afresh the derivations behind each of the algorithms. Ultimately, we developed a rigorous, nonrelativistic 3-dimensional vector approach, based on an algorithm used earlier for spacecraft occultation analyses (STH, French *et al.* 1988, Rosen 1989, and NCP) and extended to include additional geometrical effects specific to Earth-based occultations such as topocentric corrections for the observer's location, offsets to allow for a priori ephemeris errors, and the general relativistic deflection of light. To check the new algorithm, we compared its results with those obtained using a revised version of the sky-plane code previously employed for Earth-based Uranus occultations (French *et al.* 1986, 1988), obtaining agreement in the calculated ring radii at the 0.02-km level. The revisions to the sky-plane code incorporated corrections for several minor errors or inconsistencies uncovered during the course of this study: errors which were insignificant at Uranus but amounted to several kilometers at Saturn.

In Appendix A, we present a detailed description of the vector algorithm, which can be used for both Earth-based and spacecraft occultation reductions. For completeness, we include a summary of the sky-plane approach. We also note errors uncovered in earlier formulations of occultation reductions; most of these errors involved the treatment of stellar aberration, light travel time, and parallax corrections. Appendix B presents detailed calculations for two of the ring features used in this analysis, using the vector approach, as well as the results of various sensitivity tests and computer code comparisons. These results serve to illustrate the actual method used for our final solutions and also as benchmarks against which to test future codes.

Table VII contains a summary of the fundamental geometrical and physical constants adopted for our analysis of both the 28 Sgr and Voyager 1 and 2 observations. For all of our astrometric solutions, we have used the JPL DE-130 (B1950.0) planetary ephemeris (Standish 1987, 1990) and ephemerides for the principal Saturnian satellites obtained from the Navigational and Ancillary Information Facility of the Jet Propulsion Laboratory (NAIF/JPL) (see Acton 1990). We elected to perform the entire calculation in B1950.0 coordinates because the Voyager 1 and 2 trajectory files provided by the Voyager Navigation Team are in B1950.0 coordinates. We wished to avoid the possibility of contaminating our results with inadvertent systematic errors which could have resulted from inconsistent conversions of the planetary ephemeris and the spacecraft trajectories. (See Standish *et al.* (1992) for a summary of the procedure required to convert the B1950.0-based ephemerides to J2000.0.) For ease of comparison with the results of the H93 analysis, however, we present our final solution for Saturn's pole in B1950.0 and J2000.0 coordinates.

The spacecraft trajectories are the same as those used by NCP, and represent the "official" trajectory reconstructions provided by the Voyager Navigation Team to the RSS and UVS science teams in 1981. (Work currently in progress of JPL may eventually lead to the release of revised trajectories for both spacecraft, but these results are not yet available.) The coordinates for δ Sco are also from NCP, and the Deep Space Network ground station position is taken from the *Astronomical Almanac*. The coordinates of 28 Sgr are from the Perth 70 catalog, including proper motion, but have been adjusted to remove the "E-terms" in the catalog position for compatibility with the DE-130 planetary ephemeris. Any small error in the adopted position of 28 Sgr would of course be absorbed in the planetary ephemeris correction determined as part of our geometric solutions.

### *4.2. Determination of Standard Voyager Feature Radii*

The standard feature radii adopted as a priori values for all of our fits were derived from the remeasured RSS

TABLE VII
Adopted Geometrical and Physical Parameters

| | | |
|---|---|---|
| **Saturn System** | | |
| $GM_{Saturn}$ | $3.793120 \times 10^7$ km$^3$s$^{-2}$ | as adopted by Nicholson and Porco, 1988 |
| $J_2$ | $1.6297 \times 10^{-2}$ | as adopted by Nicholson and Porco, 1988 |
| $J_2$ reference radius | 60330 km | |
| Planetary ephemeris | JPL DE-130 | Standish, 1987, 1990 |
| Satellite ephemerides | | JPL/NAIF File SAT018H.BSP (Acton 1990) |
| Satellite masses | $GM$ (km$^3$s$^{-2}$) | JPL/NAIF File SAT018H.BSP (AIAA/NASA, 1990) |
| Mimas | 2.5 | |
| Enceladus | 5.6 | |
| Tethys | 44.1 | |
| Dione | 77.3 | |
| Rhea | 154.1 | |
| Titan | 8977.7 | |
| Hyperion | 1. | |
| Iapetus | 117.4 | |
| **Earth Figure** | | |
| Semimajor axis | 6378.137 km | Archinal, 1992 |
| Flattening ($f$) | 1/298.257 | Archinal, 1992 |
| Earth figure | MERIT 1983 | Archinal, 1992 |
| **28 Sgr** | | |
| $\alpha$(B1950.0) | $18^h\ 43^m\ 19\overset{s}{.}770$ | Perth 70 catalog[b], epoch 1989.5 |
| $\delta$(B1950.0) | $-22°\ 26'\ 46\overset{''}{.}91$ | |
| $\alpha$(B1950.0)[a] | $18^h\ 43^m\ 19\overset{s}{.}7946475$ | (used for all fits in this paper) |
| $\delta$(B1950.0)[a] | $-22°\ 26'\ 46\overset{''}{.}88424$ | |
| $\mu_\delta$ | $0\overset{''}{.}00$/yr | Sky Catalogue 2000.0[c] |
| $\mu_\alpha$ | $+0\overset{''}{.}002$/yr | Sky Catalogue 2000.0[c] |
| $1/\pi$ | 150 pc | Sky Catalogue 2000.0[c] |
| **RSS** | | |
| Voyager 1 trajectory | T810308 | Nicholson *et al.*, 1990b. |
| DSS-63 latitude | 40° 25′ 48″. | *Astronomical Almanac*, 1984. |
| DSS-63 W. longitude | 4° 14′ 54″. | (geodetic) |
| DSS-63 Altitude (m) | 774 | |
| **PPS** | | |
| Voyager 2 trajectory | T811001 | Nicholson *et al.*, 1990b. |
| $\alpha[\delta$ Sco] (B1950.0) | $15^h\ 57^m\ 22\overset{s}{.}295$ | Heliocentric position, epoch 1981.8; FK4 catalog |
| $\delta[\delta$ Sco] (B1950.0) | $-22°\ 28'\ 52\overset{''}{.}16$ | |
| $\alpha[\delta$ Sco] (B1950.0) | $15^h\ 57^m\ 22\overset{s}{.}2979$ | Saturnicentric position, heliocentric frame |
| $\delta[\delta$ Sco] (B1950.0) | $-22°\ 28'\ 52\overset{''}{.}172$ | (used for all fits in this paper) |

[a] Epoch 1989.5; includes a correction for E terms of $(+0\overset{s}{.}02464750, +0\overset{''}{.}02576020)$ to the catalog place.
[b] Høg and von der Heide, 1976.
[c] Hirshfeld and Sinnott, 1982.

and PPS feature times given in Table II, using the Saturn pole determined by NCP and the vector code used for the astrometric fits. These standard radii are also listed in Table II. Except for the B Ring features (71–83), for which only PPS measurements were made, the standard radii are simply the average of the RSS and PPS radii and agree closely with the radii tabulated by NCP (see their Tables III and VI). The rms radius residual for the 59 measurements of the 30 non-B Ring circular features in Table II relative to their average radii was found to be $\Delta r = 0.71$ km per degree of freedom. This is consistent with the postfit rms residual radius difference $< (R_{RSS} - R_{PPS})^2 >^{1/2} \simeq 2^{1/2}\Delta r = 0.9$ km found by NCP. Besides providing an indication of the circularity of the features (albeit not an absolute proof with only two data points), the rms residual provides an objective estimate of the rms errors in our Voyager feature measurements of ~0.7 km.

References in Section 5 to the differences between fitted radii and "Voyager radii" (e.g., in Fig. 11), or to

the "NCP radius scale" refer strictly to these standard radii, rather than to the slightly different (and less accurate) numerical values given by NCP. (See Fit 1 in Table IX.) Note that for eccentric features such as the Maxwell and Titan (or Colombo) ringlets, or the A and B Ring outer edges, the standard radii are not generally equal to the mean radii, which must be derived from noncircular fits to all available data.

### *4.3. Precession of Saturn's Pole*

The possibility of forced precession of Saturn's pole, or of a free precession analogous to the Earth's Chandler wobble, is addressed by H93. They conclude that the period of the latter is too short to influence the mean ring plane, and estimate a period of $7 \times 10^6$ years for the solar-induced precession. This would result in a displacement in the pole of ~0.7″ over the period of 9 years between the Voyager and 28 Sgr epochs, which is small compared to the uncertainty either in the NCP pole or in our adopted solution below. However, this calculation neglects the influence of the solar torque on the equatorial satellites, principally Titan, which effectively increases Saturn's $J_2$ by a factor of ~4 and reduces the precession period accordingly (Ward 1975).

We may estimate the actual forced precession rate of the Saturn system pole as follows. The torque exerted on Saturn's oblate figure by the Sun, averaged over an orbit, is given by

$$T = -\frac{3GM_S M_\odot J_2 R_S^2}{4a_S^3} \sin 2\varepsilon, \tag{4}$$

where $M_S$, $R_S$, $\varepsilon$, and $J_2$ are the mass, equatorial radius, obliquity, and second zonal gravity coefficient of Saturn, respectively, $M_\odot$ is the mass of the Sun, and $a_S$ is the semimajor axis of Saturn's orbit. In terms of the planet's polar ($C$) and equatorial ($A$) moments of inertia,

$$J_2 = \frac{C - A}{M_S R_S^2}. \tag{5}$$

A similar torque is also exerted by the Sun on the orbits of the equatorial satellites, which may conveniently be included in the above expression by adding the contribution of each satellite's orbit (treated here as a circular hoop of mass $m_j$ and radius $a_j$) to the effective $J_2$ of the system:

$$J_2' = J_2 + \frac{1}{2}\sum_j \frac{m_j a_j^2}{M_S R_S^2} \tag{6}$$

Titan is responsible for over 90% of the satellite torque.

These relatively weak Sun–satellite torques are effectively communicated to the planet via the much stronger planet–satellite torques due to Saturn's oblateness, which lead to the satellites' maintaining their constant, near-zero inclinations to the planet's equatorial plane despite the steady precession of the planet's spin axis in inertial space (Goldreich 1965). More distant nonequatorial satellites such as Phoebe do not contribute appreciably to the effective torque on the system, as their orbits precess independently under solar perturbations, and thus do not maintain a fixed inclination to the planet's equator (e.g., Burns 1977). Iapetus is unique among solar system satellites in occupying an intermediate situation, precessing about a Laplace plane inclined ~15° to Saturn's equator (Ward 1981). We handle the contribution of Iapetus (~5% of the total satellite torque and second only to Titan's) by reducing its effective contribution to $J_2$ by a factor of $\sin 2(\varepsilon - i_L)/\sin 2\varepsilon$, where $i_L = 14.84°$ is the inclination of its Laplace plane to Saturn's equator (Ward 1981). This is justified a posteriori by the relatively rapid (3000 years) precessional motion of Iapetus' orbit compared with the planet's spin axis precession rate.

The precession period of the system is then determined by the augmented torque acting on the sum of Saturn's spin angular momentum and the combined orbital angular momenta of the equatorial satellites,

$$P = \frac{2\pi L_{\text{tot}} \sin \varepsilon}{T}, \tag{7}$$

where

$$\begin{aligned} L_{\text{tot}} &= C\omega + \sum_j m_j n_j a_j^2 \\ &= \gamma' M_S R_S^2 \omega. \end{aligned} \tag{8}$$

Here, $\omega$ is Saturn's spin angular velocity and the $n_j$ are the satellite mean motions. The effective moment of inertia factor,

$$\gamma' = \gamma + \sum_j \frac{m_j a_j^2 n_j}{M_S R_S^2 \omega}, \tag{9}$$

where $\gamma = C/M_S R_S^2$. (The Iapetus contribution is reduced by a factor of $\sin(\varepsilon - i_L)/\sin \varepsilon$.) Combining the above expressions and using Kepler's third law, we have the more compact result (Ward 1975),

$$P = \frac{4\pi\gamma'\omega}{3J_2' n_S^2 \cos \varepsilon}, \tag{10}$$

where $n_S$ is Saturn's orbital mean motion.

Using current values for Saturn system parameters (Table VII) and the moment of inertia derived from interior models by Hubbard and Marley (1989), we obtain numerical values of

$$J_2' = J_2 + 0.05164 = 0.06794, \quad (11)$$

$$\gamma' = \gamma + 0.00278 = 0.22270, \quad (12)$$

and

$$P = 1.5603 \times 10^6(\cos \varepsilon)^{-1} \text{ years}. \quad (13)$$

(We have rescaled the polar moment of inertia, $C = 0.22037 M_S R_S^2$, given by Hubbard and Marley to our adopted value for Saturn's equatorial radius to give $\gamma = 0.21992$.) Note that although the contribution from the satellite torques increases the effective $J_2$ by almost a factor of 4, their contribution to the system's angular momentum is only ~1%. Although the current obliquity of Saturn is 26.73°, this quantity will change over the course of Saturn's orbital precession period of ~50,400 years (Brouwer and Clemence 1961). During this period, Saturn's orbital plane precesses about the invariable plane of the Solar System, maintaining an almost constant inclination to the latter of 0.90°. Because of the almost 40-fold disparity between orbital and spin axis precession periods, we assume that the spin axis will maintain an essentially fixed obliquity, $\varepsilon = 27.34°$ with respect to the invariable plane, precessing about the invariable pole with a period $P = 1.7565 \times 10^6$ years. The largest uncertainties in this rate are probably due to Saturn's moment of inertia, which may possibly be in error by as much as 10%, and to our approximate treatment of the effective Iapetus torque ($\lesssim$5%).

The corresponding motion of Saturn's pole on the sky is given, in B1950.0 coordinates, by

$$\begin{aligned} d\alpha_p/dt &= -0.00057699° \text{ years}^{-1} \\ \text{and } d\delta_p/dt &= -0.00006604° \text{ years}^{-1}, \end{aligned} \quad (14)$$

where time is measured in Julian years. We shall see that it is important to take this motion into account when determining Saturn's pole direction from Voyager and 28 Sgr occultation observations.

## 5. SATURN POLE AND RADIUS SCALE

An accurate radius scale for Saturn's rings is essential for detailed dynamical investigations of the rings, as well as accurate intercomparisons between Voyager and Earth-based observations. As a practical matter, the determination of the radius scale is strongly coupled to the assumed pole direction of the mean ring plane, and thus we must in the end solve simultaneously for both the pole and radius scale. Prior to the Voyager encounters with Saturn, the most detailed investigation of Saturn's pole was that of Kozai (1957), who determined the pole direction from an extensive set of Earth-based astrometric observations of Saturn's satellites. Subsequently, Holberg (1983, private communication), STH, and NCP used Voyager occultation data to refine the pole direction and radius scale. (These results are shown in Fig. 8 and listed in Table VIII, along with the values from other fits described below.) The Kozai (1957) pole direction differed substantially from the STH and NCP Voyager results. However, NCP demonstrated that their derived radius scale (and hence the corresponding pole direction) was corroborated by detailed matches between linear models of density wave trains and the Voyager occultation observations. Hence, we took as our starting point the NCP Saturn pole and radius scale.

We performed a suite of fits, first to the 28 Sgr data and Voyager data separately, and then to the combined data sets, as described below. The sky-plane and barycentric vector algorithms described in Appendix A were incorporated into a flexible ring orbit fitting computer code using specified sets (or subsets) of the Earth-based and Voyager occultation event times. By minimizing the sum of squared residuals in either ring plane radius or ring event time, the least squares solution could be determined by optimizing any desired combination of the following parameters: planet pole direction, ring orbital elements, corrections to the relative star and planet positions, offset times to be applied to individual observations, and Voyager trajectory offsets. The sensitivity of the results to a variety of effects such as motion of Saturn with respect to the system barycenter, the treatment of general relativistic deflections, and the precession of Saturn's pole could be easily determined by varying the conditions of the fit.

The code has been tested extensively, both via comparisons with the SW group using identical input data sets and fit conditions, and via comparisons between the results of fits using the barycentric vector algorithm and the sky-plane approach. These test cases are documented in Appendix B. Unless otherwise noted, all of the orbit fits presented below were obtained using the Wellesley College version of the barycentric vector code. A 3-D ephemeris for the eight main Saturnian satellites was used, general relativistic deflections were computed taking account of the oblateness ($J_2$) of the planet, and the sum of squared residuals in ring plane radius (rather than ring event time) was minimized.

### *5.1. Fits to the 28 Sgr Observations*

In order to determine both the pole and ring radii from the observations, it was desirable to include as many ring features as possible over the full range of radii from the inner C Ring to the outer A Ring. At the same time, inclusion of noncircular features in the fits could intro-

TABLE VIII
Saturn Pole Fits

| Fit[a] | $\alpha_P$(B1950.0) | $\delta_P$(B1950.0) | rms (km)[b] | Comments |
|---|---|---|---|---|
| | | **Earth-based satellite data** | | |
| Kozai | $38.432 \pm 0.023$ | $83.3071 \pm 0.0036$ | | Kozai (1957)[c] |
| HT | $38.474 \pm 0.014$ | $83.3198 \pm 0.0016$ | | Harper and Taylor (1993) |
| | | **Voyager data only** | | |
| UVS | $38.438 \pm 0.064$ | $83.327 \pm 0.002$ | | Holberg (1983)[c] |
| STH | $38.409 \pm 0.016$ | $83.324 \pm 0.002$ | 2 | |
| NCP | $38.4107 \pm 0.0006$ | $83.32352 \pm 0.00002$ | 0.64 | |
| NCP | $38.4107 \pm 0.0102$ | $83.32352 \pm 0.00033$ | 0.64 | *a priori* trajectory errors included |
| Fit 8 | $38.4108 \pm 0.0010$ | $83.32352 \pm 0.00004$ | 0.646 | reproduces NCP fit |
| Fit 9 | $38.4111 \pm 0.0009$ | $83.32357 \pm 0.00004$ | 0.690 | fit to remeasured data |
| Fit 10 | $38.22 \pm 0.07$ | $83.333 \pm 0.004$ | 0.630 | solves for trajectory errors |
| | | **28 Sgr data only** | | |
| Fit 3 | $38.415 \pm 0.008$ | $83.3216 \pm 0.0011$ | 1.749 | radii fixed at NCP |
| Fit 5 | $38.25 \pm 0.05$ | $83.399 \pm 0.023$ | 1.271 | NE & SW data |
| Fit 6 | $38.12 \pm 0.07$ | $83.413 \pm 0.024$ | 1.202 | NE data only |
| Fit 7 | $38.23 \pm 0.15$ | $83.408 \pm 0.069$ | 1.535 | SW data only |
| | | **Voyager and 28 Sgr data** | | |
| Fit 11 | $38.4084 \pm 0.0009$ | $83.32342 \pm 0.00003$ | 1.309 | |
| Fit 12 | $38.4101 \pm 0.0035$ | $83.32354 \pm 0.00017$ | 1.295 | solves for trajectory errors |
| Fit 13[d] | $38.4168 \pm 0.0035$ | $83.32329 \pm 0.00017$ | 1.295 | includes Saturn pole precession |

[a] See **Table IX** for fit definitions.
[b] rms residual per degree of freedom.
[c] As reported by STH.
[d] Adopted fit.

duce significant systematic errors, since for the present work we modeled all fitted features as having equatorial, circular orbits. Based on the NCP measurements of features in the Voyager data, and the results of several preliminary fits, we culled our fitted data set of a number of possibly noncircular features. Furthermore, although B Ring features were measured in a number of the NE data sets (cf. Tables III–VI), they have not been included as weighted points in our astrometric solutions for several reasons: (i) they are more difficult to measure precisely and have larger intrinsic measurement errors than the other features; (ii) RSS measurements are not available for features in most of the B Ring because of limited SNR in the ocultation observations at high optical depth; and (iii) for the features we could measure in the PPS data, the radii differed substantially (by 5–10 km) from their counterparts in the 28 Sgr data.

In the end, we selected 30 "quasi-circular" features to be included in the astrometric fits: 20 features in the C Ring, 6 in the Cassini Division, and 4 in the A Ring. For convenient reference, these are identified by an asterisk in the first column of Table II. We began our astrometric investigations with a series of fits to the 28 Sgr observations of these 30 features. Our objectives were to determine whether the results were consistent with earlier determinations of the pole and radius scale (most notably the NCP and STH results), and to ascertain whether the Earth-based occultation observations alone could provide significant constraints on the pole direction and radius scale. The a priori radius scale for the rings was determined by fixing the pole at the NCP value, setting the Voyager trajectory offsets to zero, and fitting the remeasured Voyager data to determine the standard Voyager feature radii (Fit 1 in Table IX).

To set the general scene, we first allowed only the most essential model parameters to be determined by the fit, and held the Saturn pole direction and ring plane radius scale fixed at the NCP values. Because of the large a priori astrometric uncertainties (~0.2″) in the positions of the star and Saturn, we utilized two degrees of freedom in the equations of condition to determine from the 28 Sgr observations the best-fitting constant sky-plane offsets to the Saturn ephemeris, $f_0$ and $g_0$ (see Eq. (A15) in Appendix A). Also, as described previously, the absolute timing for the ESO observations could be in error by an unknown constant offset, although we believe that the time *differences* between measured features are quite precise. Thus, in all of our fits utilizing the ESO observations, we

TABLE IX
Description of Model Fits

| Fit | Data fitted | | | | | Fit parameters | | | | | Comments |
|---|---|---|---|---|---|---|---|---|---|---|---|
| | NE[a] | SW[b] | Vgr[c] | B Ring[d] | No. | Radii[e] | Pole[f] | $\Delta T$'s[g] | No. | rms (km)[h] | |
| 1 | – | – | × | – | 59 | × | – | – | 30 | 0.711 | standard radii[i] |
| 2 | × | × | – | – | 338 | – | – | A | 9 | 1.865 | |
| 3 | × | × | – | – | 338 | – | × | A | 11 | 1.749 | |
| 4 | × | × | – | – | 338 | × | – | A | 39 | 1.289 | |
| 5 | × | × | – | – | 338 | × | × | A | 41 | 1.271 | large radius, pole $\sigma$'s |
| 6 | × | – | – | – | 198 | × | × | B | 36 | 1.202 | large radius, pole $\sigma$'s |
| 7 | – | × | – | – | 140 | × | × | – | 22 | 1.535 | large radius, pole $\sigma$'s |
| 8 | – | – | × | – | 48 | × | × | – | 26 | 0.646 | re-doing NCP fit[j] |
| 9 | – | – | × | – | 59 | × | × | – | 32 | 0.690 | Voyager only fit |
| 10 | – | – | × | – | 59 | × | × | C | 34 | 0.630 | Voyager only fit |
| 11 | × | × | × | – | 397 | × | × | A | 41 | 1.309 | |
| 12 | × | × | × | – | 397 | × | × | D | 43 | 1.295 | no pole precession |
| 13 | × | × | × | – | 397 | × | × | D | 43 | 1.295 | adopted fit[k] |
| 14 | × | – | – | × | 42 | × | –[l] | –[l] | 8 | 2.675 | B Ring only |
| 15–22 | × | × | × | – | 397 | × | × | D | 43 | –[m] | Voyager offsets |
| 23–26 | × | × | × | – | 397 | × | × | D | 43 | –[n] | satellite tests |
| 27–28 | × | × | × | – | 397 | × | × | D | 43 | –[o] | gravitational bending |

[a] PAL + MCD + IRTF + ESO1 + ESO2.
[b] MMT + CAT + KP + SPM + UKIRT + CTIO.
[c] RSS + PPS.
[d] Features 71–83.
[e] For 30 rings (except for Fit 14): default values from **Table II**.
[f] Default is NCP pole.
[g] A = ESO1/ESO2/MMT/CAT/KPi/KPe/SPM
B = ESO1 and ESO2 only
C = Voyager 1 and 2 along-track offset times.
D = ESO1/ESO2/MMT/CAT/KPi/KPe/SPM + RSS/PPS.
[h] rms residual per degree of freedom.
[i] Fit to determine feature radii in **Table II**, based on NCP pole.
[j] Fit used original data from NCP, rather than from **Table II**.
[k] Fit parameters in **Table X**.
[l] Parameters held fixed at values from Fit 13.
[m] Voyager 1 and 2 radial and vertical offsets. See **Table XI** for results of individual fits.
[n] Satellite motion sensitivity tests. See **Table XI** for results of individual fits.
[o] Gravitational bending sensitivity tests. See **Table XI** for results of individual fits.

included as fitted parameters "station offset times" to be added to the measured event times for ESO1 and ESO2. Finally, rather than using atmospheric spike correlation times to calibrate the SW data sets, we chose to fit for station offset times to all observations for which reliable instrumental absolute timing calibrations were unavailable: these were MMT, CAT, SPM, KPi, and KPe. (As described by H93, separate timing corrections were necessary for Kitt Peak ingress and egress observations.)

The characteristics of this solution (Fit 2) are summarized in Table IX, and the rms ring plane radius residuals are displayed in Fig. 7, along with the results from additional fits described below. The rms radius residual for this fit was 1.865 km, somewhat larger than the estimated uncertainty of 1.0 km associated with measuring the features. The radii of individual ring events calculated from Fit 2 showed systematic differences of up to several kilometers from the NCP values, particularly in the inner C

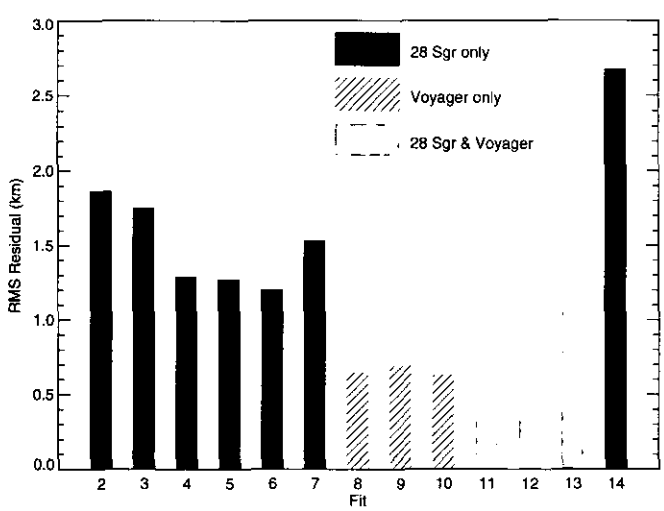


FIG. 7. Ring-plane radius residuals (rms) from a series of fits to 28 Sgr and Voyager observations. See **Table IX** and the text for details.

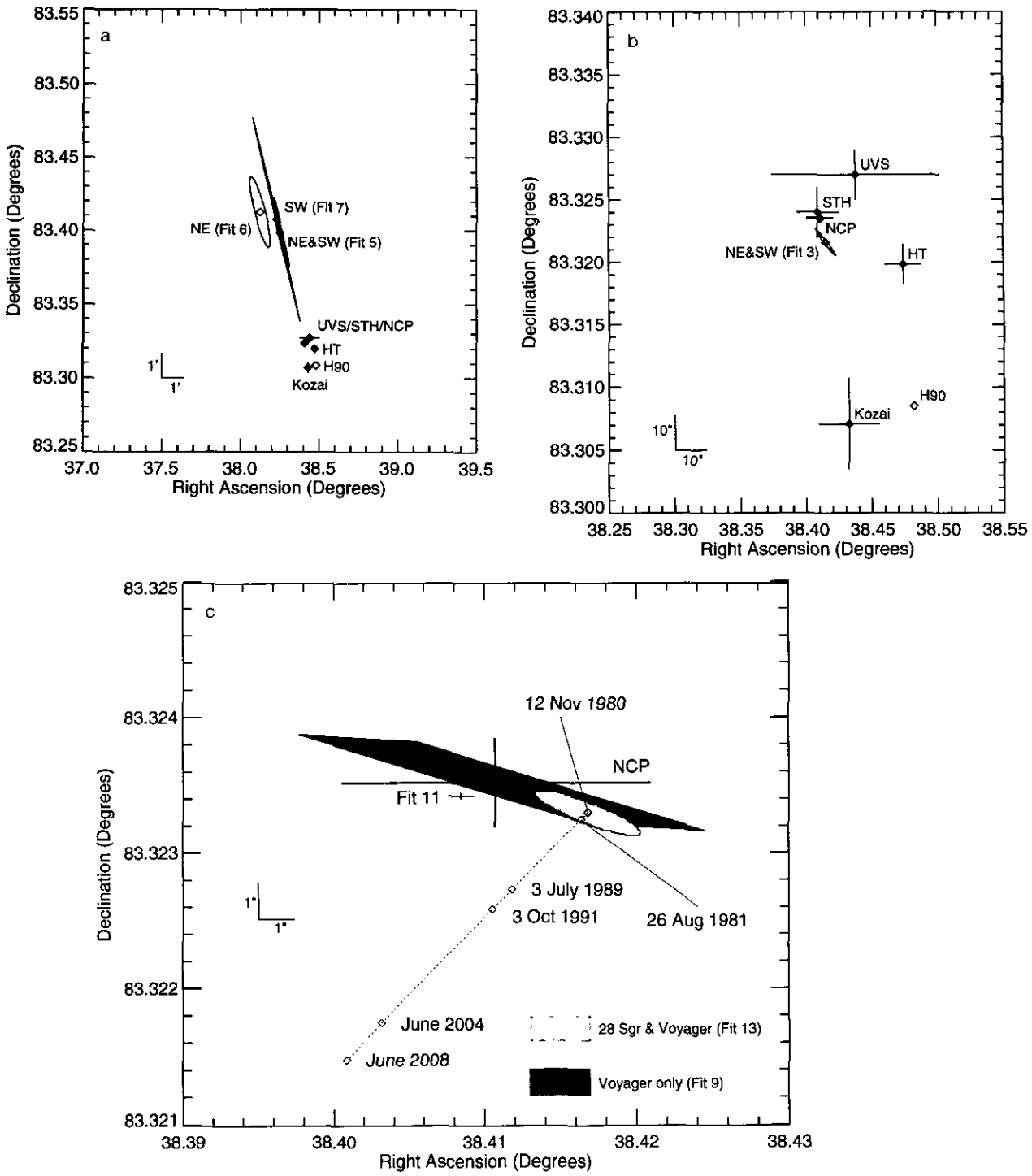


**FIG. 8.** Saturn's pole direction (B1950.0) from fits to occultation data. (a) Simultaneous fits for both the pole direction and the ring plane radius scale using 28 Sgr data described in this paper (NE, Fit 6), the data of H93 (SW, Fit 7), and with both datasets combined (NE&SW, Fit 5). All yield pole solutions which are systematically displaced from the poles determined by Kozai (1957) and Harper and Taylor (1993) (labeled HT) from satellite orbits and from analyses of Voyager UVS, RSS, and PPS ring occultations by STH and NCP, labeled UVS/STH/NCP. However, the pole is rather poorly constrained by the 28 Sgr data alone (as indicated by the error ellipses) and the correlation between the pole direction and ring radius scale is so high as to render these fits unsatisfactory. The light shaded region is shown in more detail in (b). (b) When the ring feature radii are instead held fixed at the mean values determined by the Voyager occultation data and the NCP pole (**Table II**), the fitted pole direction for the combined (NE&SW) 28 Sgr dataset (Fit 3) is well-defined and quite close to the STH/NCP pole. The Hubbard *et al.* (1990) earlier determination of the pole direction from 28 Sgr observations is also shown (H90). It differs substantially from the results shown here, due primarily to errors in event times and assumed ring geometry that have been corrected by H93. The light shaded region is shown in more detail in (c). (c) When Voyager and 28

Ring. However, because a slight shift in the pole direction could produce significant changes in the inferred radii of the measured features for the 28 Sgr occultation geometry (see Fig. 1), it was conceivable that these systematic trends in residuals could be reduced by changing either the pole direction or the model radii from the NCP values.

As a test, we next performed Fit 3 (pole fitted, NCP radii held fixed) and Fit 4 (NCP pole held fixed, radii fitted). As indicated in Table IX and Fig. 7, Fit 3 showed little improvement over Fit 2: the pole solution changed very little from the NCP results and the rms residuals were nearly the same. In contrast, Fit 4 was considerably better, with the rms radius residual reduced to 1.289 km, due primarily to a revision of the NCP radius scale by about −1 km in the inner C Ring and by as much as −4 km for selected Cassini Division features. To determine whether the fit could be further improved by allowing both the radii and the pole to be varied from the NCP values, we ran Fit 5, using the full set of 28 Sgr observations. However, the fitted radii shifted from the NCP values by −60 km in the inner C Ring to −85 km in the outer A Ring, and the pole direction shifted by nearly 0.1°. Both shifts greatly exceed any plausible uncertainties in these quantities based on numerous Voyager observations. In particular, the close match between model density wave profiles and occultation observations using the NCP radius scale rules out such large radius scale errors, and Saturn satellite tracking from Voyager 1 and 2 optical navigation (described by STH) similarly constrains the pole to be within ~0.015° of the NCP pole.

Figure 8a and Table VIII present the pole direction and formal errors for Fit 5 (labeled "NE & SW"), compared with several other pole determinations: the UVS, STH and NCP solutions, and Kozai's (1957) calculation based on Earth-based satellite observations. Although the formal error ellipse for Fit 5 is quite large, and the correlation coefficient between the pole direction coordinates $\alpha_P$ and $\delta_P$ is −0.9968, the fitted pole lies disconcertingly far—about two standard deviations—from the STH and NCP Voyager-based determinations.

In an attempt to isolate the cause for this large difference, we fitted the NE and SW data sets separately (Fits 6 and 7, respectively). If errant measurements from a single station were responsible, then the offending set could be identified by comparing the pole solutions from these two fits with the NCP result. In Fit 7 to the SW data, we adopted the H93 ring event times and did *not* fit for offset times for the SW stations. (When station offset times were added as free parameters for the MMT, CAT, KPi, KPe, and SPM stations, the formal error in the declination of the pole was nearly 0.2°.) Figure 8a shows the results of these fits (labeled "NE" and "SW", respectively). Both fits give roughly comparable offsets from the NCP pole. We conclude that systematic errors in a *single* data set, such as an uncorrected timing error, or inaccurate station coordinates, cannot account for the difference between the pole solution from the 28 Sgr data alone and the NCP pole solution from the Voyager observations. Perhaps the offset is due to slight noncircularity in some of the measured features in the A Ring. This is an issue worth revisiting when more occultation observations of the rings become available or when the orbits of other noncircular ring features are determined.

Whatever the cause, the error bars are so large and the radius scale is so obviously in error for this set of fits that perhaps the most important conclusion is that the 28 Sgr observations *by themselves* cannot be used to improve upon the NCP determination of *both* the pole direction and radius scale. There is a suggestion from Fit 4 that the NCP radii may be too large by a few kilometers, assuming the NCP pole is correct. Without additional constraints, radii and pole are simply too strongly correlated to say more. Geometrically, this is primarily due to the small size of the Earth compared to the rings (Fig. 1)—even for occultation chords separated by nearly the diameter of the Earth, only a small range of ring longitudes is sampled on either ingress or egress.

### 5.2. *Fits to Voyager 1 and 2 Observations*

In contrast to the results using 28 Sgr observations alone, described above, STH and NCP obtained quite

Sgr data are included in the solution, both the pole and radius scale are well constrained. The large error bars show the solution of NCP, based on Voyager 1 RSS and Voyager 2 PPS observations only. As these authors describe, the errors are principally due to uncertainties in the Voyager 1 and 2 trajectories. The actual pole uncertainty is more accurately shown by the dark shaded parallelogram (Fit 9), obtained by applying a priori along-track timing offsets of ±0.10 and ±0.17 sec to the Voyager 1 and 2 trajectories, respectively, and then fitting the pole and ring radius scale to the remeasured Voyager data in **Table II**. With 28 Sgr and Voyager observations included in the fit, but without taking into account the Voyager trajectory uncertainties, the solution (Fit 11) has extremely small *formal* errors, as shown by the small error bars to the lower left of the shaded regions. When along-track Voyager timing offsets are included as free parameters in the fit, and the precession of Saturn's pole is taken into account, the formal errors increase and the pole solution is shown by the light shaded elliptical region (Fit 13). We adopt this as our final solution for the Saturn pole direction, tabulated in **Table X**. The dashed line illustrates the calculated precession of Saturn's pole, relative to the adopted pole, from the time of the Voyager 1 encounter (12 Nov 1980). The labeled points correspond to times of the Voyager 2 encounter (26 Aug 1981), the 28 Sgr occultation (3 July 1989), the occultation of GSC6323-01396 (3 Oct 1991) (Cooke *et al.* 1992, Bosh *et al.* 1992), and the projected interval of the Cassini orbital tour from Saturn Orbital Insertion (June 2004) to the End of Mission (June 2008).

stringent constraints on Saturn's pole direction as a result of the very different occultation geometry of the Voyager 1 RSS occultation, when the rings were inclined only 5.9° to the line of sight, and the Voyager 2 δ Sco occultation, with a ring opening angle of 28.7°. With the ultimate objective of including both the 28 Sgr and the Voyager data in a joint solution for the pole and radius scale, we first tested our implementation of the barycentric vector algorithm described in Appendix A by attempting to reproduce the NCP pole and radius scale, using their input data for 26 features. The results (Fit 8) matched the NCP results very closely, to within 0.04″ in the pole position. An independent fit (Fit 9) to the remeasured Voyager data alone (see Table II) using the barycentric vector code developed for this work yielded a Saturn pole vector within 0.23″ of the NCP pole, ring feature radii which differ by about 0.1–0.3 km from NCP values, and an rms radius residual of 0.69 km. (This fit employed our new set of 30 presumed circular features.) The distribution of radius residuals is shown separately for the RSS and PPS observations in Fig. 9.

As described in detail by NCP, the main sources of error in their derived pole and radius scale are uncertainties in the trajectories of Voyager 1 and 2. Their adopted solution for the pole direction includes errors bars based on propagation of estimated systematic along-track trajectory errors. That is, the *paths* of the two spacecraft were assumed to be exactly as given by the Voyager navigation files, but the *locations* along the track were assumed to be uncertain by about 0.10 sec for Voyager 1 and 0.17 sec for Voyager 2. We followed NCP's error propagation procedure and performed four separate fits, identical to Fit 9 except with the (Voyager 1, Voyager 2) trajectory time offsets fixed at (±0.10, ±0.17) sec. The dark shaded parallelogram in Fig. 8c delimits the range of variation in the derived pole based on these four fits (compare to Fig. 3 of NCP).

In principle, an astrometric fit to the Voyager ring measurements might be used to constrain these trajectory uncertainties more tightly than was done by the navigation results. To test this possibility, we fitted the Voyager data sets alone (Fit 10), including as free parameters an along-track timing offset for each spacecraft, the pole direction, and individual feature radii. The fit yielded large formal errors in all fitted parameters, ring feature radii that differed by an implausible 50 km from the NCP results, and alongtrack timing offsets of −3.1 sec for Voyager 1 and −4.4 sec for Voyager 2, much larger than the estimated uncertainty in the trajectory of either spacecraft. In short, these results show that the a priori error propagation of NCP cannot be improved upon by relying on the Voyager occultation observations alone to refine the trajectory error estimates of the Voyager navigation team.

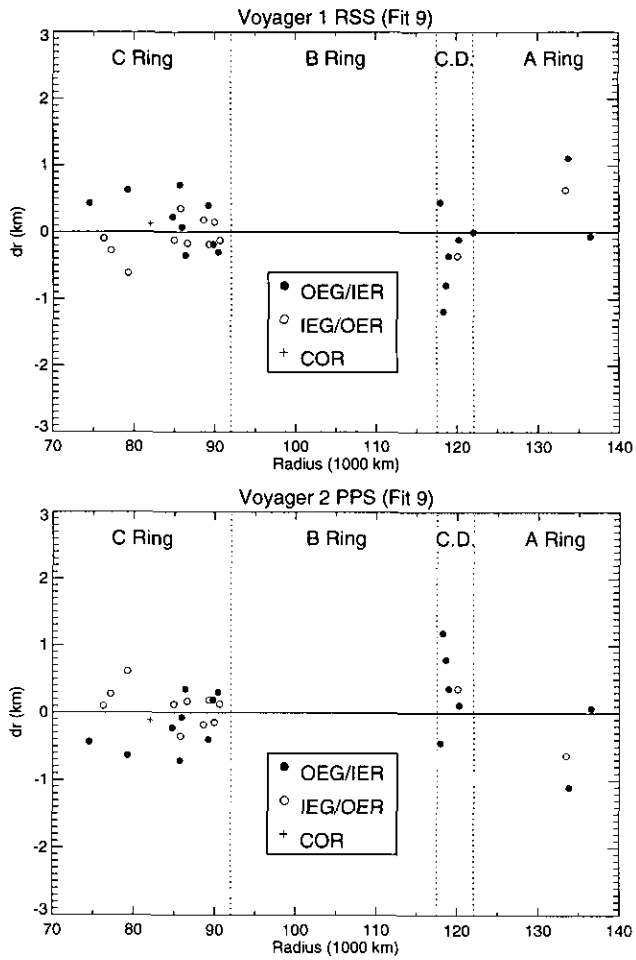


**FIG. 9.** Distribution of radius residuals for Voyager 1 RSS and Voyager 2 PPS observations from a solution in which the Voyager data alone were fitted (see **Table IX**, Fit 9). This fit effectively updates the NCP fit, using our new measurements in **Table II**. The small rms residual per degree of freedom of 0.69 km is partly an artifact of there being only two data points for each ring feature in this fit, which effectively reduces the standard deviation by $\sqrt{2}$ and also produces an antisymmetric pattern of residuals. Note that the largest individual residuals occur in the Cassini Division, for features 13 and 16, and for the edges of the Encke Gap in the A Ring (features 3 and 4). The latter are known to suffer perturbations of amplitude ~2 km due to the embedded moonlet, Pan, and similar perturbations may affect the Cassini Division gaps.

### *5.3. Joint Fits to 28 Sgr and Voyager 1 and 2 Observations*

The astrometric fits to the 28 Sgr data described above showed that rms residuals in ring plane radius as small as ~1.3 km (cf. Table IX, Fits 4 and 5) could be obtained, reflecting the high quality of the observations and the accuracy of the measurements. However, the pole direction and radius scale are poorly constrained by the Earth-based observations alone. In contrast, the two Voyager occultations yield uncertainties in the pole and ring radii

that are much smaller, but which are dominated by possible systematic errors in the assumed Voyager trajectories. In this section, we describe a series of joint fits to both the 28 Sgr and Voyager data, from which an improved solution is obtained. In addition, we attempt to obtain the first experimental constraint on the precession rate of Saturn's pole.

We began by fitting for the pole and radius scale, using both 28 Sgr and Voyager measurements of the 30 "circular" features identified in Table II. As indicated in Table IX, the free parameters of the fit included the 30 individual ring radii, the pole direction, and offset times for selected SW stations, as well as the usual sky plane offset between the actual and predicted location of Saturn at the time of the occultation. The rms error of this fit (Fit 11) was 1.309 km and the pole direction was within 1.02″ of the NCP value, with very small formal errors, as shown in Fig. 8c. The derived feature radii were, on average, ~1 km less than the corresponding NCP radii, corroborating the previous result (Fit 4) obtained by holding the pole fixed at the NCP location. Indeed, it appears that in the combined solution the principal leverage on the pole still comes from the Voyager data, whereas the more numerous 28 Sgr data force a modest (typically 1–2 km) reduction in the ring radii relative to the NCP solution. This close agreement with the NCP result argues against there being any gross inconsistency between the Voyager and 28 Sgr results, in contrast to the early findings by Hubbard *et al.* (1990).

However, the difference between the Fit 11 and Fit 9 (≃ NCP) poles, although small, is considerably larger than the formal uncertainties of either solution, if we neglect possible errors in the spacecraft trajectories: $-0.0027 \pm 0.0012°$ in right ascension and $-0.00015 \pm 0.00005°$ in declination, or 1.26″ overall. After initially dismissing this apparently tiny discrepancy, we were led by a reviewer's query to reinvestigate the possibility that it might be due to a real displacement of the pole between 1980/1981 and 1989. From Eq. (14), the predicted motion amounts to ~0.339″ year$^{-1}$, or 2.93″ in the 8.64 years between the Voyager 1 Saturn encounter in November 1980 and the 28 Sgr occultation in July 1989. This is seven times the formal uncertainty in our combined solution, Fit 11. Note further that the displacement of the Fit 11 pole to the south-west of the NCP pole is approximately in the direction of the predicted motion, although only ~1/3 of the amplitude. This is consistent with what might be expected for a compromise solution which is dominated by the Voyager data. (By contrast, the precession during the 286 days separating the encounters of Voyagers 1 and 2 is only 0.27″, much less than the adopted uncertainty in the NCP solution.) We were thus led to conclude that although a fixed pole may be adequate to model the Voyager observations alone, it is necessary to account for precession in combining Voyager and 28 Sgr (or subsequent) occultation data.

Furthermore, Fit 11 did not take into account known uncertainties in the Voyager trajectories. Although Fit 10 to the Voyager observations alone did not improve upon the a priori trajectory errors, the addition of 28 Sgr observations helped significantly by breaking the strong correlation between trajectory shifts and changes in the radius scale. With only egress observations, both RSS and PPS data are quite sensitive to trajectory errors, whereas with both ingress and egress measurements of each feature the 28 Sgr data rather tightly constrain the absolute ring radii, given a well-determined pole direction. In part to provide a comparison case to assess the importance of including precession in our final solution, we initially included along-track trajectory offsets for Voyager 1 and 2 as additional free parameters while ignoring the precession of Saturn's pole. The resulting solution (Fit 12) lies only 0.26″ from the NCP pole, but the formal errors are ~1/3 of those derived by NCP from the a priori trajectory uncertainties. (This solution is also used in Appendix B as the basis of sample calculations, and to assess the influence of various systematic effects on our calculated radii.)

Clearly, then, it is desirable that both pole precession *and* trajectory errors be taken into account in any realistic joint fit to the 28 Sgr and Voyager data. We attempted a simultaneous solution for both the pole precession rate and the spacecraft trajectory offsets, but the present data set does not span a sufficiently long period of time to permit a meaningful solution of this type. By systematically varying the assumed precession rate while solving for the pole, radius scale, and trajectory offsets, the best that we could obtain was a global $\chi^2$ minimum for a rather poorly constrained precession rate equal to $0.5 \pm 1.1$ times the predicted rate, and RSS/PPS trajectory offsets of $+0.03$ and $-0.11$ sec, respectively. The somewhat surprising result that any reasonable simultaneous solution is possible at all seems to be due to the fact that the locus of precession is almost orthogonal to the major axis of the error ellipse due to trajectory uncertainties (see Fig. 8c).

We were thus led to try two simpler approaches in dealing with the combined pole precession/trajectory problem. In our final solution incorporating along-track spacecraft trajectory offsets (Fit 13), we fixed the precession rate at the value given by Eq. (14) and solved for the pole position at the epoch of Voyager 1 encounter—23:46:32 UTC, 12 November 1980 = JD 2444556.49065. The new pole lies 2.55″ from the NCP pole, although the error ellipse falls within the error parallelogram based on fits to Voyager data alone (Fig. 8c). The fitted trajectory offsets of $+0.051 \pm 0.036$ sec for Voyager 1 and $-0.094 \pm 0.061$ sec for Voyager 2 are within the a priori uncertainties of $\pm 0.10$ and $\pm 0.17$ sec, respectively, but

are more precisely determined by about a factor of three. This reduction in the spacecraft trajectory uncertainties leads to a similar reduction in the uncertainty of the absolute ring radii, from the ±2 km of NCP to ~±0.6 km for Fit 13.

In a second set of solutions we systematically varied the precession rate and repeated Fit 11 for the pole and radius scale, while keeping the nominal Voyager trajectories fixed. Our objective here was to determine to what extent the combined data set could actually constrain the pole precession rate, given the direction in which the pole is expected to move,[1] and in the absence of trajectory errors. The results of this series of fits are shown in Fig. 10. In the top panel, the sum of squared residuals of the fits is plotted as a function of the assumed precession rate, in units of the predicted value. The best fit is obtained for a precession rate of 0.86 ± 0.31 times the expected value, justifying our inclusion of this effect in the combined solution and nicely confirming our predicted rate. The corresponding pole position at epoch is essentially coincident with the Voyager-only result, Fit 9, or equivalently with the NCP pole. The mean radius shift of our 30 circular features relative to the NCP radii, shown in the bottom panel of Fig. 10, is −150 m for the minimum-$\chi^2$ solution and a negligible −70 m for the predicted precession rate.

*5.3.1. The adopted fit.* Armed with this apparent confirmation of the predicted pole precession rate, we adopt Fit 13 as our preferred solution for the pole direction, ring feature radii, trajectory and station timing offsets, and the constant offset to the sky-plane position of Saturn relative to 28 Sgr. The detailed results of the adopted fit are presented in Table X, where the formal errors take into account the internally determined along-track Voyager trajectory uncertainties but exclude any uncertainty in the pole precession rate. The fitted ring radii are compared with the Voyager-derived results in Fig. 11. The mean shift in the radius scale, in the sense (Fit 13–NCP), is −0.7 ± 0.2 km, with an overall rms fit residual of 1.295 km. Using the Fit 13 pole, we separately fitted the B Ring observations for 28 Sgr to determine mean B Ring feature radii (Fit 14). The rms error of this fit (Fig. 7 and Table IX) was rather large (2.675 km), due principally to the difficulty of measuring the precise locations of these features. The resulting B Ring radii, with typical uncertainties of 1.2 km, are also included in Table X.

In addition to the ring pole and radii, skyplane offsets, and spacecraft trajectory offsets, Fit 13 includes systematic time offsets for ESO and for four of the SW stations, for the reasons discussed in Section 2.1. above. These station offsets range from −0.024 sec for SPM to 0.068 sec for MM1, and ~−0.21 sec for ESO. They are determined to an accuracy of ±0.02 sec or better, corresponding to ~0.4 km of displacement of the ring features in the skyplane. Because of the relative proximity of the SW station tracks to those of Palomar and McDonald, for which no offsets are allowed in the fit, these fitted offsets are not sensitive to the exact orientation of the ring plane

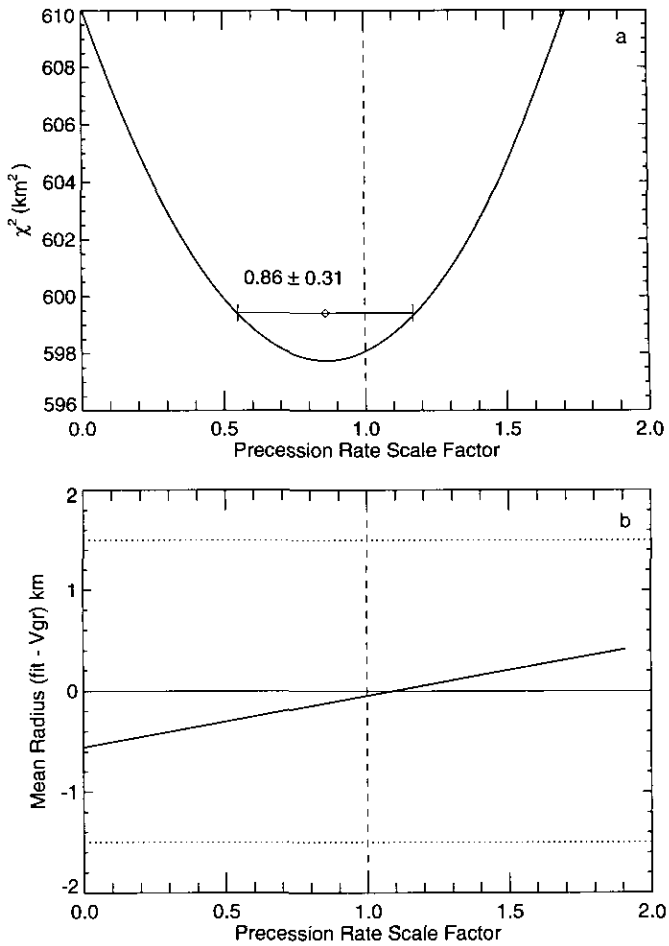


FIG. 10. Precession of Saturn's pole. (a) Sum of squared radius residuals as a function of the assumed precession rate of Saturn's pole. A series of fits to the standard set of 28 Sgr and Voyager occultation data was performed, identical to Fit 11 (see **Table IX**) except that Saturn's pole was assumed to precess at a nominal rate of ($d\alpha_P/dt$ = −0.00057699°year$^{-1}$, $d\delta_P/dt$ = −0.00006604°year$^{-1}$, B1950.0; denoted by the dashed vertical line) times a precession rate scale factor. No Voyager trajectory corrections were included in the fits. The best fit results give a precession rate of 0.86 ± 0.31 times the nominal rate, where the uncertainty is determined from the $\chi^2$ per degree of freedom. (b) The effect of Saturn's pole precession on the fitted ring radii, for the same series of fits as described in (a). The mean radius shift (for 30 ring features) between the fitted results and the Voyager radii given in **Table II** is shown as a function of the precession rate scale factor. At the nominal rate (denoted by the dashed vertical line) the mean radius shift is only 70 m. The dotted horizontal lines at ±1.5 km correspond to the uncertainty in the ring radius scale inferred from comparison of Voyager occultation profiles and models of density waves (see NCP).

[1] Note that, for practical purposes over such a short period of time, it is immaterial whether the pole is assumed to precess about Saturn's current orbit normal rather than the invariable pole of the Solar System.

TABLE X
Adopted Astrometric Solution

**Saturn Pole Direction**[a]

| | |
|---|---|
| $\alpha_P$(B1950.0) | 38.4168 ± 0.0035 |
| $\delta_P$(B1950.0) | 83.32329 ± 0.00017 |
| $\alpha_P$(J2000.0) | 40.5955 ± 0.0036 |
| $\delta_P$(J2000.0) | 83.53812 ± 0.00018 |
| $\rho(\alpha_P, \delta_P)$[b] | −0.8715 |

**Skyplane Offsets (Planet − Star)**[c]

| | |
|---|---|
| $f_0$(B1950.0) (km) | 989.93 ± 0.48 |
| $g_0$(B1950.0) (km) | −828.00 ± 0.52 |

**Station Time Offsets (s)**[d]

| | |
|---|---|
| ESO1 | −0.219 ± 0.014 |
| ESO2 | −0.204 ± 0.015 |
| MM1 | 0.068 ± 0.017 |
| CAT | 0.030 ± 0.016 |
| SPM | −0.024 ± 0.011 |
| KPi | 0.064 ± 0.017 |
| KPe | 0.059 ± 0.021 |
| RSS | 0.054 ± 0.036 |
| PPS | −0.093 ± 0.060 |

| Feature | Radius (km) | dr[e] | N[f] | rms[g] | Feature | Radius (km) | dr[e] | N[f] | rms[g] |
|---|---|---|---|---|---|---|---|---|---|
| 44 | 74490.76 ± 0.57 | 0.76 | 8 | 1.37 | 23 | 90614.87 ± 0.50 | −0.03 | 18 | 1.25 |
| 40 | 76263.93 ± 0.56 | 1.03 | 9 | 1.57 | 83[h] | 94439.46 ± 1.20 | −4.64 | 5 | 1.38 |
| 39 | 77164.63 ± 0.56 | 0.23 | 9 | 0.84 | 82[h] | 95365.20 ± 1.20 | 6.90 | 5 | 2.92 |
| 38 | 79220.31 ± 0.55 | −0.69 | 11 | 0.91 | 81[h] | 96895.97 ± 1.09 | −3.63 | 6 | 3.06 |
| 37 | 79265.28 ± 0.57 | 0.18 | 10 | 1.69 | 78[h] | 98278.49 ± 1.20 | −8.71 | 5 | 1.78 |
| 36 | 82040.58 ± 0.59 | −1.02 | 8 | 0.90 | 76[h] | 101002.53 ± 1.20 | −7.17 | 5 | 1.83 |
| 35 | 84749.44 ± 0.49 | −0.86 | 18 | 1.41 | 75[h] | 101543.48 ± 1.20 | −5.82 | 5 | 2.28 |
| 34 | 84949.38 ± 0.50 | 0.18 | 17 | 1.61 | 72[h] | 103657.03 ± 1.09 | −16.2 | 6 | 2.00 |
| 33 | 85660.65 ± 0.60 | −0.85 | 8 | 0.71 | 71[h] | 104087.19 ± 1.20 | 3.79 | 5 | 3.24 |
| 42 | 85758.59 ± 0.51 | −0.11 | 15 | 1.14 | 20 | 117932.25 ± 0.62 | 0.05 | 9 | 1.03 |
| 31 | 85921.38 ± 0.60 | −2.22 | 8 | 1.72 | 16 | 118283.29 ± 0.64 | −0.61 | 8 | 1.09 |
| 30 | 86370.61 ± 0.52 | −1.29 | 14 | 0.88 | 13 | 118628.11 ± 0.55 | −0.99 | 17 | 1.35 |
| 29 | 86601.11 ± 0.50 | −1.29 | 18 | 1.06 | 15 | 118965.69 ± 0.56 | −2.61 | 15 | 1.60 |
| 28 | 88594.29 ± 0.52 | −0.01 | 14 | 1.02 | 12 | 120073.42 ± 0.63 | −2.88 | 9 | 1.65 |
| 27 | 89188.60 ± 0.51 | −1.80 | 16 | 0.80 | 11 | 120246.31 ± 0.63 | 1.31 | 9 | 1.57 |
| 41 | 89295.06 ± 0.51 | −0.24 | 17 | 1.09 | 7 | 122049.48 ± 0.61 | −3.02 | 12 | 1.29 |
| 26 | 89786.80 ± 0.50 | −1.50 | 17 | 0.79 | 4 | 133423.53 ± 0.58 | 0.03 | 17 | 1.28 |
| 25 | 89939.28 ± 0.50 | 0.48 | 19 | 0.94 | 3 | 133745.14 ± 0.59 | −0.06 | 16 | 1.17 |
| 24 | 90404.08 ± 0.52 | −1.62 | 14 | 1.54 | 1 | 136522.28 ± 0.59 | 0.28 | 17 | 0.68 |

[a] Pole direction at a reference time of 1980 November 12 23:46:32 UTC, assuming a constant precession rate of $d\alpha_P/dt = -0.00057699°\text{yr}^{-1}$, $d\delta_P/dt = -0.00006604°\text{yr}^{-1}$ (B1950.0).
[b] Correlation coefficient for B1950.0 $\alpha_P, \delta_P$.
[c] See Eq. A52, Appendix A.
[d] Offset times to be *added* to nominal measured feature times for each station.
[e] Difference (km) between fitted radius and nominal Voyager radius from Table II.
[f] Number of data points for this feature included in fit.
[g] rms residual (km) for data points for this feature.
[h] B Ring results from Fit 14, Table IX; all others from Fit 13.

or to the absolute ring radii: Fit 2, which assumed both the NCP pole and ring radii, yielded station offsets within $1\sigma$ of the final values in Table X. Nevertheless, the derived offsets imply that the timing calibration for these stations established by H93, on the basis of cross-correlation of atmospheric light curve spikes, is in error in some cases by more than their estimated ±0.02 sec. We believe that sharp ring edges provide an intrinsically more reliable fiducial reference for such calibrations than do the inhomogeneities in Saturn's atmosphere responsible for the spikes in the atmospheric light curves.

*5.3.2. Fit residuals.* Inspection of Fig. 11 reveals a systematic difference between the radial shifts for OEG/IER features (those for which $d\tau/dr > 0$) and those for IEG/OER features (for which $d\tau/dr < 0$) in the C Ring. This pattern is also evident in the Voyager 1 RSS and Voyager 2 PPS radius residuals from Fit 13 shown in Fig. 12, in contrast to the Voyager-only fit results in Fig. 9. The greater inward shift of model radii for OEG/IERs results in positive residuals in the RSS and PPS data and vice versa for the IEG/OERs. These systematic differences are most probably due to the combined effects of the lower resolution of the 28 Sgr data and the gradual "ramp-like" nature of many of these C Ring features. However, since the numbers of inner and outer gap edge (IEG/OEG) C Ring features are comparable, there is no reason to suspect that these systematic patterns in the residuals for the Voyager observations result in a significant systematic error in the derived radius scale itself.

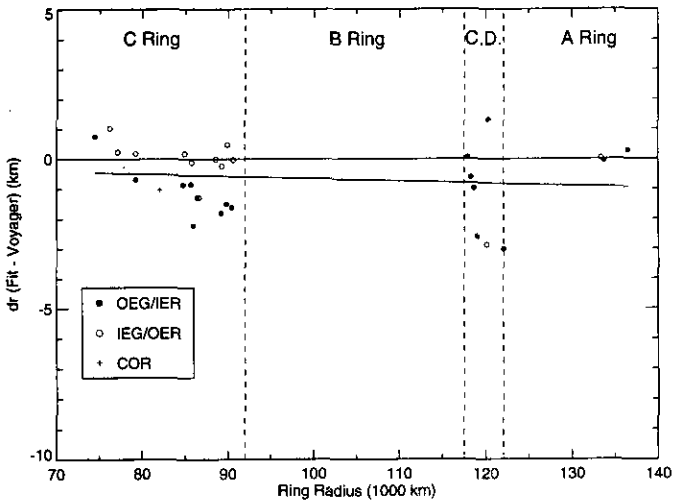


FIG. 11. Differences between the ring feature radii from our adopted combined fit to 28 Sgr and Voyager data, *Fit 13* (see **Fig. 8c** and **Table X**) and the a priori standard Voyager radii are shown as a function of ring plane radius. The standard radii (see **Table II**) were obtained from Fit 1 to the Voyager data, using the NCP pole. Features are grouped by their three-letter codes, as given in **Table II**. In the new solution, ring radii are systematically smaller by an average of ~0.7 km in the C Ring. A more scattered pattern of shifts is found for features in the Cassini Division, labeled C.D. The systematic shift is within the quoted uncertainty of the NCP solution. In the C Ring, the plateau inner edges (IER) are shifted inward by ~1.5 km relative to the corresponding outer edges (OER) (note that no actual gap edges were fitted in the C Ring). This may be attributable to the relatively gradual edges of this class of feature, combined with the lower resolution of the 28 Sgr data; no such consistent pattern is seen in the Cassini Division or A Ring, where most of the quasi-circular features (all but feature 7) are sharp gap edges.

The overall distribution of radius residuals for the full set of 28 Sgr features used in the adopted solution is shown in Fig. 13 (top panel), along with the rms radius residual for each feature of the combined set of 28 Sgr and Voyager data (bottom panel). (Note that the B Ring residuals were obtained separately from Fit 14, since B Ring features were excluded from the adopted fit for the pole and radius scale.) The rms error for Fit 13 is shown as a horizontal dashed line in the lower panel. The bulk of the individual observations have residuals of less than 2 km, although there are some outliers, particularly in the C Ring. We have examined the individual measurements in the NE data and see no indication of obvious measurement errors. Histograms of timing residuals for each station are shown in Fig. 14, and individual radius residuals are plotted against ring radius for each station in Fig. 15, where ingress features are marked by "+" and egress features are marked by open circles. At the kilometer level, there appear to be some systematic patterns in the residuals. For example, the bulk of the PAL radius residuals are negative, whereas the IRTF residuals are mainly positive. These differences may be due in large part to possible "jitter" in the absolute timing of the PAL data at the 0.05-sec level, as described above in Section 2.1. In addition, there appear to be small systematic timing residuals in the MCD data (−0.03 sec) and IRTF data (+0.05 sec) relative to PAL, CTIO, and UKIRT. These were confirmed by an earlier trial fit in which offsets were included for *all* stations except Palomar and which yielded station corrections of +0.024, −0.054, −0.024,

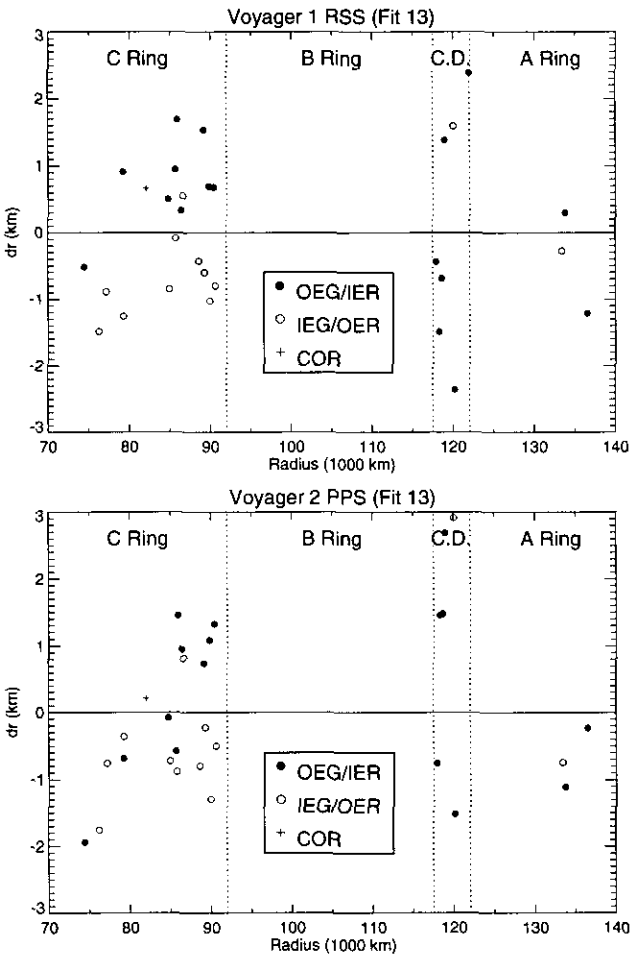


FIG. 12. Distribution of radius residuals for 59 Voyager 1 RSS and Voyager 2 PPS observations, relative to our adopted solution (Fit 13) as given in **Table X**. Note that Voyager B Ring observations were not included in the fit, as their mean radii differed substantially from those determined from the 28 Sgr observations. Features in the Cassini Division (C.D.) again show the greatest scatter. There is no overall systematic trend in the radius residuals, due in part to the inclusion of along-track Voyager 1 and 2 trajectory offsets as fitted parameters. However, there are clear systematic differences in the C Ring between plateau inner (IER) and outer (OER) edges, attributable to the systematic shifts in the fitted radii of these features noted in the caption to **Fig. 11**. The systematic inward (outward) shift in the fitted radii for IER's (OER's) relative to the Voyager solution results in positive (negative) radius residuals for both RSS and PPS measurements of these features. No such systematic effects are visible in the Cassini Division or A Ring.

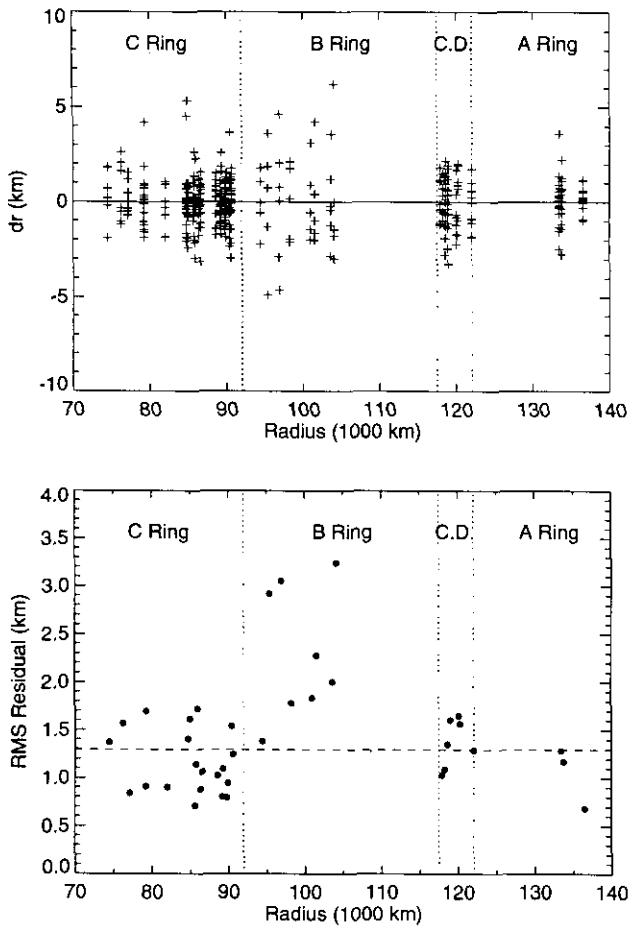


FIG. 13. Top: Distribution of radius residuals vs ring plane radius for the combined set of 380 individual 28 Sgr observations, relative to our adopted solution, Fit 13. Note that the B Ring features were not included in the fit for the pole and radius scale given in **Table X**. Instead, the mean radii of these eight features in the 28 Sgr data were fitted separately (Fit 14), using the pole and Saturn ephemeris offset from the adopted solution. In this way, the larger scatter of the points in the B Ring (due largely to measurement uncertainties for these high optical depth features) did not bias the fit for the pole. See text for further details. (Bottom) RMS radius residuals for each ring feature vs ring plane radius, for Fits 13 and 14 (see **Table X**). Both 28 Sgr and Voyager observations are included for C Ring, Cassini Division, and A Ring features. In the B Ring, Voyager data were excluded because of relatively large differences between the 28 Sgr and PPS radii found for several of these features.

and −0.036 sec for MCD, IRTF, UKIRT and CTIO, respectively.

As a final comparison of the residuals, Fig. 16 shows the station-by-station rms residuals in radius and event time. Most stations have rms radius residuals of less than 1.5 km, and there are no obvious outliers among the stations. Note that all the fitted features were weighted equally—no attempt was made to determine relative weights for individual data points or stations.

### *5.4. Sensitivity to Systematic Errors*

The reliability of our adopted solution for the pole direction and radius scale (Table X) is dependent not only on the proper implementation of an accurate astrometric reduction method, but also upon the magnitude of unmodelled systematic errors. In this section, we identify a number of possible systematic errors and estimate their effects on our astrometric solution.

*5.4.1. Cross-track Voyager trajectory errors.* Slight modifications in the assumed Voyager trajectories can have a significant effect on the pole direction and radius scale derived from Voyager radio and stellar occultations. Our adopted solution accounts for possible along-track errors, but it is likely that the actual paths of the two spacecraft differ to some extent from those we have used for our model fits. To estimate the effects of such differences, we have applied fixed offsets to the trajectories and refitted for the pole and radius scale. The trajectory offsets were modeled in the following manner. In addition to the along-track position error, which is approximated as a fixed offset time $\sigma(t)$ for each spacecraft (as described previously), a radial offset $\sigma(r)$ in the spacecraft orbital plane and a "vertical" offset $\sigma(z)$ normal to this plane were specified. These three offsets, $\sigma(t)$, $\sigma(r)$, $\sigma(z)$, are roughly orthogonal, and were easily incorporated into the orbit fitting code.

As discussed by NCP, the estimated trajectory errors for Voyager 1 and 2 are described in terms of B-plane statistics, with $x$ = North on the sky (B1950.0), $y$ = East on the sky, and $z$ = radial (from Earth, not Saturn). For Voyager 1, the B-plane statistics at Saturn egress (near the start of the ring occultation) are $\sigma(x)$ = 1.0 km, $\sigma(y)$ = 0.3 km, and $\sigma(z)$ = 0.6 km. At closest approach, the errors are $\sigma(x)$ = 0.5 km, $\sigma(y)$ = 0.85 km, and $\sigma(z)$ = 0.32 km. Using the larger error in each case, these map roughly into $[\sigma(t), \sigma(r), \sigma(z)]$ = [0.10 sec, 0.6 km, 0.85 km] for Voyager 1. For Voyager 2, B-plane statistics are available only at Saturn closest approach, about 2 hr after the ring occultation: $\sigma(x)$ = 1.4 km, $\sigma(y)$ = 1.5 km, and $\sigma(t)$ = 0.14 sec. Mapping these unchanged back to the occultation, these correspond roughly to $[\sigma(t), \sigma(r), \sigma(z)]$ = [0.14 sec, 1.5 km, 1.4 km] for Voyager 2.

Our adopted astrometric solution accounts explicitly for $\sigma(t)$. To determine the sensitivity of our results to errors in the other two coordinates, we performed a series of fits in which the offsets were set individually at $[0, \pm\sigma(r), \pm\sigma(z)]$ for Voyager 1 and 2 in turn, holding the other offsets at zero. Table XI includes the results of these eight fits (Fits 15–22) and lists the effect on the fitted pole and radius scale. In all cases, the pole directions obtained from this test series lie within the error bars of our adopted fit in Table X. Systematic shifts in the radius scale due to radial and vertical trajectory errors

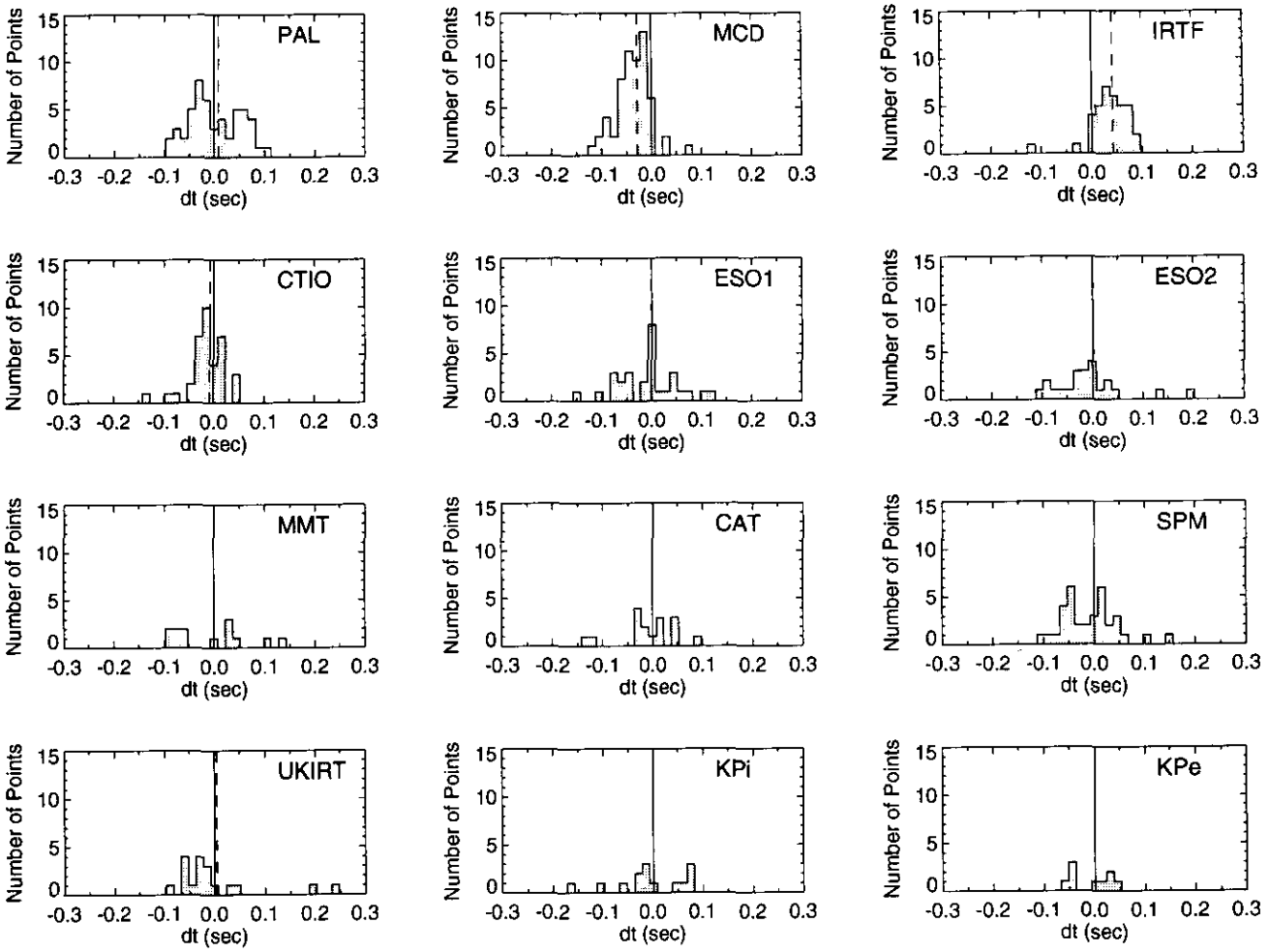


FIG. 14. Distribution of residuals (observed–model) in ring event time for each station from our adopted solution, Fit 13. The mean of the distribution for each station is indicated by a dashed vertical line and is in every case less than 0.05 sec.

$\sigma(r)$ and $\sigma(z)$ were <0.3 km throughout the ring region. We conclude that the quoted uncertainty of our adopted solution comfortably includes any systematic errors resulting from $\sigma(r)$ and $\sigma(z)$ trajectory offsets.

*5.4.2. Saturn satellite motion.* During the 28 Sgr occultation, Saturn orbited the system barycenter with a velocity of about 4.75 km/hr due to the orbital motion of Saturn's satellites (principally Titan). Projected into the sky plane, Saturn's velocity with respect to the adopted JPL DE-130 barycentric ephemeris was approximately 3.02 km/hr West and 1.96 km/hr North (B1950.0). Over the duration of the occultation (approximately $3\frac{1}{2}$ hr), failure to account for Saturn's motion with respect to the barycenter would result in an unacceptably large chord length error of about 10.6 km and an associated error in the derived pole position. We accounted for the influence of the satellites in our barycentric vector solution by explicitly including the time-dependent vector offset position of Saturn from the system barycenter, based on JPL satellite ephemerides for the eight major Saturnian satellites (Mimas, Enceladus, Tethys, Dione, Rhea, Titan, Hyperion, and Iapetus) obtained from the NAIF at JPL (*Acton 1990*).

As an independent check on these results, we interpolated the tabulated satellite positions for Titan, Rhea, Dione, Tethys, and Iapetus in the *Astronomical Almanac* (1989) over the duration of the 28 Sgr occultation and determined the corresponding sky-plane offset position and velocity of Saturn from the system barycenter as a function of time, using the values given in Table VII for the satellite masses. We then reran Fit 12 using these satellite ephemerides and the sky-plane astrometric algorithm, rather than the barycentric vector method. The results of this fit (Fit 23) are given in Table XI, where the differences from Fit 12 are at the 100-m level in ring plane radius. These differences are due almost entirely to the differences between the satellite ephemerides, and not to

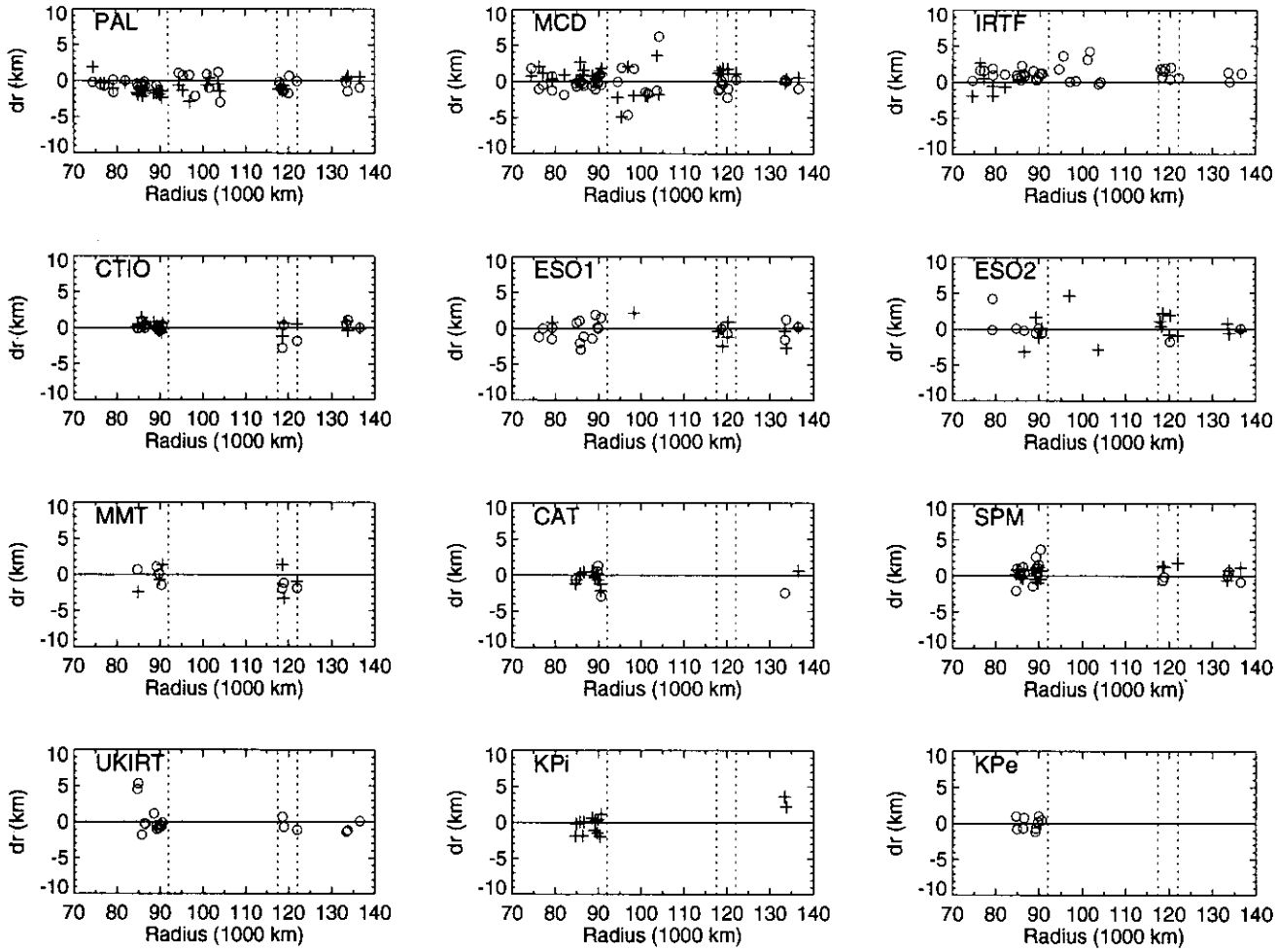


FIG. 15. Radius residuals of individual ring features for each station from the adopted solution, Fig. 13, as a function of ring plane radius. Ingress features are denoted by "+" signs, and egress observations by open circles. The vertical dashes delineate the C Ring, B Ring, Cassini Division, and A Ring.

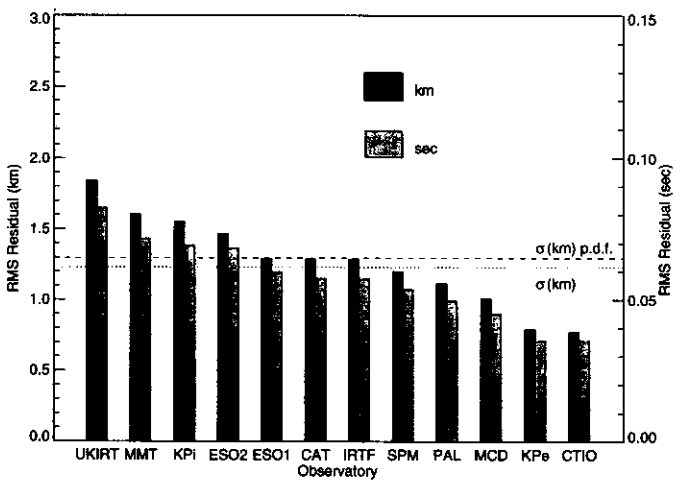


FIG. 16. RMS fit residuals by station, in both ring plane radius (km and ring event time (sec), from the adopted solution in **Table X**. The overall rms error for the fit, per degree of freedom, is shown by the dashed line. The dotted line indicates the weighted average of the the displayed distribution.

the differences between the sky-plane and barycentric vector methods, which are shown in Appendix B to agree at the 20-m level in ring plane radius.

To determine the relative importance of Titan and the other major satellites, we performed Fit 24, in which only Titan's influence on Saturn's motion was taken into account, using the apparent positions of Titan as tabulated in the *Astronomical Almanac*. The pole direction shifted negligibly from the five-satellite solution (see Table XI), although the derived ring radii shifted by a few hundred meters. To provide a more direct comparison with our adopted solution, we computed the motion of Saturn with respect to the system barycenter using the 3-D JPL satellite ephemeris for Titan, but ignoring the leverage provided by the seven other satellites included in Fit 12. In this fit (Fit 25), the derived ring radii decreased by a few hundred meters from our adopted fit. Finally, to quantify the effect of neglecting to correct for Saturn's motion with respect to the barycenter during the 28 Sgr occultation, we performed Fit 26, in which satellite motions

TABLE XI
Pole and Radius Sensitivity Tests

**Sensitivity to Voyager Trajectory Errors**

| | Voyager 1 | | Voyager 2 | | Saturn Pole (B1950.0)[a] | | $\Delta r$ (km)[b] | | |
|---|---|---|---|---|---|---|---|---|---|
| Fit | $\sigma(r)$[c] | $\sigma(z)$[d] | $\sigma(r)$[c] | $\sigma(z)$[d] | $\Delta\alpha_P(°)$ | $\Delta\delta_P(°)$ | #1 | #44 | $\sigma$(rms)[e] |
| 15 | +0.6 | 0 | 0 | 0 | +0.00000 | −0.00000 | +0.005 | +0.005 | 1.2949 |
| 16 | −0.6 | 0 | 0 | 0 | −0.00000 | +0.00000 | −0.005 | −0.005 | 1.2952 |
| 17 | 0 | +0.85 | 0 | 0 | +0.00074 | −0.00013 | +0.028 | +0.009 | 1.2961 |
| 18 | 0 | −0.85 | 0 | 0 | −0.00074 | +0.00013 | −0.028 | −0.009 | 1.2943 |
| 19 | 0 | 0 | +1.5 | 0 | −0.00187 | +0.00007 | +0.284 | +0.118 | 1.2994 |
| 20 | 0 | 0 | −1.5 | 0 | +0.00187 | −0.00007 | −0.284 | −0.118 | 1.2924 |
| 21 | 0 | 0 | 0 | +1.4 | −0.00129 | +0.00005 | +0.192 | +0.074 | 1.2988 |
| 22 | 0 | 0 | 0 | −1.4 | +0.00129 | −0.00005 | −0.192 | −0.074 | 1.2921 |

**Sensitivity to Saturn Satellite Motion**

| | | Saturn Pole (B1950.0)[a] | | $\Delta r$ (km)[b] | | |
|---|---|---|---|---|---|---|
| Fit | # Satellites | $\Delta\alpha_P(°)$ | $\Delta\delta_P(°)$ | #1 | #44 | $\sigma$(rms)[e] |
| 12[f] | 8[g] | 0 | 0 | 0 | 0 | 1.2950 |
| 23 | 5[h] | +0.00018 | −0.00000 | +0.125 | +0.068 | 1.2957 |
| 24 | 1[i] | +0.00010 | −0.00000 | −0.138 | −0.083 | 1.2952 |
| 25 | 1[j] | −0.00013 | +0.00000 | −0.228 | −0.131 | 1.2947 |
| 26 | 0 | +0.00617 | −0.00030 | −3.11 | −1.73 | 1.3206 |

**Sensitivity to Gravitational Bending**

| | | Saturn Pole (B1950.0)[a] | | $\Delta r$ (km)[b] | | |
|---|---|---|---|---|---|---|
| Fit | Gravitational Bending | $\Delta\alpha_P(°)$ | $\Delta\delta_P(°)$ | #1 | #44 | $\sigma$(rms)[e] |
| 12[f] | $J_2$ | 0 | 0 | 0 | 0 | 1.2950 |
| 27 | point mass | −0.00041 | +0.00006 | −0.079 | −0.444 | 1.2954 |
| 28 | none | −0.02973 | +0.00407 | −19.6 | −35.6 | 2.2277 |

[a] Difference from adopted fit in **Table X**.
[b] Difference from adopted fit for features #1 and #44 in **Table X**.
[c] Radial shift (km) from nominal Voyager trajectory.
[d] Vertical shift (km) from nominal Voyager trajectory.
[e] rms ring plane radius residual per degree of freedom (km) for orbit fit.
[f] No Saturn pole precession included in this fit.
[g] 3-D vector ephemerides for Titan, Rhea, Dione, Tethys, Iapetus, Enceladus, Mimas, and Hyperion from JPL/NAIF File SAT018H.BSP (Acton 1990).
[h] Sky-plane satellite ephemerides, based on *Astronomical Almanac* (1989) tabulated positions for Titan, Rhea, Dione, Tethys, and Iapetus.
[i] Same as Fit 23, but for Titan only.
[j] Same as Fit 12, but for Titan only.

were ignored. The pole direction changed from our adopted solution by about 3 arcsec, significantly greater than our adopted uncertainty, and the fitted ring radii decreased by several kilometers.

From these tests, we conclude that *Astronomical Almanac* satellite positions are adequate for astrometry at the few-hundred-meter level, but that for the most precise work, a more accurate 3-D vector ephemeris is preferable. It should be noted that the influence of individual satellite motions depends strongly on the relative sky plane orientations of the satellites and planet at the time of the occultation, and on the duration of the event. It is likely that Titan's orbital motion should be taken into account for any stellar occultation by Saturn's rings, but the importance of the other satellites must be determined on a case-by-case basis.

*5.4.3. General relativistic deflection by Saturn.* The gravitational deflection of starlight by Saturn results in a transverse displacement of the received ray by some tens of kilometers at the Earth, and thus it is important to include this general relativistic effect in the astrometric solution for the radius scale and pole direction. In previous ring occultation orbit models for the Uranian rings, the planet was modeled as a point mass, but Saturn is sufficiently oblate that a more accurate representation of the gravitational bending was required. In our adopted solution, we have included the $J_2$ term in the bending equation (see Eqs. (13) and (14) of H93). To measure the effect on the solution of ignoring Saturn's oblateness, we ran Fit 27, in which Saturn was modeled as a point mass. The results, given in Table XI, show that the pole direction changes by much less than the uncertainty in our adopted solution, but that the derived ring radii shift by nearly −0.5 km in the inner C Ring.

Failure to account for any general relativistic bending results in enormous systematic errors in both the pole direction and ring radii, as illustrated by Fit 28 in Table XI. From these tests, we conclude that it is essential to account for Saturn's oblateness when correcting for gravitational deflection of light, if one is to obtain subkilometer accuracy in the derived ring radii.

*5.4.4. Stellar proper motion and annual parallax.* For this analysis, we have assumed that the proper motion and the annual parallax of 28 Sgr could be neglected, over the duration of the occultation. As we have just seen, however, the astrometric solution for Saturn's pole and radius scale depends quite sensitively on the assumed velocity of Saturn with respect to the occulted star. This relative velocity is influenced not only by Saturn's satellites, but also by any changes in the apparent direction of the star during the event. These can be conveniently separated into stellar proper motion and annual parallax.

For a stellar proper motion of $\mu$ (in arcsec/cy), the associated sky-plane velocity of the star with respect to a fixed inertial direction is

$$v_\mu = 2.3 \times 10^{-7}\ \mu\Delta \text{ km/sec} \tag{15}$$

where $\Delta$ is the geocentric distance to the planet in AU. The error in the derived chord length for an occultation spanning a ring system of radius $R$ is of order

$$dl_\mu = 2Rv_\mu/v_{\text{sky}}, \tag{16}$$

where $v_{\text{sky}}$ is the mean relative velocity of the star and planet in the sky plane. For the 28 Sgr event, $v_{\text{sky}} \sim 20.5$ km/sec, and a proper motion of 30 arcsec/cy would result in a chord length error of 1 km. Since the estimated proper motion of 28 Sgr is only 0.2 arcsec/cy (Table VII), proper motion may be safely neglected in this case.

Analogously, the sky-plane velocity of a star with respect to a fixed inertial direction associated with annual parallax during an occultation by a planet at opposition is approximately

$$v_\pi = 1.4 \times 10^{-4}\ \pi\Delta \text{ km/sec}, \tag{17}$$

where $\pi$ is the annual stellar parallax in arcsec. For 28 Sgr, $1/\pi = 150$ pc (Table VII). (For simplicity we have assumed circular, coplanar planetary orbits.) The corresponding error in the derived chord length for an occultation spanning a complete ring system is:

$$dl_\pi = 2Rv_\pi/v_{\text{sky}}. \tag{18}$$

For this occultation, $dl_\pi = 0.12$ km, and the resulting effect on the derived ring radius scale and pole direction is thus quite small.

We conclude that neither proper motion nor annual parallax are important for the 28 Sgr occultation. For other occultations, however, particularly those occurring near a planet's stationary point in its orbit, for which $v_{\text{sky}}$ is small (such as an occultation by Saturn's rings observed from the Hubble Space Telescope; Elliot *et al.* 1992), uncertainties in stellar proper motion and parallax may be important sources of error in the occultation geometry, and should be taken into account.

*5.4.5. Observatory position errors.* An implicit assumption behind all of our solutions is that the observatory coordinates in Table I are perfectly known, but in the course of this study we have discovered significant inconsistencies (at the level of 500 m) between the locations tabulated in the *Astronomical Almanac* and several observatory handbooks. It is quite possible that errors at the 100-meter level are present in our adopted positions, and therefore we were prompted to determine the sensitivity of our geometric solution to small changes in station coordinates.

We performed a series of tests, first using 28 Sgr data only. These were motivated in part by trying to understand why Fits 6 and 7 to the NE and SW data sets alone (Fig. 8a) differed so substantially from the NCP results. We began by fitting the SW data alone alone and selecting the observatory that seemed likely to have the greatest leverage on the solution—in this case, the most southern site in the SW set, CTIO. We fitted for the pole direction, ephemeris offsets, and ring feature radii, after displacing the CTIO position in turn by ±10″ in latitude and longitude. The pole direction changed relatively little: 0.002° in both right ascension and declination, which is much less than the total offset of Fit 7 from our adopted solution. A similar series of fits to the NE data alone, with the IRTF position changed by ±10″ in each direction, re-

sulted in even smaller changes in the pole direction than in the SW test. It would take an unreasonably large error (5–10 km) in the CTIO or IRTF positions to force the SW-only or NE-only solutions to fall on our adopted pole. Next, we began with the conditions for Fit 13 (our adopted solution), fitting both the 28 Sgr and Voyager observations, and changed the CTIO coordinates in turn by ±10″ as before. The pole direction changed by significantly less than our adopted final error.

From these experiments, we conclude that the overall results of our final solution are insensitive to errors at the 300-m level in the observatory position. However, it is still possible that systematic patterns in the residuals for a *given* station, such as those seen in Fig. 14, can be attributed in part to such errors.

*5.4.6. Ring plane distortions.* For all of our fits, and in common with NCP, we have assumed that the rings are coplanar. The warp of Saturn's Laplace plane—the equilibrium surface about which the ring particle orbits are symmetrically distributed—due to perturbations by Tethys, Mimas, Titan, and the Sun was calculated by Burns *et al.* (1979). The effects of the predicted maximum warp on the RSS and PPS occultation measurements were tabulated by NCP (see their Table IV), who found that the largest potential influence on the apparent ring radii occurs for RSS observations of features in the A Ring. Due to the very low incidence angle for the radio occultation, a peak vertical warp of 175 m can appear as a radial shift of 1.32 km, comparable to the uncertainties in the RSS measurements and the overall fit residuals. For the less-grazing incidence of the PPS and 28 Sgr occultations (25–29°), the effects of the ring warp are less than 100 m and may be neglected for our current purposes.

## 6. SUMMARY AND DISCUSSION

We have redetermined the pole direction and ring radius scale of the Saturn system from fits to 28 Sgr and Voyager occultation observations of 30 apparently circular features in the A Ring, the Cassini Division, and the C Ring. Observations of the 3 July 1989 occultation of 28 Sgr obtained by our group (NE) from Palomar, McDonald, the IRTF and ESO were combined with measurements of the same occultation provided by H93 (the SW group) to form a comprehensive data set with multiple chords spanning both ansae of the rings. The astrometric solution utilizes a 3-D barycentric vector representation of the occultation geometry, developed for this work, which avoids the errors and approximations of some methods that have been used in the past. The new derivation of occultation astrometry also clarifies a number of subtle effects that have not been properly taken into account in previous ring orbit determinations from occultations. When correctly implemented, the sky plane and barycentric results give nearly identical results. For Saturn, both the contribution of the planet's oblateness to general relativistic bending (H93) and the motion of the planet with respect to the system barycenter are important if subkilometer accuracy is to be achieved in the reconstruction of the event geometry.

Despite the wealth of observations, and the very high quality of most of the data, we find that both the pole and ring radius scale cannot be simultaneously determined from the 28 Sgr data alone. This is due to the relatively small separation of Earth-based chords in comparison with the dimensions of the rings and to the constant observing geometry provided by a single occultation. The pole direction determined from the 28 Sgr observations alone (Fit 5) is quite uncertain and lies several standard deviations from the NCP solution, whereas the fitted radii differ by over 50 km from the NCP values, which are substantiated by independent lines of evidence. Very high correlations between the fitted parameters confirm that these results are not reliable. However, fits for either the ring pole or the radius scale alone (Fit 3 and Fit 4, respectively) yield results which are quite consistent with the pole and radii derived by NCP from Voyager occultation data. The smaller residuals obtained for Fit 4 suggest that the NCP pole is essentially correct, but that the NCP radii may be too large by 1–2 km. The postfit rms residual for this fit of 1.29 km is comparable to the measurement errors.

Voyager 1 RSS and Voyager 2 PPS data, with their very different viewing geometries, provide much stronger constraints on the system geometry. Sixty-five sharp-edged features in the Voyager PPS and RSS ring occultation data were remeasured, after scaling the observations to match the geometry and extinction efficiency of the 28 Sgr data. A fit to these new Voyager measurements alone (Fit 9), using the same 30 quasi-circular features measured in the 28 Sgr data, gave essentially identical results to those obtained by NCP, with an rms residual per degree of freedom of 0.69 km. As found by NCP, the overall uncertainties in the pole direction and radius scale are dominated by a priori spacecraft trajectory uncertainties. We find that the Voyager occultation data alone cannot be used to improve upon these a priori trajectory errors.

When both Voyager and 28 Sgr data are fitted simultaneously (Fit 11), a tightly constrained solution is obtained with a pole direction which is quite close to the NCP pole, with a *formal* uncertainty of 0.38″, a radius scale which is systematically ~1 km smaller than that found by NCP, and an rms residual of 1.31 km per degree of freedom. However, we have found that the predicted precession of Saturn's pole due to solar torques on the equatorial satellites is sufficiently rapid that it may not be

neglected over the 8.6-year interval between the Voyager 1 encounter and the 28 Sgr occultation. A series of fits with varying precession rate confirmed the anticipated motion of the pole, at a rate of 0.86 ± 0.31 times the predicted value (Fig. 10). Unlike the situation for Voyager data alone, the joint solution also permits a useful estimate of along-track spacecraft trajectory errors (Fit 13), leading to a reduction of about a factor of 3 in the systematic uncertainties for the pole and radius scale relative to the NCP solution. For this solution we fixed the pole precession rate at the predicted value. It is clear, however, that a longer span of data, provided by a combination of further ground-based and HST occultations and eventually *Cassini* occultations after 2004, should lead to a direct determination of the spin axis precession rate and thus of Saturn's polar moment of inertia.

This latter fit constitutes our adopted solution, with formal uncertainties of ±1.6″ in the pole direction and ±0.6 km in the ring radius scale. The rms residual per degree of freedom of 1.295 km is comparable to our estimated measurement errors of ~1 km, in both Voyager and 28 Sgr datasets. In comparison with the NCP results, the Saturn pole is shifted by 2.55″, whereas the absolute ring radii are reduced by an average of 0.7 ± 0.2 km (see Fig. 11 and Table X). A number of possible sources of systematic error have been investigated, but none of them appears likely to lead to changes as large as the formal errors in the fit, which we therefore regard as a realistic measure of the uncertainty of our solution.

Our results are consistent with those obtained by H93 in their parallel analysis of the joint 28 Sgr data set. In addition to employing their independently developed astrometric code and the DE-200 ephemeris for Saturn, the SW group chose to fit a somewhat smaller set of 18 features in the C Ring, Cassini Division and A Ring. (See Table I of H93 for a crosslisting of the two sets of features.) For their solution, which did not incorporate Voyager data, they adopted the ring radii determined by NCP and solved for the ring pole as well as the usual planetary ephemeris offset. Their fit is thus most comparable to our Fit 3, and indeed their derived pole at $\alpha_p$(J2000.0) = 40.5988 ± 0.02°, $\delta_p$(J2000.0) = 83.53630 ± 0.005° (or $\alpha_p$(B1950.0) = 38.421°, $\delta_p$(B1950.0) = 83.3216°) is within 2.2″ of the Fit 3 pole (see Table VIII). They conclude that there is no significant inconsistency between the 28 Sgr data and the NCP solution and concur with us that the 28 Sgr data alone cannot constrain both the pole direction and the ring radius scale.

One issue which we have been, as yet, unable to resolve to our satisfaction is the nature and true radii of the new B Ring features identified in this study. Of the 13 features originally selected for measurement (features 71–83 in Table II and Fig. 4), 8 were found to yield acceptably small radius residuals in the 28 Sgr data (see Table X). All are edges of fairly narrow zones of reduced optical depth, although it should be noted that even the minimum optical depth in these regions ranges from 0.7 to ~1.3, and is thus higher than most optical depth maxima in the C Ring and the Cassini Division. No significant differences between ingress and egress radii were detected in any of these features, making it unlikely that they are particularly noncircular, at least at the 2- to 3-km level. However, in almost every case the measured radius in the Voyager PPS data differs substantially from the fitted 28 Sgr radius, typically by 5–10 km and by 17 km in the case of feature 72. (For this reason, only 28 Sgr data were used in Fit 14.) These discrepancies are not random: for all IEGs the PPS radii show positive residuals, whereas for the two OEGs the PPS residuals are negative. This pattern is *opposite* to the PPS and RSS residuals seen for plateau features in the C Ring (cf. Fig. 12) and seems to imply that the low optical depth features in the inner B Ring are somewhat narrower in the 1-km-resolution UV data from the PPS occultation than they appear in the 20-km-resolution IR data from 28 Sgr. Whether this is indeed a wavelength-dependent effect (which would be unique to the B Ring) or an effect of the differing resolution and/or extinction efficiency of Voyager and Earth-based observations is unknown. Further investigation of these differences promises to be a fruitful area for future work. It may be possible to identify some of the lower optical depth regions in the RSS data at >1-km resolution, which might answer the question of wavelength dependence.

The most sensitive independent check of the derived radius scale probably remains the comparison of observations and models of density waves associated with satellite resonances (NCP; Rosen *et al.* 1991; Brophy and Rosen 1992), using the ~1-km-resolution Voyager occultation data sets. NCP examined a suite of 22 density waves in the PPS data for the outer A Ring driven by the satellites Prometheus and Pandora, fitting the observed locations of the peaks in the wavetrains to both an asymptotic expression derived from the linear density wave dispersion relation (Shu 1984) and actual linear wave models which incorporated the predicted phases of the individual waves. Both the dispersion relation and wave model fits showed excellent agreement between the fitted and theoretical resonance locations, with mean residuals $\delta r = r_{fit} - r_{pred}$ of −0.3 ± 0.4 km for the dispersion relation and 0.0 ± 0.2 km (Prometheus) or −0.6 ± 0.7 km (Pandora) for the linear wave models.

Rosen *et al.* (1991), in a very comprehensive study of density and bending waves in the RSS data, found mean residuals for linear model fits to the first wavelength of $\delta r = -4.0 \pm 0.9$ km, using the NCP radius scale for the RSS occultation, but ≤1 km for unweighted dispersion relation fits. The observed nonlinearity of the waves led

them to attach greater significance to the model fits, which were restricted to the linear portion of the wavetrains. A subsequent study by Brophy and Rosen (1992), however, showed that the phases of many of the Prometheus waves in the RSS data disagree with the predicted values, which complicates the interpretation of model fits. (The same waves in the PPS data appear to match the predicted phases, for reasons that are unknown; see Brophy and Rosen for further discussion.)

For the present, we may conclude that the locations and phases of the density waves, at least as seen in the PPS data, are consistent with linear models and with the NCP radius scale, perhaps favoring a slight increase (<1 km) in the radii. The present solution, which leaves the NCP radii essentially unchanged in the outer A Ring (see Fig. 11), we judge to be equally compatible with the density wave data. A caveat must be attached to this statement, however. Although the linear theory appears to match the comparatively weak Prometheus and Pandora waves fairly well, if not the much stronger waves due to Mimas, Janus, and Epimetheus, more reliable results will require the construction of density wave models that take proper account both of nonlinear effects and of surface density enhancements in the wave zone. The latter are expected due to the removal of angular momentum from the ring particles by the waves, and are seen clearly in strong waves (Longaretti and Borderies 1986). Rosen *et al.* (1991) also find evidence for density enhancements in their model fits to the weaker waves. It is likely that such models, fitted to the same data, will yield systematically different resonance locations: a rough estimate by NCP shows that a 10 gm $cm^{-2}$ (30%) change in the local surface density within the wave zone will bias the fitted resonance location by 3 km.

A second independent check on the radius scale is provided by a comparison of the "wake" driven by the Encke Gap satellite, Pan, with model predictions based on the observed orbit and location of the satellite (Showalter 1991). These results suggest that the NCP radius scale is too large by $\sim 2.9 \pm 0.8$ km in the outer A Ring. Our adopted fit reduces the Encke gap edge radii by <0.1 km, relative to NCP. Nonlinear effects in the wake might conceivably account for the discrepancy, although it must be admitted that the linear model appears to fit the observed wave extremely well.

The present solution for the pole and radius scale is intended to form a basis for future investigations of noncircular features in the rings and of the gravitational field of Saturn. Although the pole is not statistically distinct from the NCP pole, the error bars are appreciably smaller, we now have some handle on the level of likely errors in the spacecraft trajectories, and the $1\sigma$ uncertainty in the absolute radius scale has been reduced from 2.0 km to ~0.6 km. We have also obtained the first tentative detection of Saturn's pole precession. Ongoing work at JPL may eventually result in more accurate Voyager trajectories for the Saturn encounters. If the along-track corrections in the new trajectories match those determined from our astrometric fit, it will provide additional support for the results adopted here. Additional Earth-based occultation observations, as well as those made by the Hubble Space Telescope (Elliot *et al.* 1992; Bosh *et al.* 1992, Cooke *et al.* 1992), should result in a steady improvement in the pole solution, perhaps eventually reducing the present uncertainties in the radius scale to the 100-m level.

## ACKNOWLEDGMENTS

We would like to thank may people for assisting us with the observations, including Thibault Lebertre, Patrice Bouchet, and the technicians at ESO. The SW group kindly provided us with the results of their analysis prior to publication. We would also like to thank William Hubbard and Amanda Bosh for extensive cross-checks with our astrometric programs. The PDS Ring Node provided the PPS occultation data, and Paul Rosen supplied the RSS occultation data. Hester Neilan provided us with the JPL/NAIF satellite ephemerides, and William Owen supplied satellite ephemerides which we used during the development stage of this work. Doug Mink provided detailed predictions of the occultation. Neil Donahue assisted with the preparation of the synthetic Saturn figure. A comment by an anonymous reviewer led to our reinvestigation of the question of Saturn's pole precession. This work was supported in part by NASA Grants NAGW-544 and NAGW-1368, NSF Grant AST-8906011, the NASA Space Grant Program, and the Wellesley College Summer Program.

## APPENDIX A: OCCULTATION ASTROMETRY ALGORITHMS

In this appendix we derive the vector algorithm adopted in this paper for the analysis of the 28 Sgr occultation astrometry, including topocentric, Saturn barycenter, and light travel time corrections, as well as the effects of general relativistic bending of starlight by Saturn. This approach to groundbased occultation data is adapted from an algorithm originally developed in 1986 for the analysis of spacecraft stellar and radio occultation experiments by R. French and P. Nicholson, and previously applied to Voyager occultation data for the Uranian (French *et al.* 1988) and Saturnian (NCP) ring systems. It is also essentially identical to the analysis of Voyager radio occultation data for Saturn described by STH and Rosen (1989).

The vector approach avoids the small-angle and sky-curvature approximations involved in some of the more conventional "sky-plane" analyses generally used for the analysis of groundbased stellar occultation data (see, e.g., Smart 1977, Elliot *et al.* 1978), and we find it to be more conceptually transparent, but these advantages come at the expense of requiring full 3-dimensional ephemerides for the Earth, Saturn, and the Saturnian satellites, as well as some additional complications in the implementation of the GR bending correction. To clarify the relation between the vector approach and various sky-plane calculations in use, we also present here an abbreviated derivation of the key sky-plane expressions, starting with both astrometric and apparent geocentric planetary ephemerides. To $O(v/c)$, where $v$ is Saturn's velocity with respect to the Solar System barycenter, we show that all approaches yield the same ring-plane coordinates for the occulting material, although intermediate (and unobservable) quantities such as the observer–ring distance may differ significantly.

In the interests of both testing our new code, and in ensuring its compatibility with other calculations, particularly those by the SW group reported by H93, we have carried out extensive comparative calculations. Numerous small conceptual and software errors were uncovered in this process, but final comparisons between independent programs developed at Wellesley, Cornell, MIT, and the University of Arizona yielded sky-plane chord lengths which differed by only a few hundred meters, whereas ring plane radii calculated with both vector and sky-plane codes were found to agree at the 10-m level. In the course of outlining both algorithms below, we take note of several of these conceptual errors.

## *A.1. Vector Calculation*

Let the *geometric* (i.e., instantaneous) positions of the Earth's center and Saturn system barycenter with respect to the solar system barycenter at time $t$ be denoted as $\mathbf{R}_E(t)$ and $\mathbf{R}_B(t)$, respectively, whereas the offset of the center of Saturn from the Saturn system barycenter (due chiefly to Titan) is denoted $\mathbf{R}_{BS}(t)$. The barycentric position of Saturn itself is

$$\mathbf{R}_S(t) = \mathbf{R}_B(t) + \mathbf{R}_{BS}(t). \tag{A1}$$

$\mathbf{R}_E(t)$ and $\mathbf{R}_B(t)$ are obtained by interpolation in the JPL solar system ephemeris DE-130.[2] $\mathbf{R}_{BS}(t)$ is calculated from the ephemerides and masses of the principal Saturnian satellites

$$\mathbf{R}_{BS}(t) = -\sum_j (m_j/M_S)\mathbf{r}_j(t), \tag{A2}$$

where $m_j$ and $\mathbf{r}_j$ are the mass and position (relative to the system barycenter) of the $j$th satellite and $M_S$ is the mass of Saturn. All tabulated ephemerides are given in Barycentric Dynamical Time (TDB), and must thus be interpolated at time $t + \Delta BT$, where $\Delta BT = TDB - UTC$ is the difference between Coordinated Universal Time (UTC) and TDB (*Astronomical Almanac* 1992, p. B5). TDB differs from terrestrial dynamical time, TDT (the successor to ephemeris time) by at most 1.7 msec. All occultation data are recorded in, or reduced to, UTC.

The geocentric position of the observer at time $t$ is denoted $\mathbf{R}_{EO}(t)$. For the moment, we will leave the coordinate system in which these vectors are described unspecified, other than to require that it be inertial. In practice, $\mathbf{R}_E$, $\mathbf{R}_B$, and $\mathbf{R}_{BS}$ are usually given in standard equatorial coordinates (B1950.0 or J2000.0), whereas $\mathbf{R}_{EO}$ is most readily expressed in equatorial coordinates of date. It is thus necessary either (a) to apply precession and nutation to $\mathbf{R}_E$ and $\mathbf{R}_S$, or (b) to reduce $\mathbf{R}_{EO}$ to B1950.0 or J2000.0. The latter approach is to be preferred, as the somewhat tricky precession and nutation corrections are applied to the vector with the smallest lever arm in the problem (the radius of the Earth, rather than the Earth–planet separation), and as it is conceptually simpler to work in a fixed coordinate system, but many formulations have adopted the former approach. We note that nutation, even when only applied to $\mathbf{R}_{EO}$, can amount to a linear displacement of the observer of up to ~500 m, and a comparable shift in the calculated radius of a feature in the ring plane. It is therefore important that it be included, especially if data from widely separated observatories are to be combined.

*A.1.1. Barycentric calculation.* Consider an occultation event due to ring material around Saturn observed at time $t_o$ by an observer at $\mathbf{R}_{EO}$. If the unit vector to the occulted star, in the barycentric reference frame but corrected for terrestrial parallax, is denoted $\hat{\mathbf{n}}_*$, then the position $\mathbf{R}_{SI}$ of the occulting material relative to the center of Saturn is given by

$$\mathbf{R}_{SI} = \mathbf{R}_E(t_o) + \mathbf{R}_{EO}(t_o) + \Delta_I\hat{\mathbf{n}}_* - \mathbf{R}_S(t_i), \tag{A3}$$

where $t_i$ is the time at which the light ray pierced the ring plane and $\Delta_I$ is the length of the ray from ring plane intercept point to observer in the barycentric frame. (It may be necessary first to remove the aberrational "E terms" from the catalog position of the star, for compatibility with a numerical planetary ephemeris.) Requiring that the vector $\mathbf{R}_{SI}$ be orthogonal to the ring pole vector $\hat{\mathbf{n}}_p$, we obtain

$$\Delta_I = \frac{[\mathbf{R}_S(t_i) - \mathbf{R}_E(t_o) - \mathbf{R}_{EO}(t_o)] \cdot \hat{\mathbf{n}}_p}{\hat{\mathbf{n}}_* \cdot \hat{\mathbf{n}}_p}. \tag{A4}$$

For current purposes, the ring pole is assumed to be coincident with Saturn's rotation pole, but in other cases (e.g., for Uranian ring occultations) it is necessary to account for the inclination and node of the individual ring plane in computing $\hat{\mathbf{n}}_p$. Setting

$$t_i = t_o - \Delta_I/c, \tag{A5}$$

we may solve iteratively for $\Delta_I$ and $t_i$, starting with the geometric Earth–Saturn distance

$$\Delta_0 = |\mathbf{R}_S(t_o) - \mathbf{R}_E(t_o)|. \tag{A6}$$

Our algorithm determines $\mathbf{R}_{SI}$ by direct numerical iteration of Eqs. (A4) and (A5), followed by evaluation of Eq. (A3). The geometry is illustrated in Fig. A1. The longitude of the ring intercept point $\lambda_{SI}$, relative to the ascending node of the ring plane on the Earth's equator plane, is determined by rotating $\mathbf{R}_{SI}$ from Earth equatorial to ring plane coordinates:

$$[R_{SI}\cos\lambda_{SI}, R_{SI}\sin\lambda_{SI}, 0] = \mathbf{C}_1(90^\circ - \delta_p) \cdot \mathbf{C}_3(90^\circ + \alpha_p) \cdot \mathbf{R}_{SI}. \tag{A7}$$

$\mathbf{C}_i(\theta)$ denotes a clockwise coordinate system rotation through an angle $\theta$ about the $i$th axis, as viewed from the origin; $\alpha_p$ and $\delta_p$ are the right ascension and declination of the ring pole.

An additional factor which must be included in all groundbased stellar occultation reductions is an adjustment to the star position to allow for general relativistic deflection of the light ray by the planet. In the vector approach, we first determine the point of closest approach to Saturn along the geometric ray, given by the impact parameter

$$\boldsymbol{\rho} = \mathbf{R}_{EO}(t_o) + D\hat{\mathbf{n}}_* + \mathbf{R}_E(t_o) - \mathbf{R}_S(t_i), \tag{A8}$$

where the distance $D$ is given by

$$D = [\mathbf{R}_S(t_i) - \mathbf{R}_E(t_o) - \mathbf{R}_{EO}(t_o)] \cdot \hat{\mathbf{n}}_*. \tag{A9}$$

For a spherical planet, the deflected ray is given by the familiar expression

$$\hat{\mathbf{n}}_{*,d} = \hat{\mathbf{n}}_* + \frac{4GM}{c^2\rho^2}\boldsymbol{\rho}. \tag{A10}$$

An improved estimate of the deflection is obtained by iterating this procedure once, substituting $\hat{\mathbf{n}}_{*,d}$ for $\hat{\mathbf{n}}_*$. Strictly speaking, $\mathbf{R}_S$ in the above expressions should be evaluated at the time of closest approach

[2] We adopt the convention that "barycentric" refers to measurements from the center of mass of the Solar System, unless a different center of mass is explicitly identified.

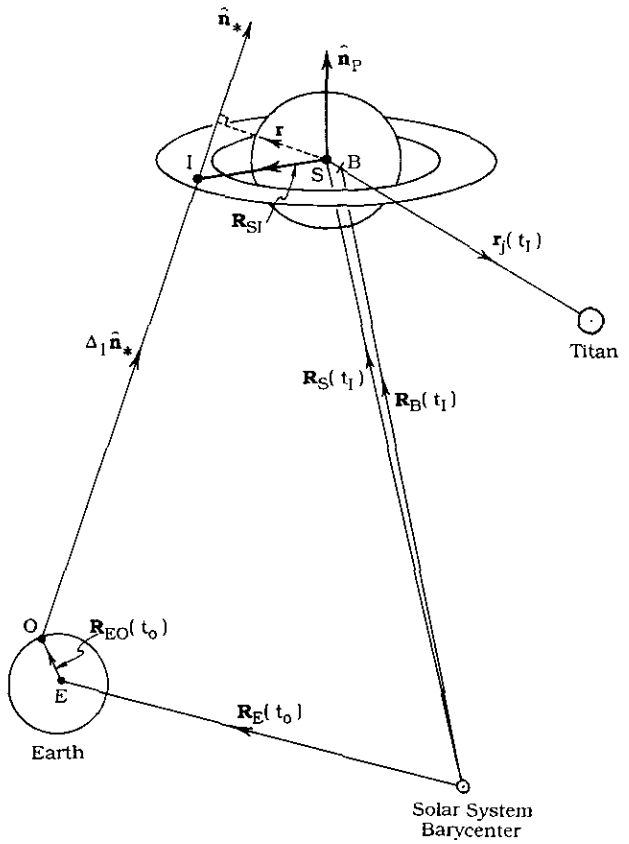


FIG. A1. Geometry for Earth-based stellar occultations, illustrating the vectors involved in the reconstruction of the ring intercept location (I) from the positions of the Earth (E), observer (O), Saturn system barycenter (B) and Titan, as well as the stellar position $\hat{\mathbf{n}}_*$ and the ring pole vector $\hat{\mathbf{n}}_P$. The impact parameter relative to Saturn's center, denoted $\mathbf{r}$, determines the general relativistic deflection of the light ray. Vector notation follows the text of Appendix A. Times $t_o$ and $t_i$ are the time of observation and the time at which the photons intercepted the ring plane, respectively.

of the ray to the planet, rather than at $t_i$, but the resulting difference in the calculated ring plane radius amounts to <1 m. Finally, $\hat{\mathbf{n}}_{*,d}$ is used in place of $\hat{\mathbf{n}}_*$ in Eqs. (A4) and (A3).

For Saturn, however, the above approximation is not adequate: the effects of the planet's gravitational oblateness (i.e., $J_2$) must be included if subkilometer precision is desired (H93). The relativistic deflection for an oblate planet, as formulated by H93, depends on the orientation of the planet's spin axis as well as the close approach vector, $\boldsymbol{\rho}$. It is most readily expressed in terms of the components of $\boldsymbol{\rho}$ perpendicular and parallel to the projection of the planet's spin axis on the plane of the sky $(\tilde{x}, \tilde{y})$:

$$[0, \tilde{x}, \tilde{y}] = \mathbf{C}_1(-P) \cdot \mathbf{C}_2(-\delta_*) \cdot \mathbf{C}_3(\alpha_*) \cdot \boldsymbol{\rho}, \tag{A11}$$

where $\alpha_*$ and $\delta_*$ are the right ascension and declination of the star, $P$ is the position angle of the spin axis in the plane of the sky, and $\rho$ is assumed to be expressed in Earth equatorial coordinates. The angular deflection of the light ray in the $(\tilde{x}, \tilde{y})$ coordinate system is given by H93,

$$\varepsilon_{\tilde{x}} = \frac{4GM}{c^2\rho^2}\left(1 - J_2R_S^2\cos^2 B\left[\frac{3\tilde{y}^2 - \tilde{x}^2}{\rho^4}\right]\right)\tilde{x}, \tag{A12}$$

$$\varepsilon_{\tilde{y}} = \frac{4GM}{c^2\rho^2}\left(1 + J_2R_S^2\cos^2 B\left[\frac{3\tilde{x}^2 - \tilde{y}^2}{\rho^4}\right]\right)\tilde{y}, \tag{A13}$$

where $M$, $R_S$, and $J_2$ are Saturn's mass, equatorial radius, and second zonal gravity coefficient, respectively, and $B$ is the inclination of the planet's equatorial plane to the line of sight. Expressions are given below for $B$ and $P$. Rotating back to equatorial coordinates, the deflected ray is given by

$$\hat{\mathbf{n}}_{*,d} = \hat{\mathbf{n}}_* + \mathbf{C}_3(-\alpha_*) \cdot \mathbf{C}_2(\delta_*) \cdot \mathbf{C}_1(P) \cdot [0, \varepsilon_x, \varepsilon_y], \tag{A14}$$

which reduces to Eq. (A10) for $J_2 = 0$. At Saturn the GR deflection for rays grazing the planet's equatorial limb amounts to $4GM/c^2R_S \simeq 2.8 \times 10^{-8}$ radians. The corresponding displacement of the ring intercept point in the plane of the sky, $\varepsilon\Delta_1 \simeq 38$ km at Saturn's distance of 9.02 AU. The additional deflection due to $J_2$ can amount to as much as 300 m in the inner C Ring, but declines to ~100 m at the outer edge of the A Ring.

A final correction must be made to the planet's interpolated position, $\mathbf{R}_S$, to allow for errors in the ephemeris. (This correction may equally be considered and implemented as a correction to the nominal star position, $\hat{\mathbf{n}}_*$: in reality only errors in the relative positions are important.) Because small errors in the planet's distance are unimportant, this correction is usually expressed in terms of components in the plane of the sky, $(f_0, g_0)$, where $f_0$ and $g_0$ are eastward and northward displacements, respectively. Following a similar procedure to that used above to describe the gravitational deflection, we write the vector correction to the planetary position as

$$\delta\mathbf{R}_S = \mathbf{C}_3(-\alpha_*) \cdot \mathbf{C}_2(\delta_*) \cdot [0, f_0, g_0]. \tag{A15}$$

The actual values of $f_0$ and $g_0$ must be determined as a part of the least-squares fit of the astrometric model to the observed ring occultation times. Typical corrections are ~1000 km, or 0.15″ on the sky. This completes the barycentric vector formulation. Appendix B provides a set of numerical data from two example calculations, against which future codes can be tested.

*A.1.2. Planetocentric calculation.* A slight simplification of the above expressions, which avoids the iterative step at some cost of precision, is to write

$$\mathbf{R}_S(t_i) \simeq \mathbf{R}_S(t_o) - \dot{\mathbf{R}}_S(t_o)(\Delta_1/c), \tag{A16}$$

where $\dot{\mathbf{R}}_S$ is the barycentric velocity of Saturn, from which we obtain

$$\mathbf{R}_{SI} \simeq \mathbf{R}_{EO}(t_o) - \mathbf{R}_{ES}(t_o) + \Delta_1(\hat{\mathbf{n}}_* + \dot{\mathbf{R}}_S/c) \tag{A17}$$

$$= \mathbf{R}_{EO}(t_o) - \mathbf{R}_{ES}(t_o) + \Delta_2\hat{\mathbf{n}}'_*, \tag{A18}$$

where

$$\Delta_2 = \frac{[\mathbf{R}_{ES}(t_o) - \mathbf{R}_{EO}(t_o)] \cdot \hat{\mathbf{n}}_p}{\hat{\mathbf{n}}'_* \cdot \hat{\mathbf{n}}_p}, \tag{A19}$$

and

$$\hat{\mathbf{n}}'_* = \frac{\hat{\mathbf{n}}_* + \dot{\mathbf{R}}_S/c}{|\hat{\mathbf{n}}_* + \dot{\mathbf{R}}_S/c|}. \tag{A20}$$

(We use the shorthand notation $\mathbf{R}_{ES}(t)$ for the instantaneous geocentric position $\mathbf{R}_S(t) - \mathbf{R}_E(t)$.)

Equations (A18) and (A19) may be interpreted as describing the occultation geometry in a reference frame at rest with respect to Saturn,

rather than in the barycentric frame of Eqs. (A3) and (A4). In the planetocentric frame, the iteration on the planet's back-dated position drops out but the barycentric star position $\hat{\mathbf{n}}_*$ is replaced by the position corrected for stellar aberration at Saturn, $\hat{\mathbf{n}}'_*$. This "trade-off" between light travel time and aberration corrections occurs frequently when calculations such as this in different reference frames are compared, and has often been the cause of considerable confusion. We shall see it again below. The distances $\Delta_1$ and $\Delta_2$ are not identical: from Eqs. (A17) and (A18), we see that

$$\Delta_2 \simeq \Delta_1(1 + \dot{\mathbf{R}}_S \cdot \hat{\mathbf{n}}_*/c). \tag{A21}$$

For the 28 Sgr occultation, $\Delta_2 - \Delta_1 \simeq -390$ km.

As in the barycentric case, it is also necessary to include corrections for GR deflection and planetary ephemeris errors. In this case, we have an impact parameter

$$\boldsymbol{\rho}' = \mathbf{R}_{EO}(t_o) + D'\hat{\mathbf{n}}'_* - \mathbf{R}_{ES}(t_o) \tag{A22}$$

where

$$D' = (\mathbf{R}_{ES}(t_o) - \mathbf{R}_{EO}(t_o)) \cdot \hat{\mathbf{n}}'_*. \tag{A23}$$

The deflected star position is substituted for $\hat{\mathbf{n}}'_*$ in Eqs. (A18) and (A19).

Equation (A18) is the most convenient form for reducing spacecraft stellar occultations, where the light travel time $\Delta_2/c$ is of order 1 sec, rather than the 1–4 hr characterizing Earth-based occultations, and the approximation in Eq. (A16) introduces negligible error. In the spacecraft case, of course, there is no topocentric correction $\mathbf{R}_{EO}$ and $\mathbf{R}_{ES}$ becomes $-\mathbf{R}_{s/c}$, the planetocentric position of the spacecraft. For 28 Sgr, $\Delta_1/c = 4501.5$ sec and the acceleration term neglected in Eq. (A16) is ~0.6 km, not completely negligible for our purposes, albeit largely in the radial ($\hat{\mathbf{n}}_*$) direction.

## *A.2. Sky Plane Calculations*

The principal differences between the two vector calculations outlined above and the conventional sky-plane calculation are: (a) the use of a tabulated geocentric ephemeris for Saturn, usually in the form of right ascension $\alpha_S$, declination $\delta_S$, and distance $\Delta_0$ and (b) an analytic approximation in which the vectors $\mathbf{R}_{ES}$ and $\mathbf{R}_{EO}$ are projected into the plane perpendicular to the stellar direction $\hat{\mathbf{n}}_*$ (the "sky plane"). It is only the second item which makes this approach fundamentally different from, and potentially less accurate than, the vector approach, but the use of a geocentric ephemeris complicates the correct treatment of the light travel time and has led to small errors in past calculations (e.g., French *et al.* 1988). Fortunately, these errors appear to be negligible for Uranus, although they would have amounted to several km for the 28 Sgr occultation.

*A.2.1. Astrometric ephemerides.* We consider first the case when an *astrometric* geocentric ephemeris of Saturn[3] is used. The astrometric position is simply the geometric position corrected for the motion of Saturn during the light travel time from the planet to the Earth

$$\begin{aligned}\mathbf{R}_{ES,A}(t) &= \mathbf{R}_S(t - \Delta_3/c) - \mathbf{R}_E(t) \\ &\simeq \mathbf{R}_{ES}(t) - \dot{\mathbf{R}}_S\Delta_3/c,\end{aligned} \tag{A24}$$

where $\Delta_3 = |\mathbf{R}_{ES,A}(t)| \simeq \Delta_0(1 - \dot{\mathbf{R}}_S \cdot \hat{\mathbf{n}}_{ES}/c)$ and we have introduced the geometric unit vector $\hat{\mathbf{n}}_{ES} = \mathbf{R}_{ES}/\Delta_0$. No stellar aberration is applied, so the position is in the barycentric reference frame.

[3] If the ephemeris is of the barycenter, then it is to be understood that a correction $\mathbf{R}_{BS}$ has been applied as described above.

From Eq. (A17), the position of the occulting material relative to Saturn is given by

$$\mathbf{R}_{SI} = \Delta_1\hat{\mathbf{n}}_* - \mathbf{R}_{ES,A}(t_o) + \mathbf{R}_{EO}(t_o) + \dot{\mathbf{R}}_S\delta t \tag{A25}$$

where the residual light travel time

$$\begin{aligned}\delta t &= (\Delta_1 - \Delta_3)/c \\ &\simeq (\mathbf{R}_{SI} - \mathbf{R}_{EO}) \cdot \hat{\mathbf{n}}_*/c\end{aligned} \tag{A26}$$

allows for the extra projected distance from Saturn's center to the ring intercept point, and the correction from Earth center to observer. If we rewrite Eq. (A25), splitting $\Delta_1$ into its two components, we get

$$\mathbf{R}_{SI} = \Delta_3\hat{\mathbf{n}}_* - \mathbf{R}_{ES,A}(t_o) + \mathbf{R}_{EO}(t_o) + (c\hat{\mathbf{n}}_* + \dot{\mathbf{R}}_S)\delta t, \tag{A27}$$

$$= \Delta_3[\hat{\mathbf{n}}_* - \hat{\mathbf{n}}_{ES,A}(t_o)] + \mathbf{R}_{EO}(t_o) + (c\hat{\mathbf{n}}_* + \dot{\mathbf{R}}_S)\delta t, \tag{A28}$$

where we have introduced the astrometric unit vector $\hat{\mathbf{n}}_{ES,A} = \mathbf{R}_{ES,A}/\Delta_3$. This expression is identical to Eq. (A17), as may readily be verified by substituting for $\mathbf{R}_{ES,A}$ in terms of $\mathbf{R}_{ES}$ and recombining $\Delta_3$ and $c\delta t$ into $\Delta_1$.

We expand Eq. (A28) later into explicit sky-plane components. The corresponding geometry is illustrated in Fig. A2. Note that the three terms on the RHS have simple physical interpretations: the first accounts for the offset on the sky between the star and Saturn's center, as seen from the center of the Earth; the second accounts for the position of the observer in Saturn's shadow; and the third is the correction for light travel time between the sky-plane and the ring plane. In the context of the last term, note that it is the *barycentric* velocity of Saturn which enters, rather than the geocentric velocity as might be supposed. This error was discovered to have persisted in at least two of our computer codes for at least 5 years, although the relatively small dimensions (~0.17 light second) and pole-on orientation of the Uranian ring plane greatly reduced its importance. For Saturn, the maximum ring radius is ~0.47 light seconds and the error in replacing $\dot{\mathbf{R}}_S$ by $\dot{\mathbf{R}}_{ES}$ can amount to several km.

*A.2.2. Apparent ephemerides.* We consider now the alternative case when an *apparent* geocentric ephemeris of Saturn is used, such as is provided by the *Astronomical Almanac*. In this case, the tabulated positions are corrected for both light travel time, as in the astrometric case, and terrestrial stellar aberration,

$$\begin{aligned}\mathbf{R}_{ES,a}(t) &= \mathbf{R}_{ES,A}(t) + \dot{\mathbf{R}}_E\Delta_3/c \\ &= \mathbf{R}_{ES}(t) - \dot{\mathbf{R}}_{ES}\Delta_3/c \\ &= (1 + \sigma)\Delta_3\hat{\mathbf{n}}_{ES,a},\end{aligned} \tag{A29}$$

where $1 + \sigma = |\hat{\mathbf{n}}_{ES,A}(t) + \dot{\mathbf{R}}_E/c|$. Thus we have the apparent unit vector

$$\hat{\mathbf{n}}_{ES,a} = \frac{\hat{\mathbf{n}}_{ES,A} + \dot{\mathbf{R}}_E/c}{1 + \sigma}. \tag{A30}$$

In addition, the star position must now be corrected for stellar aberration,

$$\hat{\mathbf{n}}_{*,a} = \frac{\hat{\mathbf{n}}_* + \dot{\mathbf{R}}_E/c}{1 + \varepsilon}, \tag{A31}$$

where $1 + \varepsilon = |\hat{\mathbf{n}}_* + \dot{\mathbf{R}}_E/c|$. It is necessary to recompute the apparent planet and star positions separately for each ring event, due to the acceleration of the Earth.

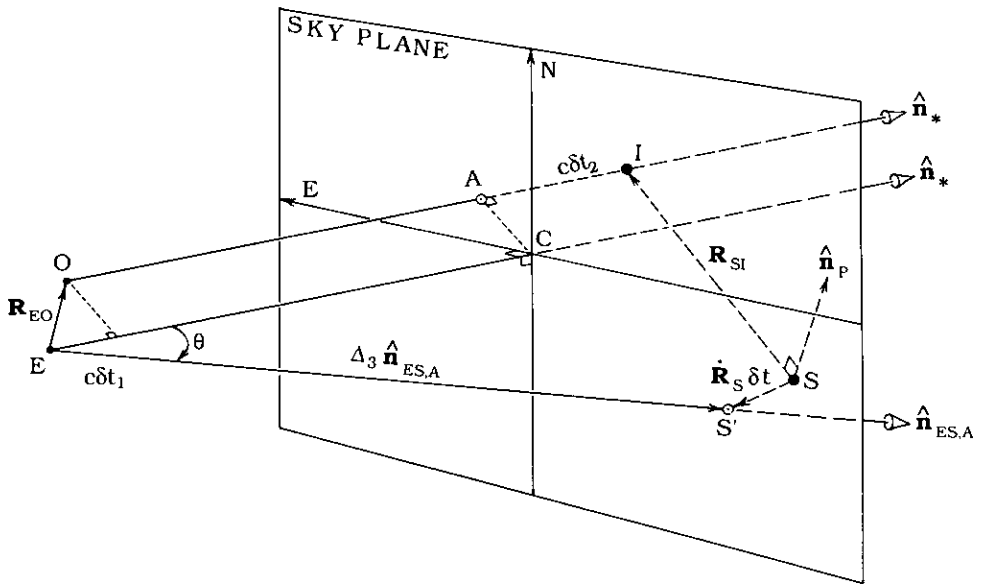


FIG. A2. The sky-plane representation of stellar occultation geometry. The locations of Earth (E) and observer (O) at time $t_0$, and the astrometric position of Saturn's center (S') at $t_0 - \Delta_3/c$ are indicated, as are the back-dated position of Saturn (S) at the moment the ray intercepted the ring plane, $t_i$, and the ring intercept point (I). The sky-plane is perpendicular to the stellar direction, $\hat{\mathbf{n}}_*$, and passes through S' at a distance $\Delta_3$ from the Earth. A denotes the projection of the observer's position into the sky-plane. The ring intercept point lies along the prolongation of the line OA, at a point such that the vector SI is perpendicular to the ring plane normal $\hat{\mathbf{n}}_P$. The distance OI determines the actual light travel time $\Delta_1/c$. The residual light travel time, $\delta t = (\Delta_1 - \Delta_3)/c \simeq \delta t_2 - \delta t_1$, where the topocentric and sky-to-ring plane distances $c\delta t_1$ and $c\delta t_2$ are indicated in the diagram. The angle $\theta$ between the stellar and planetary directions is $\leq 20'' \sim 10^{-4}$ rad, so that the difference between $\Delta_3$ and the distance EC, $(1 - \cos\theta)\Delta_3 \lesssim 6$ km, corresponding to a negligible error in $\delta t$ of $\leq 20$ $\mu$sec.

Substituting these expressions into Eq. (A27), we have

$$\begin{aligned}\mathbf{R}_{SI} &= \Delta_3(1+\varepsilon)\hat{\mathbf{n}}_{*,a} - \mathbf{R}_{ES,a}(t_o) + \mathbf{R}_{EO}(t_o) \\ &\quad + [c(1+\varepsilon)\hat{\mathbf{n}}_{*,a} + \dot{\mathbf{R}}_{ES}]\delta t, \qquad \text{(A32)}\\ &= \Delta_3[(1+\varepsilon)\hat{\mathbf{n}}_{*,a} - (1+\sigma)\hat{\mathbf{n}}_{ES,a}(t_o)] + \mathbf{R}_{EO}(t_o) \\ &\quad + [c(1+\varepsilon)\hat{\mathbf{n}}_{*,a} + \dot{\mathbf{R}}_{ES}]\delta t. \qquad \text{(A33)}\end{aligned}$$

Now $\varepsilon - \sigma \simeq (\hat{\mathbf{n}}_* - \hat{\mathbf{n}}_{ES,A}) \cdot \dot{\mathbf{R}}_E/c \lesssim 10^{-8}$, so that we may safely set $\sigma = \varepsilon$ to obtain the final result for the ring intercept vector in terms of apparent positions

$$\mathbf{R}_{SI} \simeq \Delta_4[\hat{\mathbf{n}}_{*,a} - \hat{\mathbf{n}}_{ES,a}(t_o)] + \mathbf{R}_{EO}(t_o) + [c(1+\varepsilon)\hat{\mathbf{n}}_{*,a} + \dot{\mathbf{R}}_{ES}]\delta t, \quad \text{(A34)}$$

where $\Delta_4 = (1+\sigma)\Delta_3 = |\mathbf{R}_{ES,a}(t_o)|$.

Equation (A34) may be compared with the analogous expression involving astrometric positions, Eq. (A28). The three terms on the RHS again correspond to the star–Saturn center offset (apparent), the position of the observer in Saturn's shadow, and the residual light travel time correction. There are, however, two important differences between the two expressions: (a) the apparent distance to Saturn $\Delta_4$ must be used in place of the astrometric distance $\Delta_3$; and (b) the light travel time correction involves the geocentric velocity of Saturn $\dot{\mathbf{R}}_{ES}$ rather than the barycentric velocity $\dot{\mathbf{R}}_S$. The former is particularly important to note, as the *Astronomical Almanac* tabulates the geometric distance $\Delta_0$, rather than the apparent distance in its listing of apparent planetary coordinates. Combining the above expressions for $\Delta_0$, $\Delta_3$, and $\Delta_4$, we have the usual relation between the apparent distance and the back-dated geometric distance

$$\begin{aligned}\Delta_4(t_o) &= \Delta_0(t_o)[1 + (\dot{\mathbf{R}}_E - \dot{\mathbf{R}}_S)\cdot\hat{\mathbf{n}}_{ES}/c] \\ &= \Delta_0(t_o)[1 - \dot{\mathbf{R}}_{ES}\cdot\hat{\mathbf{n}}_{ES}/c] \qquad \text{(A35)}\\ &= \Delta_0(t_o - \Delta_0/c).\end{aligned}$$

The equivalence of Eqs. (A28) and (A34), at least to $O(\dot{\mathbf{R}}_S/c)$ and $O(\dot{\mathbf{R}}_E/c)$, is demonstrated by their mutual derivation from the approximate vector expression Eq. (A17). In fact, even the individual terms are equivalent, as we have shown above that

$$\hat{\mathbf{n}}_{*,a} - \hat{\mathbf{n}}_{ES,a} \simeq (\hat{\mathbf{n}}_* - \hat{\mathbf{n}}_{ES,A})/(1+\sigma), \qquad \text{(A36)}$$

which cancels the factor of $1 + \sigma$ in $\Delta_4/\Delta_3$, whereas it is also readily seen that the light travel term in Eq. (A28)

$$\begin{aligned}(c\hat{\mathbf{n}}_* + \dot{\mathbf{R}}_S)\delta t &\simeq (c\hat{\mathbf{n}}_* + \dot{\mathbf{R}}_E + \dot{\mathbf{R}}_{ES})\delta t \\ &= [(1+\varepsilon)c\hat{\mathbf{n}}_{*,a} + \dot{\mathbf{R}}_{ES}]\delta t\end{aligned} \qquad \text{(A37)}$$

which is identical to the third term in Eq. (A34). This is really another example of light travel time (in this case $\Delta_3$ vs $\Delta_4$ and $c\delta t$ vs $(1+\varepsilon)c\delta t$) being traded for aberration (barycentric vs apparent unit vectors).

*A.2.3. Planetocentric ephemerides.* In the context of the above comparisons of calculations with astrometric and apparent ephemerides, it is instructive also to examine the case of a planetocentric ephemeris (i.e., an ephemeris giving apparent positions as seen by an observer on Saturn). The vector expression for this case has been already given as Eq. (A18) above, but we start with Eq. (A28) instead. Proceeding in

parallel to the case of terrestrial apparent coordinates, we correct both the astrometric geocentric position of Saturn and the star direction for stellar aberration *as seen by Saturn*,

$$\begin{aligned}\mathbf{R}_{ES,s}(t) &= \mathbf{R}_{ES,A}(t) + \dot{\mathbf{R}}_S\Delta_3/c \\ &= \mathbf{R}_{ES}(t)\end{aligned} \tag{A38}$$

and

$$\hat{\mathbf{n}}'_* = \frac{\hat{\mathbf{n}}_* + \dot{\mathbf{R}}_S/c}{1+\tau}, \tag{A39}$$

where $1 + \tau = |\hat{\mathbf{n}}_* + \dot{\mathbf{R}}_S/c|$. We see that the aberrated planet position is simply the geometric position $\mathbf{R}_{ES}(t_0)$. Although strange at first glance, this simply means that the apparent saturnicentric position of the Earth, $-\mathbf{R}_{ES}$, is the actual position of the Earth at the time the light is received, minus the position of Saturn itself which is fixed. Thus the apparent geocentric position of Saturn (in Saturn's reference frame) becomes

$$\hat{\mathbf{n}}_{ES,s} = \hat{\mathbf{n}}_{ES} = \frac{\hat{\mathbf{n}}_{ES,A} + \dot{\mathbf{R}}_S/c}{1+\mu}, \tag{A40}$$

where $1 + \mu = |\hat{\mathbf{n}}_{ES,A} + \dot{\mathbf{R}}_S/c| \simeq 1 + \tau$. Substituting these expressions into Eq. (A28), and noting that $\Delta_3 \simeq \Delta_0(1 - \tau)$ we obtain

$$\mathbf{R}_{SI} = \Delta_0[\hat{\mathbf{n}}'_* - \hat{\mathbf{n}}_{ES}] + \mathbf{R}_{EO}(t_0) + c(1+\tau)\hat{\mathbf{n}}'_*\delta t. \tag{A41}$$

Comparison with Eqs. (A28) and (A34) shows the same three terms, with the same physical interpretation, and it is readily shown that the individual terms are also equal to those in Eq. (A28)

$$\begin{aligned}\hat{\mathbf{n}}'_* - \hat{\mathbf{n}}_{ES} &= [\hat{\mathbf{n}}_* - \hat{\mathbf{n}}_{ES,A}]/(1+\tau) \\ &\simeq \Delta_3/\Delta_0[\hat{\mathbf{n}}_* - \hat{\mathbf{n}}_{ES,A}],\end{aligned} \tag{A42}$$

$$c(1+\tau)\hat{\mathbf{n}}'_*\delta t = (c\hat{\mathbf{n}}_* + \dot{\mathbf{R}}_S)\delta t. \tag{A43}$$

Again we have aberration trading for light travel time, but in this case the final expression, Eq. (A41) is particularly simple: it involves only the geometric distance $\Delta_0$, the geometric unit vector $\hat{\mathbf{n}}_{ES}$, and the apparent star position in Saturn's frame $\hat{\mathbf{n}}'_*$. Moreover, the residual light travel correction is purely in the radial ($\hat{\mathbf{n}}'_*$) direction, and thus has no component in the sky-plane. Thus only when we use the planetocentric frame can the light time correction be omitted from the sky-plane calculation.

This has its counterpart in the simplicity of the planetocentric vector expression, Eqs. (A18) and (A19), in which only geometric positions enter and for which no iteration on the light travel time is necessary.

We thus have three separate sky-plane formulations—astrometric, apparent, and planetocentric—all of which yield identical results to $O(v/c)$ and which are equivalent to the approximate vector expression Eq. (A17). The four expressions for $\mathbf{R}_{SI}$, Eqs. (A17), (A28), (A34), and (A41), may, however, be expected to differ fractionally by terms of order $(\dot{\mathbf{R}}_S/c)^2$, $(\dot{\mathbf{R}}_E/c)^2$, $(\hat{\mathbf{n}}_* - \hat{\mathbf{n}}_{ES}) \cdot \dot{\mathbf{R}}_{ES}/c$, and $d^2\mathbf{R}_S/dt^2\Delta_3/c^2$, or $\sim 10^{-8}$. The errors associated with using them in place of the exact vector expression Eq. (A3) should therefore be of order 1–10 m in ring plane position, an expectation borne out by our numerical calculations and summarized in Appendix B.

*A.2.4. Sky-plane coordinates.* Although Eqs. (A28), (A34), or (A41) are written most compactly in vector form, they are usually implemented in terms of sky-plane coordinates $(f, g)$, a local cartesian coordinate system erected in the plane perpendicular to the stellar direction $\hat{\mathbf{n}}_*$ (or $\hat{\mathbf{n}}_{*,a}$ in the case of calculations using apparent positions, or $\hat{\mathbf{n}}'_*$ for geometric positions—for simplicity we shall assume an astrometric calculation here). Note that $f$ is measured toward the east on the sky, and $g$ toward the north. The third component, $h$, is directed radially away from the Earth, in the direction $\hat{\mathbf{n}}_*$ (see Fig. A2).

Starting with vector components $(x, y, z)$ in an Earth equatorial system (e.g., B1950, J2000, or coordinates of date), with the $z$ axis toward celestial north and the $x$ axis toward the vernal equinox, we may rotate these components into the $(h, f, g)$ system via the symbolic procedure

$$[h, f, g] = \mathbf{C}_2(-\delta_*) \cdot \mathbf{C}_3(\alpha_*) \cdot [x, y, z], \tag{A44}$$

where again $\mathbf{C}_i(\theta)$ denotes a coordinate system rotation through an angle $\theta$ about the $i$th axis ($1 = x$, $2 = y$, $3 = z$). Applying this rotation to the planet position $\hat{\mathbf{n}}_{ES,A}$ we obtain

$$\begin{aligned}\hat{\mathbf{n}}_{ES,A} = &(\cos\delta_*\cos\delta_S\cos\Delta\alpha + \sin\delta_*\sin\delta_S)\hat{\mathbf{h}} \\ &+ \cos\delta_S\sin\Delta\alpha\hat{\mathbf{f}} \\ &+ (\cos\delta_*\sin\delta_S - \sin\delta_*\cos\delta_S\cos\Delta\alpha)\hat{\mathbf{g}},\end{aligned} \tag{A45}$$

where $\delta_*$ and $\delta_S$ are the declinations of the star and Saturn, respectively, and $\Delta\alpha = \alpha_S - \alpha_*$ is the difference in their right ascensions. The geocentric position of the observer (in coordinates of date) is similarly given by

$$\begin{aligned}\mathbf{R}_{EO} = &R(\cos\delta_*\cos\phi\cos H + \sin\delta_*\sin\phi)\hat{\mathbf{h}} \\ &+ R\cos\phi\sin H\hat{\mathbf{f}} \\ &+ R(\cos\delta_*\sin\phi - \sin\delta_*\cos\phi\cos H)\hat{\mathbf{g}},\end{aligned} \tag{A46}$$

where $R$ is the geocentric radius, $\phi$ is the geocentric latitude, and $H$ is the local hour angle of the star. (Note that the geocentric, rather than geodetic, latitude must be used here.) Once the observer's position has been computed, precession and nutation may be applied to convert $\mathbf{R}_{EO}$ from coordinates of date to any desired epoch. By definition, $\hat{\mathbf{n}}_* = \hat{\mathbf{h}}$.

Equation (A28) then yields the sky-plane coordinates of the ring intercept vector $\mathbf{R}_{SI}$, relative to the center of Saturn

$$f = R\cos\phi\sin H - \Delta_3\cos\delta_S\sin\Delta\alpha + (\dot{\mathbf{R}}_S)_f\delta t \tag{A47}$$

$$\begin{aligned}g = &R(\cos\delta_*\sin\phi - \sin\delta_*\cos\phi\cos H) \\ &- \Delta_3(\cos\delta_*\sin\delta_S - \sin\delta_*\cos\delta_S\cos\Delta\alpha) + (\dot{\mathbf{R}}_S)_g\delta t,\end{aligned} \tag{A48}$$

as given by Elliot *et al.* (1978), but with the addition of the residual light travel term. The radial ($h$) component of $\mathbf{R}_{SI}$ depends on the initially unknown value of $\delta t$, but may be obtained instead by requiring that $\mathbf{R}_{SI} \cdot \hat{\mathbf{n}}_p = 0$. The orientation of the ring plane is specified by its inclination to the line of sight to the star ($B$), and the position angle of Saturn's north pole relative to celestial north (the $g$ direction on the sky) ($P$), which are given by

$$\sin B = -\cos\delta_p\cos\delta_*\cos(\alpha_* - \alpha_p) - \sin\delta_p\sin\delta_* \tag{A49}$$

$$\cos B\sin P = -\cos\delta_p\sin(\alpha_* - \alpha_p) \tag{A50}$$

$$\cos B\cos P = -\cos\delta_p\sin\delta_*\cos(\alpha_* - \alpha_p) + \sin\delta_p\cos\delta_*, \tag{A51}$$

where $\alpha_p$ and $\delta_p$ are the right ascension and declination of Saturn's rotation pole.

As discussed above, it is necessary to allow for errors in the planetary ephemeris or star position, neither of which is known a priori to the desired accuracy of <1 km, or $\sim 10^{-4}$ arcsec for Saturn. This is accomplished most economically here by simply applying an ephemeris correction $(f_0, g_0)$ to the raw sky-plane coordinates. This offset is subsequently solved for using ring features of known absolute radii. After

converting the corrected sky-plane position to polar coordinates

$$f - f_0 = \rho \sin\theta, \quad g - g_0 = \rho \cos\theta, \tag{A52}$$

we apply the correction for GR deflection using the geometric impact parameter $\rho$. For a spherical planet, the corrected impact parameter is

$$\rho_d = \rho\left(1 + \frac{4GM}{c^2\rho^2}\Delta_3\right). \tag{A53}$$

For an oblate planet, the procedure described by H93 and outlined above must be used. The resulting sky-plane position is projected into the ring plane at a radius

$$R_{SI} = \rho_d[\cos^2(\theta - P)/\sin^2 B + \sin^2(\theta - P)]^{1/2}. \tag{A54}$$

The corresponding line-of-sight component is given by

$$h = \rho_d \cos(\theta - P)/\tan B, \tag{A55}$$

from which we obtain the residual light travel time

$$\delta t = [h - R(\cos\delta_* \cos\phi \cos H + \sin\delta_* \sin\phi)]/c, \tag{A56}$$

which is then substituted into Eqs. (A47) and (A48) to refine iteratively the estimates of $f$ and $g$. This completes the formulation of the sky-plane calculation.

Note that in going from the sky-plane coordinates $(f, g)$ to ring plane radius $R_{SI}$, and in evaluating the light time $\delta t$, we have calculated the ring plane angles $B$ and $P$ using the position of the star, $(\alpha_*, \delta_*)$, rather than the planet's position $(\alpha_S, \delta_S)$. This is because the direction of the light ray maintains a constant angle to the ring plane $(B)$, while the inclination of this plane relative to the direction toward the *planet* changes perceptibly during the course of the occultation. Similarly, the azimuth of the ring pole $(P)$ must remain constant relative to the fixed stellar direction. Although it is also possible to formulate this transformation in terms of the slowly varying $(B, P)$ calculated using the planet position, it is then necessary to apply "perspective" corrections (cf. Elliot *et al.* 1981) as the angular separation of planet and star increases. Numerical experiments showed that, for the 28 Sgr occultation, improper treatment of these effects can lead to errors in the ring plane radius of up to 8 km. The corresponding errors at Uranus would be much less, due to the smaller angular dimensions of the Uranian ring system.

### *A.3. Summary*

We have outlined above five different approaches to the reduction of Earth-based stellar occultation data: two based on a purely vector scheme, in the barycentric (Eq. (A3) and (A4)) and planetocentric (Eqs. (A18) and (A19)) reference frames; and three based on geocentric ephemerides suitable for sky-plane expansions, using astrometric (Eq. (A28)), apparent (Eq. (A34)) and geometric (Eq. (A41)) ephemerides. Most, if not all, of these approaches have been used in previous published analyses of either spacecraft or Earth-based data, although the relations between them have not been explored in detail. Note that to $O(v/c)$, we have shown that all four approximate methods yield the same ring-plane coordinates of the occulting material. These analytic demonstrations have been partially confirmed by our numerical experiments, summarized in Appendix B, which show satisfactory (~10 m) agreement between independently developed barycentric vector codes and between these and an astrometric sky-plane code.

In the course of formalizing these methods, however, the importance of several secondary effects or corrections has been underscored, and in some cases errors in preexisting codes identified. As a guide to future workers in this field, we have noted these points as they arose naturally in the derivations above. In summary, they include:

1. corrections for the motion of the planet relative to the barycenter of the planet–satellite system, as given in most Solar System ephemerides—this is important mostly for Jupiter and Saturn;
2. the need for consistency in applying precession and nutation corrections to the planet, star and observer positions—we recommend the conceptually simple approach of precessing the observer position rather than the use of planet and star positions of date (note that it is necessary to account for nutation as well as precession if subkilometer accuracy is required);
3. the correct treatment of the residual ring-to-sky-plane and topocentric light travel time corrections—the barycentric planet velocity should be used with an astrometric ephemeris, the geocentric velocity with an apparent ephemeris, and no correction is needed with a geometric ephemeris;
4. the use of the appropriate Earth–planet distance in sky-plane calculations—the back-dated astrometric distance ($\Delta_3$) with astrometric ephemerides, the apparent distance ($\Delta_4$) with apparent ephemerides, and the geometric distance ($\Delta_0$) with geometric ephemerides;
5. the desirability of calculating the ring-plane orientation angles, $B$ and $P$, from the (fixed) stellar position rather than from the (moving) planetary position, to avoid unnecessary perspective or parallax effects entering the calculation; and
6. corrections for general relativistic bending, if necessary taking into account the oblateness of the planet's gravity field (i.e., $J_2$).

Instances of virtually every one of these items being improperly handled or neglected have been identified in the five different computer codes scrutinized during the course of this study, several of which have been in use for many years. In most cases, the errors were unimportant for Uranus or Neptune occultations, but became significant at Saturn because of the larger dimensions of its ring system and because of our much better a priori knowledge of the planet's pole vector and of the absolute radius scale of the rings.

## APPENDIX B: DETAILS OF ASTROMETRIC CALCULATIONS

In this appendix, we present details of our astrometric solution. We begin by presenting sample barycentric calculations for two of the data points used in Fit 12, giving sufficient detail to allow comparison of our results with those of other investigators. We then present abbreviated results for additional astrometric calculations for these two test points, using two completely independent barycentric computer codes. These serve both as additional cross-checks for other investigators and to quantify the importance of several small but important geometrical effects described in Appendix A. Next, we compare the sky-plane and barycentric fitting methods as implemented in the code actually used to perform the astrometric fits presented in this work, and finally, we compare the results of our orbit-fitting algorithm with those of the SW group (H93).

### *B.1. Sample Barycentric Calculations*

To provide guidance to others who wish to implement the barycentric vector algorithm described in Appendix A, we have selected two representative data points used in our fits, and have tabulated a number of intermediate quantities in the calculation. The objective of our sample calculation is to determine $\mathbf{R}_{SI}$, the position of the occulting material

TABLE B-I
**Instantaneous Saturn and Earth Ephemerides**

| | $\mathbf{R}_B$[b] | | | $\dot{\mathbf{R}}_B$[b] | | |
|---|---|---|---|---|---|---|
| TDB[a] | $x$ | $y$ | $z$ | $\dot{x}$ | $\dot{y}$ | $\dot{z}$ |
| 4:30:00 | 262628476.27939 | −1362112118.50631 | −574685461.69059 | 8.988960 | 1.684982 | 0.308026 |
| 4:40:00 | 262633869.65341 | −1362111107.50767 | −574685276.87101 | 8.988954 | 1.685014 | 0.308039 |
| 4:50:00 | 262639263.02373 | −1362110096.48980 | −574685092.04332 | 8.988947 | 1.685046 | 0.308053 |
| 5:00:00 | 262644656.39033 | −1362109085.45271 | −574684907.20751 | 8.988941 | 1.685078 | 0.308066 |
| 7:10:00 | 262714769.81856 | −1362095940.22079 | −574682503.60385 | 8.988861 | 1.685494 | 0.308242 |
| 7:20:00 | 262720163.13322 | −1362094928.91451 | −574682318.65448 | 8.988855 | 1.685526 | 0.308256 |
| 7:30:00 | 262725556.44417 | −1362093917.58901 | −574682133.69699 | 8.988848 | 1.685559 | 0.308269 |
| 7:40:00 | 262730949.75141 | −1362092906.24428 | −574681948.73139 | 8.988842 | 1.685591 | 0.308283 |
| | $\mathbf{R}_{BS}$[c] | | | $\dot{\mathbf{R}}_{BS}$[c] | | |
| TDB | $x$ | $y$ | $z$ | $\dot{x}$ | $\dot{y}$ | $\dot{z}$ |
| 4:30:00 | −242.030675 | 131.366228 | 10.890477 | −0.000714 | −0.001186 | 0.000145 |
| 4:40:00 | −242.458036 | 130.653786 | 10.977393 | −0.000711 | −0.001189 | 0.000145 |
| 4:50:00 | −242.883277 | 129.939726 | 11.064223 | −0.000707 | −0.001191 | 0.000145 |
| 5:00:00 | −243.306386 | 129.224054 | 11.150964 | −0.000703 | −0.001194 | 0.000145 |
| 7:10:00 | −248.607977 | 119.777153 | 12.269871 | −0.000655 | −0.001228 | 0.000142 |
| 7:20:00 | −249.000125 | 119.039743 | 12.355214 | −0.000652 | −0.001230 | 0.000142 |
| 7:30:00 | −249.389982 | 118.300845 | 12.440446 | −0.000648 | −0.001233 | 0.000142 |
| 7:40:00 | −249.777538 | 117.560468 | 12.525564 | −0.000644 | −0.001235 | 0.000142 |
| | $\mathbf{R}_E$[d] | | | $\dot{\mathbf{R}}_E$[d] | | |
| TDB | $x$ | $y$ | $z$ | $\dot{x}$ | $\dot{y}$ | $\dot{z}$ |
| 5:40:00 | 28064949.88541 | −137049642.75275 | −59424472.56075 | 28.803991 | 4.989791 | 2.163963 |
| 5:50:00 | 28082232.08671 | −137046647.94193 | −59423173.77679 | 28.803346 | 4.992912 | 2.165317 |
| 6:00:00 | 28099513.90096 | −137043651.25874 | −59421874.18014 | 28.802701 | 4.996032 | 2.166672 |
| 6:10:00 | 28116795.32791 | −137040652.70323 | −59420573.77084 | 28.802055 | 4.999153 | 2.168026 |
| 6:20:00 | 28134076.36730 | −137037652.27543 | −59419272.54890 | 28.801409 | 5.002273 | 2.169380 |
| 8:20:00 | 28341418.51836 | −137001501.12056 | −59403594.50785 | 28.793623 | 5.039712 | 2.185630 |
| 8:30:00 | 28358694.49645 | −136998476.35728 | −59402282.72360 | 28.792971 | 5.042832 | 2.186984 |
| 8:40:00 | 28375970.08342 | −136995449.72236 | −59400970.12701 | 28.792319 | 5.045951 | 2.188338 |
| 8:50:00 | 28393245.27903 | −136992421.21585 | −59399656.71811 | 28.791666 | 5.049070 | 2.189692 |
| 9:00:00 | 28410520.08303 | −136989390.83779 | −59398342.49691 | 28.791014 | 5.052190 | 2.191046 |

[a] TDB (Barycentric Dynamical Time) on 3 July 1989. On this date, TDB–UTC=56.1840 s.
[b] Position (km) and velocity (km/s) of the Saturn system barycenter with respect to the solar system barycenter, in B1950.0 coordinates, from the DE–130 ephemeris (Standish 1987, 1990).
[c] Position (km) and velocity (km/s) of Saturn with respect to the Saturn system barycenter, in B1950.0 coordinates, computed from Saturn satellite ephemerides obtained from JPL/NAIF File SAT018H.BSP (Acton 1990).
[d] Position (km) and velocity (km/s) of Earth with respect to the solar system barycenter, in B1950.0 coordinates, from the DE–130 ephemeris (Standish 1987, 1990).

represented by the two occultation events, using Eqs. (A1)–(A15) of Appendix A. The first test point (designated PAL 1i) is the ingress PAL feature 1 (the outer edge of the Keeler Gap). This occurs near the onset of the occultation, and at a sufficiently large distance from Saturn that GR bending is moderate. By contrast, the second test point (MCD 38e) is the egress MCD feature 38, located in the inner C Ring, where GR bending is somewhat greater. The chord separating the two events is large enough to provide additional checks on the time-dependent aspects of the calculation. In calculating the sample results, we used the values given in Table VII for geometrical and physical parameters for the Saturn system and the station coordinates for MCD and PAL given in Table I.

In Table B-I, we have tabulated the instantaneous ephemerides of Saturn and the Earth at 10-min intervals for the time periods appropriate for the two test points. Because of the iterative nature of the calculations implicit in Eqs. (A4) and (A5), one must interpolate the barycenter position repeatedly until satisfactory convergence is achieved; in practice, two iterations are usually sufficient.

Additional information required for the calculations is given in Table B-II.[4] All calculations have been performed using the Cornell University version of the barycentric vector code, which directly implements the algorithm described in Appendix A. First, the observer position relative to the Solar System barycenter is determined by combining the barycentric coordinates of the Earth's center, $\mathbf{R}_E$, (obtained by interpolation from the DE-130 ephemeris) with the geocentric observer position, $\mathbf{R}_{EO}$. The latter quantity was computed by coverting from geodetic to geocentric coordinates (Table I), using the Earth's radius and flatten-

[4] Quantities are given to artificially high precision to permit precise comparison of results and to avoid round-off error. In addition, note that the **Table B-II** values for $\alpha_P$, $\delta_P$, $f_0$, and $g_0$ correspond to Fit 12, whereas those given in **Table X** correspond to Fit 13.

TABLE B-II

Sample Barycentric Vector Calculations[a]

| Saturn Pole Direction | | Star Direction | | Planet Ephemeris Offsets[b] | |
|---|---|---|---|---|---|
| $\alpha_P$(B1950.0) | 38.4100990 | $\alpha_*$(B1950.0) | 280.8324776979 | $f_0$(B1950.0) | 990.353 |
| $\delta_P$(B1950.0) | 83.3235386 | $\delta_*$(B1950.0) | −22.4463567333 | $g_0$(B1950.0) | −828.478 |
| $\hat{\mathbf{n}}_{Px}$ | 0.0911015924 | $\hat{\mathbf{n}}_{*x}$ | 0.173699411688 | $\delta\mathbf{R}_{Sx}$ | 913.256 |
| $\hat{\mathbf{n}}_{Py}$ | 0.0722323811 | $\hat{\mathbf{n}}_{*y}$ | −0.907768315504 | $\delta\mathbf{R}_{Sy}$ | 496.816 |
| $\hat{\mathbf{n}}_{Pz}$ | 0.9932184971 | $\hat{\mathbf{n}}_{*z}$ | −0.381818281053 | $\delta\mathbf{R}_{Sz}$ | −765.710 |
| | | $B$ | 25.40253 | | |
| | | $P$ | 6.55076 | | |
| | | $\sin(B)$ | 0.428975 | | |

| Test | Observatory | Feature | Event | UTC[c] |
|---|---|---|---|---|
| PAL#1i | PAL | 1 | Ingress | 6:02:16.5800 |
| MCD#38e | MCD | 38 | Egress | 8:41:12.4041 |

| | PAL#1i | | | MCD#38e | | |
|---|---|---|---|---|---|---|
| | $x$ | $y$ | $z$ | $x$ | $y$ | $z$ |
| $\mathbf{R}_E(t_o)$ | 28105066.005 | −137042688.107 | −59421456.482 | 28379672.424 | −136994800.830 | −59400688.714 |
| $\dot{\mathbf{R}}_E(t_o)$ | 28.802494 | 4.997035 | 2.167107 | 28.792179 | 5.046620 | 2.188628 |
| $\mathbf{R}_{EO}(t_o)$ | −1417.196 | −5138.793 | 3493.535 | 3327.563 | −4379.093 | 3222.955 |
| $\Delta_0/c$ | | 4501.6222 | | | 4501.6318 | |
| $\Delta_1/c$ | | 4501.4048 | | | 4501.6960 | |
| $\Delta_3/c$ | | 4501.6234 | | | 4501.6331 | |
| $t_o$ | | 6:02:16.5800 | | | 8:41:12.4041 | |
| $t_i$ | | 4:47:15.1752 | | | 7:26:10.7081 | |
| $\mathbf{R}_B(t_i)$ | 262638286.457 | −1362110279.554 | −574685125.510 | 262724000.404 | −1362094209.372 | −574682187.060 |
| $\dot{\mathbf{R}}_B(t_i)$ | 8.988949 | 1.685040 | 0.308050 | 8.988850 | 1.685549 | 0.308265 |
| $\mathbf{R}_{BS}(t_i)$ | −242.806 | 130.069 | 11.049 | −249.278 | 118.514 | 12.416 |
| $\dot{\mathbf{R}}_{BS}(t_i)$ | −.000708 | −0.001191 | 0.000145 | −0.000649 | −0.001232 | 0.000142 |
| $\hat{\mathbf{n}}_{*,d}$ | 0.173699397979 | −0.907768317403 | −0.381818282775 | 0.173699433700 | −0.907768311526 | −0.381818280497 |
| $D$ | | 1349549665.438 | | | 1349552316.037 | |
| $\rho$ | −119343.671 | −16603.278 | −148188.553 | 74808.661 | 13586.876 | 1729.846 |
| $\lvert\rho\rvert$ | | 121400.866 | | | 76052.162 | |
| $\epsilon\Delta_1$ | | 18.820 | | | 30.198 | |
| $\mathbf{R}_{SI}(t_i)$ | −130191.304 | 40087.419 | 9026.237 | 78661.323 | −6547.532 | −6738.928 |
| $\lvert\mathbf{R}_{SI}\rvert$ | | 136521.975 | | | 79220.496 | |
| $\lambda_{SI}$ | | 34.65784 | | | 227.02624 | |
| **Planetocentric**[d] | | | | | | |
| $\hat{\mathbf{n}}'_*$ | 0.173729445273 | −0.907762954405 | −0.381817362694 | 0.173729445271 | −0.907762954406 | −0.381817362693 |
| $\Delta_2$ | | 1349486838.123 | | | 1349574098.218 | |
| **Sky-plane**[e] | | | | | | |
| $f$(B1950.0) | | −120337.456 | | | 76029.116 | |
| $g$(B1950.0) | | −16033.276 | | | 1871.645 | |

[a] Except as noted, all calculations have been performed using the Cornell solar-system barycenter vector code, using B1950.0 coordinates. Angles are in degrees, distances are in km, and velocities are in km/sec. See Table VII for additional physical parameters adopted for these tests.

[b] Offsets applied to DE-130.

[c] 3 July 1989 occultation of 28 Sgr by Saturn.

[d] Intermediate results for planetocentric vector calculations.

[e] Final sky-plane coordinates from sky-plane calculations.

ing as given in Table VII, rotating to equatorial coordinates of date, and then reduced to B1950.0 by applying precession and nutation corrections. In practice, we extract the precession and nutation constants from the DE-130 ephemeris; alternatively, one could use the tabulated nutation constants in the *Astronomical Almanac*. As will be seen below, failure to apply nutation results in a few-hundred-meter error in the observer location.

Next, the displacement of Saturn with respect to the Saturn system barycenter is taken into account by interpolation into the satellite ephemeris. Table B-II includes both the positions and velocities of Saturn with respect to the barycenter at the ring intercept time, $t_i$, which can be extended to nearby times using linear extrapolation. Then, the zeroth-order light travel time to Saturn is computed ($\Delta_0/c$), and the iteration loop commences, where the deflected star position, $\hat{\mathbf{n}}_{*,d}$, is

TABLE B-III
Comparison of Barycentric Calculations

| Case | Code[a] | PAL#1i $\lvert R_{SI}\rvert$ (km) | MCD#38e $\lvert R_{SI}\rvert$ (km) | Description |
|---|---|---|---|---|
| 1 | CU | 140383.671 | 75059.271 | geocentric, no barycenter offset, no GR, no $(f_0, g_0)$ |
| | WC | 140383.670 | 75059.272 | |
| | $\Delta R$ | 0.001 | −0.001 | |
| 2 | CU | 140129.800 | 75328.732 | add barycenter offset and spherical GR bending |
| | WC | 140129.799 | 75328.733 | |
| | $\Delta R$ | 0.001 | −0.001 | |
| 3 | CU | 140051.428 | 74525.523 | add $(f_0, g_0)$ ephemeris correction |
| | WC | 140051.432 | 74525.516 | |
| | $\Delta R$ | −0.004 | 0.007 | |
| 4 | CU | 136522.104 | 79220.118 | add topocentric corrections (w/o nutation) |
| | CU | 136521.887 | 79220.205 | add topocentric corrections (w/ nutation) |
| | $\Delta R$ | 0.217 | −0.087 | nutation contribution to topocentric correction |
| 5 | CU[b] | 136521.975 | 79220.496 | add true $J_2$ GR bending |
| | WC[c] | 136521.971 | 79220.490 | |
| | $\Delta R$ | 0.004 | 0.006 | |
| 6 | WC | 136521.971 | 79220.490 | $J_2$ GR bending (Case 5 WC) |
| | WC | 136521.883 | 79220.198 | spherical GR bending ($J_2 = 0$) |
| | $\Delta R$ | 0.088 | 0.292 | $J_2$ contribution to GR bending |
| 7 | CU | 136500.784 | 79189.000 | same as Case 5, but no GR bending |
| | WC | 136500.779 | 79188.993 | |
| | $\Delta R$ | 0.005 | 0.007 | |

[a] Designations for computer codes used for test cases: CU – Cornell University, WC – Wellesley College.
[b] Details are presented in **Table B–II**.
[c] From Fit 12.

used in place of $\hat{\mathbf{n}}_*$ in Eq. (A4) to account for $J_2$ GR bending, and where the ephemeris offset, $(f_0, g_0)$ has been accounted for using Eq. (A15). Intermediate results are given for the closest approach point of the deflected ray to the planet center, and for the total transverse gravitational deflection, $\varepsilon\Delta_1$. The final results of the calculation are the ring plane radii and longitudes, $|\mathbf{R}_{SI}|$ and $\lambda_{SI}$, respectively. For completeness, intermediate results are included in Table B-II for the planetocentric and sky-plane algorithms as well.

## *B.2. Comparison of Independent Barycentric Calculations*

We have developed two independent implementations of the barycentric vector algorithm described in Appendix A. The Cornell University (CU) version, used to produce the test results described above, follows the equations in Appendix A exactly, but it has not been incorporated into a least-squares fitting routine to refine the pole direction, ring radii, or other input parameters. In contrast, the Wellesley College (WC) version is an extension of the code used to determine the orbits of the Uranian rings from both Voyager and Earth-based data (French *et al.*, 1988). This program incorporates both a barycentric vector approach and a sky-plane algorithm, and it was used for all of the fits reported in this work. However, the intermediate quantities computed in the code are not directly comparable to the variables defined in Appendix A. As a test of the two programs, and to determine the sensitivity of the results to changes in the input conditions, we ran several test calculations using the same two points, PAL 1i and MCD 38e. Both programs used identical planetary and satellite ephemerides, star and pole directions, and planetary and geometrical constants; they differed only in the implementation of the barycentric vector algorithm.

Table B-III summarizes each of the test cases and gives the ring intercept radius, $|\mathbf{R}_{SI}|$, as computed by the two programs. For Case 1, we reduced the calculation to the bare essentials, eliminating topocentric corrections, general relativistic bending, displacement of Saturn with respect to the Saturn system barycenter, and ephemeris offsets $(f_0, g_0)$. The CU and WC results are essentially identical, at the 1-m level in the ring plane radius. In Case 2, we included spherical GR bending and the barycenter offset, and in Case 3, we added the ephemeris offset. For these two tests, the largest difference between the CU and WC results was at the 7-m level. Next, we investigated the importance of accounting for nutation in determining the geocentric observer coordinates in B1950.0 coordinates: Case 4 shows that ring plane displacements of 200 m can result from ignoring nutation.

Next, in Case 5, we compared the CU and WC results for a full calculation, including barycenter offsets, $J_2$ GR bending, ephemeris corrections, and topocentric corrections. These are the conditions assumed for all of the fits presented in the main body of this paper. The two codes agree at the 6-m level. Case 6 quantifies the importance of accounting for $J_2$ when computing the GR deflection. Differences of up to 300 m result when one neglects the $J_2$ term, and are largest for the C ring points with the smallest impact parameter at Saturn. The last test (Case 7) is identical to Case 5, except that GR bending is not included. This provides a useful intermediate checkpoint when comparing codes.

When identical input data and geometric conditions are assumed for the CU and WC codes, the results in all cases agree at the 10-m level. This is comparable to the magnitude of special relativistic effects, and is much smaller than the formal error in the derived ring radii of ~1 km (Table X).

TABLE B-IV
Comparison of Barycentric and Sky-Plane Results

| Method | Ephemeris Correction | | Saturn Pole (B1950.0) | | $r$ (km) | |
|---|---|---|---|---|---|---|
| | $f_0$ (km) | $g_0$ (km) | $\alpha_P$(°) | $\delta_P$(°) | #1 | #44 |
| Barycentric[a] | 998.506 | −826.304 | 38.410278 | 83.323535 | 136521.573 | 74490.279 |
| Sky-plane[b] | 998.412 | −826.292 | 38.410174 | 83.323537 | 136521.587 | 74490.305 |
| Difference | 0.094 | − 0.012 | 0.000104<br>0".044 | −0.000002<br>−0".007 | − 0.014 | − 0.026 |

[a] Fit 23, **Table XI**. See text for details.
[b] Same fit conditions as for Fit 23, but sky-plane method used.

### *B.3. Comparison of Barycentric and Sky-Plane Calculations*

In Appendix A, we have shown that the barycentric and sky-plane algorithms should give comparable results to $O(v/c)$, with anticipated differences at the 10-m level ($O(v^2/c^2)$). As a final certification of the correctness of the WC fitting program, we ran Fit 23 using both algorithms. This fit was selected because the barycentric correction for the sky-plane method has been coded to use sky-plane satellite offset positions tabulated in the *Astronomical Almanac*, rather than the 3-D satellite ephemerides used in our adopted solution. The results are compared in Table B-IV, where it is seen that the derived pole direction differs by only 0.048", and fitted ring radii differ by about 20 m, as expected from Appendix A.

### *B.4. Comparison with SW Astrometric Results*

In their accompanying paper, H93 present their independent astrometric analysis of the combined NE and SW sets of 28 Sgr ring observations. The methods adopted by the two groups for the data reduction and the algorithms used in determining the astrometry were entirely independent, but standard solutions using identical input data sets were compared to identify and quantify any systematic differences in our results. The adopted standard test case used by the two groups had the following properties:

1. Each group used its own planetary ephemerides and fitting algorithms. For this test, we used the WC barycentric fitting code, based on the JPL DE-130 ephemerides in B1950.0 coordinates; H93 used the sky-plane method described in their paper and a polynomial interpolation of the apparent Saturn ephemeris published in the 1989 *Astronomical Almanac*, corrected for precession and nutation to J2000.0.

2. The H93 "standard data set" was used: all of the events listed in their Table III, augmented by the timings from PAL, MCD, and IRTF in our Tables III, IV, and V *for the ring features listed in H93 Table I only*. Note that no ESO data were used for this test, and no station offset times were applied to any of the SW data.

3. Ring radii were fixed at NCP values, listed in Table I of H93.

4. The position of 28 Sgr given in our Table VII was adopted. (This differs slightly from the value used by H93 for their final solution.)

5. In both calculations, $J_2$ GR bending, light travel time, and motion of Saturn with respect to the system barycenter were taken into account.

6. Four free parameters were determined from the fit: sky-plane corrections to the planetary ephemeris ($f_0$, $g_0$ in our notation; $\Delta x_E$, $\Delta y_E$ for H93), and the pole direction $\alpha_P$, $\delta_P$. (Since each group used a different planetary ephemeris, one would not expect the sky plane offsets to the planetary ephemeris to agree for the two test cases.)

The results of this test are presented in Table B-V. The independently determined pole directions, precessed to a common epoch (J2000.0), agree to within ~0.84". We have not established how much of this difference is the result of using different planetary ephemerides and how much is due to the actual implementation of the astrometric code. This difference in pole direction is considerably smaller than the error in the pole direction adopted by H93 for their final solution. Nevertheless, this residual disagreement is larger (by a factor of almost 20) than the differences we find between our own sky-plane and barycentric calculations (Table B-IV).

TABLE B-V
Comparison of NE and SW Fitting Algorithms[a]

| Group | $\alpha_P$(J2000.0) | $\delta_P$(J2000.0) |
|---|---|---|
| NE | 40.59526 | 83.53679 |
| SW | 40.59734 | 83.53678 |
| Difference | −0.00208<br>−0".84 | +0.00001<br>+0".04 |

[a] See the text for a detailed description of the fitting conditions and data sets used.

## REFERENCES


ACTON, C. H. JR. 1990. *The SPICE Concept: An Approach to Providing Geometric and Other Ancillary Information Needed for Interpretation of Data Returned from Space Science Instruments*. Report AIAA-90-5082-CP Proceedings of the AIAA/NASA Second International Symposium on Space Information Systems.

ARCHINAL, B. 1992. Terrestrial coordinates and the rotation of the Earth. In *Explanatory Supplement to the Astronomical Almanac* (P. K. Seidelmann, Ed.), pp. 199–277. U.S. Naval Observatory, Washington, DC.

ASTRONOMICAL ALMANAC. Issued by the Nautical Almanac Office, United States Naval Observatory. U.S. Government Printing Office, Washington, DC.

BARON, R. L. 1989. *Occultation Astronomy and Instrumentation: Studies of the Uranian Upper Atmosphere*. Ph.D. thesis, Massachusetts Institute of Technology.

BOSH, A. S., M. L. COOKE, J. L. ELLIOT, R. C. BLESS, M. NELSON, J. W. PERCIVAL, M. J. TAYLOR, G. W. VAN CITTERS, J. F. DOLAN,

AND E. L. ROBINSON 1992. Saturn pole determination using occultation data from the Hubble Space Telescope. *Bull. Am. Astron. Soc.* **24,** 1036.

BRAHIC, A., B. SICARDY, F. ROQUES, C. FERRARI, AND I. GRENIER 1989. Observation of the July 3, 1989 stellar occultation by Saturn and its rings. *Bull. Am. Astron. Soc.* **21,** 951.

BROPHY, T., AND P. A. ROSEN 1992. Density waves in Saturn's rings probed by radio and optical occultation: Observational tests of theory. *Icarus* **99,** 448–467.

BROUWER, D., AND G. M. CLEMENCE 1961. *Methods of Celestial Mechanics*. Academic Press, NY.

BURNS, J. A. 1977. Orbital evolution. In *Planetary Satellites* (J. A. Burns, Ed.), Univ. of Arizona Press, Tucson.

COOKE, M. M. 1991. *Saturn's Rings: Photometric Studies of the C Ring and Radial Variation in the Keeler Gap*. Ph.D. thesis, Cornell University.

COOKE, M. L., A. S. BOSH, J. L. ELLIOT, R. C. BLESS, M. NELSON, J. W. PERCIVAL, M. J. TAYLOR, G. W. VAN CITTERS, J. F. DOLAN, AND E. L. ROBINSON 1992. A stellar occultation by Saturn's rings observed with the Hubble Space Telescope. *Bull. Am. Astron. Soc.* **24,** 1036.

CUZZI, J. N., AND J. D. SCARGLE 1985. Wavy edges suggest moonlet in Encke's Gap. *Astrophys. J.* **292,** 276–290.

DICICCO, D., AND L. J. ROBINSON 1989. Video images of the occultation of 23 Sagittarii by Saturn, July 2–3, 1989. *Bull. Am. Astron. Soc.* **21,** 953.

DUNHAM, E. W., J. L. ELLIOT, A. S. BOSH, L. L. CORDELLA, AND L. A. YOUNG 1989. KAO optical observations of the occultation of 28 Sgr by Saturn. *Bull. Am. Astron. Soc.* **21,** 932.

ELLIOT, J. L., A. S. BOSH, M. L. COOKE, R. C. BLESS, M. NELSON, J. W. PERCIVAL, M. J. TAYLOR, G. W. VAN CITTERS, J. F. DOLAN, AND E. L. ROBINSON 1992. A Saturn ring occultation observed with the Hubble Space Telescope. *EOS Trans., Am. Geophys. U.* **73**(14), 176.

ELLIOT, J. L., E. W. DUNHAM, L. H. WASSERMAN, R. L. MILLIS, AND J. CHURMS 1978. The radii of Uranian rings $\alpha$, $\beta$, $\gamma$, $\delta$, $\varepsilon$, $\eta$, 4, 5, and 6 from their occultation of SAO 158687. *Astron. J.* **83,** 980–992.

ELLIOT, J. L., R. G. FRENCH, J. A. FROGEL, J. H. ELIAS, D. J. MINK, AND W. LILLER 1981. Orbits of nine Uranian rings. *Astron. J.* **86,** 444–455.

ELLIOT, J. L., R. G. FRENCH, K. J. MEECH, AND J. H. ELIAS 1984. Structure of the Uranian rings. I. Square-well model and particle size constraints. *Astron. J.* **89,** 1587–1603.

ESPOSITO, L. W., M. O'CALLAGHAN, AND R. A. WEST 1983. The structure of Saturn's rings: implications from the Voyager stellar occultations. *Icarus* **56,** 439–452.

ESPOSITO, L. W., C. C. HARRIS, AND K. E. SIMMONS 1987. Features in Saturn's rings. *Astrophys. J. Suppl.* **63,** 749–770.

FLYNN, B. C., AND J. N. CUZZI 1989. Regular Structure in the inner Cassini Division of Saturn's rings. *Icarus* **82,** 178–197.

FRENCH, R. G., M. A. CLARK, E. TOLLESTRUP, E. ROBINSON, P. HARVEY, L. HEILMAN, R. FARR, AND R. STIENING 1989. The 3 July 1989 occultation of 28 Sgr by Saturn and its rings: Observations from McDonald Observatory. *Bull. Am. Astron. Soc.* **21,** 928.

FRENCH, R. G., N. J. CHANOVER, M. A. CLARK, E. TOLLESTRUP, AND R. L. BARON 1990. Saturn's rings and atmosphere: Results from the 28 Sgr occultation. *Bull. Am. Astron. Soc.* **22,** 1069–1070.

FRENCH, R. G., J. L. ELLIOT, L. M. FRENCH, J. A. KANGAS, K. J. MEECH, J. E. RESSLER, M. W. BUIE, J. A. FROGEL, J. B. HOLBERG, J. J. FUENSALIDA, AND M. JOY 1988. Uranian ring orbits from Earth-based and Voyager occultation observations. *Icarus* **73,** 349–378.

FRENCH, R. G., J. L. ELLIOT, AND S. E. LEVINE 1986. Structure of the Uranian rings: Ring orbits and widths. *Icarus* **67,** 134–163.

FRENCH, R. G., P. D. NICHOLSON, C. C. PORCO, AND E. A. MAROUF 1991. Dynamics and structure of the Uranian rings. In *Uranus* (J. T. Bergstralh, E. D. Miner, and M. S. Matthews, Eds.), pp. 327–409. Univ. of Arizona Press, Tucson.

GOLDREICH, P. 1965. Inclination of satellite orbits about an oblate precessing planet. *Astron. J.* **70,** 5–9.

HARPER, D., AND D. B. TAYLOR 1993. The orbits of the major satellites of Saturn. *Astron. Astrophys.* in press.

HARRINGTON, J., E. W. DUNHAM, W. J. FORREST, AND J. L. PIPHER 1989. IRTF infrared imaging observations of the occultation of 28 Sgr by Saturn. *Bull. Am. Astron. Soc.* **21,** 954.

HARRINGTON, J., M. L. COOKE, E. W. DUNHAM, W. J. FORREST, J. L. PIPHER, AND J. L. ELLIOT 1991. Saturn ring masses and lightcurve morphology from IRTF observations of the occultation of 28 Sgr. *Bull. Am. Astron. Soc.* **23,** 1778–1779.

HARRINGTON, J., M. L. COOKE, W. J. FORREST, J. L. PIPHER, E. W. DUNHAM, AND J. L. ELLIOT 1993. IRTF Observations of the occultation of 28 Sgr by Saturn. *Icarus,* **103,** 235–252.

HIRSHFELD, A., AND R. W. SINNOTT 1982. *Sky Catalogue 2000.0 Volume 1: Stars to Magnitude 8.0*. Cambridge Univ. Press and Sky Publishing.

HØG, E., AND J. VON DER HEIDE 1976. *Abh. Hamburger Sternw.* **9.**

HOLBERG, J. B. 1982. Identification of 1980S27 and 1980S28 resonances in Saturn's A Ring. *Astron. J.* **87,** 1416–1422.

HOLBERG, J. B., W. T. FORRESTER, AND J. J. LISSAUER 1982. Identification of resonance features within the rings of Saturn. *Nature* **297,** 115–120.

HUBBARD, W. B., AND M. S. MARLEY 1989. Optimized Jupiter, Saturn, and Uranus interior models. *Icarus* **78,** 102–118.

HUBBARD, W., C. PORCO, D. HUNTEN, G. RIEKE, M. RIEKE, E. ASPHAUG, R. CLARK, V. HAEMMERLE, J. HALLER, J. HOLBERG, L. LEBOFSKY, R. MARCIALIS, D. MCCARTHY, B. MCLEOD, M. BUIE, J. ELIAS, D. JEWITT, E. PERSSON, T. BOROSON, S. WEST, R. LANDAU, AND W. SCHUSTER 1989. Preliminary results from the occultation of 28 Sgr by the Saturn system: Saturn. *Bull. Am. Astron. Soc.* **21,** 951.

HUBBARD, W., C. PORCO, R. CLARK, E. TURTLE, V. HAEMMERLE, D. HUNTEN, G. RIEKE, M. RIEKE, J. HALLER, J. HOLBERG, L. LEBOFSKY, R. MARCIALIS, D. MCCARTHY, B. MCLEOD, M. BUIE, J. ELIAS, D. JEWITT, E. PERSSON, T. BOROSON, S. WEST, R. LANDAU, AND L. CARRASCO 1990. Saturn pole position and ring radius scale from 28 Sgr occultation. *Bull. Am. Astron. Soc.* **22,** 1041.

HUBBARD, W. B., C. C. PORCO, D. M. HUNTEN, G. H. RIEKE, M. J. RIEKE, D. W. MCCARTHY, V. HAEMMERLE, R. CLARK, E. P. TURTLE, J. HALLER, B. MCLEOD, L. A. LEBOFSKY, R. MARCIALIS, J. HOLBERG, R. LANDAU, L. CARRASCO, J. ELIAS, M. W. BUIE, S. E. PERSSON, T. BOROSON, S. WEST, AND D. J. MINK 1983. The occultation of 28 Sgr by Saturn: Saturn pole position and astrometry. *Icarus,* **103,** 215–234.

KOZAI, Y. 1957. On the astronomical constants of Saturnian satellite system. *Annu. Tokyo Astron. Obs.* **5,** 73–106.

LANE, A. L., C. W. HORD, R. A. WEST, L. W. ESPOSITO, D. L. COFFEEN, M. SATO, K. E. SIMMONS, R. B. POMPHREY, AND R. B. MORRIS 982. Photopolarimetry from Voyager 2: Preliminary results on Saturn, Titan, and the rings. *Science* **215,** 537–543.

LONGARETTI, P.-Y., AND N. BORDERIES 1986. Nonlinear study of the Mimas 5:3 density wave. *Icarus* **67,** 211–223.

MAROUF, E. A., G. L. TYLER, H. A. ZEBKER, R. A. SIMPSON, AND V. R. ESHLEMAN 1983. Particle size distributions in Saturn's rings from Voyager 1 radio occultation. *Icarus* **54,** 189–211.

MAROUF, E. A., G. L. TYLER, AND P. A. ROSEN 1986. Profiling Saturn's rings by radio occultation. *Icarus* **68,** 120–166.

NICHOLSON, P. D., AND K. MATTHEWS 1991. Near-infrared observations of the Jovian ring and small satellites. *Icarus* **93,** 331–346.

NICHOLSON, P. D., AND C. PORCO 1988. A new constraint on Saturn's zonal gravity harmonics from Voyager observations of an eccentric ringlet. *J. Geophys. Res.* **93,** 10209–10224.

NICHOLSON, P. D., M. L. COOKE, K. MATTHEWS, J. ELIAS, AND G. GILMORE 1990a. Five stellar occultations by Neptune: Further observations of the ring arcs. *Icarus* **87,** 1–39.

NICHOLSON, P. D., M. L. COOKE, AND E. PELTON 1990b. An absolute radius scale for Saturn's rings. *Astron. J.* **100,** 1339–1362.

NICHOLSON, P. D., O. PERKOVIĆ, K. MATTHEWS, AND R. G. FRENCH 1991. Saturn's Rings: optical depth profiles at $\lambda 3.9$ $\mu$m from the occultation of 28 Sgr. *Bull. Am. Astron. Soc.* **23,** 1178.

PORCO, C., W. HUBBARD, D. HUNTEN, G. RIEKE, M. RIEKE, E. ASPHAUG, R. CLARK, V. HAEMMERLE, J. HALLER, J. HOLBERG, L. LEBOFSKY, R. MARCIALIS, D. MCCARTHY, B. MCLEOD, M. BUIE, J. ELIAS, D. JEWITT, E. PERSSON, T. BOROSON, AND S. WEST 1989. Preliminary results from the occultation of 28 Sgr by the Saturn system: Rings. *Bull. Am. Astron. Soc.* **21,** 928.

PORCO, C. C., P. D. NICHOLSON, N. BORDERIES, G. E. DANIELSON, P. GOLDREICH, J. B. HOLBERG, AND A. L. LANE 1984a. The eccentric Saturnian ringlets at 1.29Rs and 1.45Rs. *Icarus* **60,** 1–16.

PORCO, C. C., G. E. DANIELSON, P. GOLDREICH, J. B. HOLBERG, AND A. L. LANE 1984b. Saturn's nonaxisymmetric ring edges at 1.95Rs and 2.27Rs. *Icarus* **60,** 17–28.

PORCO, C. C., AND P. D. NICHOLSON 1987. Eccentric features in Saturn's outer C Ring. *Icarus* **72,** 437–467.

ROSEN, P. 1989. *Waves in Saturn's Rings Probed by Radio Occultation.* Ph.D. thesis, Stanford University.

ROSEN, P., G. L. TYLER, E. A. MAROUF, AND J. J. LISSAUER 1991. Resonance structures in Saturn's rings probed by radio occultation II. Results and interpretations. *Icarus* **93,** 25–44.

SANDEL, B. R., D. E. SHEMANSKY, A. L. BROADFOOT, J. B. HOLBERG, G. R. SMITH, J. C. MCCONNELL, D. F. STROBEL, S. K. ATREYA, T. M. DONAHUE, H. W. MOOS, D. M. HUNTEN, R. B. POMPHREY, AND S. LINICK 1982. Extreme ultraviolet observations from the Voyager 2 encounter with Saturn. *Science* **215,** 548–553.

SHOWALTER, M. R. 1991. Visual detection of 1981S13, Saturn's eighteenth satellite, and its role in the Encke gap. *Nature* **351,** 709–713.

SHOWALTER, M. R., J. N. CUZZI, E. A. MAROUF, AND L. W. ESPOSITO 1986. Satellite "wakes" and the orbit of the Encke Gap moonlet. *Icarus* **66,** 297–323.

SHU, F. 1984. Waves in planetary rings. In *Planetary Rings* (R. Greenberg, A. Brahic, Eds.), pp. 513–561. Univ. of Arizona Press, Tucson.

SICARDY, B., F. ROQUES, AND A. BRAHIC 1991. Neptune's rings, 1983–1989: Groundbased stellar occultation observations. *Icarus* **89,** 220–243.

SIMPSON, R. A., G. L. TYLER, AND J. B. HOLBERG 1983. Saturn's pole: Geometric correction based on *Voyager* UVS and radio occultations. *Astron. J.* **88,** 1531–1536.

SMART, W. M. 1977. Occultations and eclipses. In *Textbook on Spherical Astronomy,* pp. 368–403. Cambridge Univ. Press, Cambridge.

SMITH, B. A., L. A. SODERBLOM, R. BATSON, P. BRIDGES, J. INGE, H. MASURSKY, E. SHOEMAKER, R. BEEBE, J. BOYCE, G. BRIGGS, A. BUNKER, S. A. COLLINS, C. HANSEN, T. JOHNSON, J. MITCHELL, R. TERRILE, A. COOK, J. CUZZI, J. POLLACK, E. DANIELSON, A. INGERSOLL, M. DAVIES, G. E. HUNT, D. MORRISON, T. OWEN, C. SAGAN, J. VEVERKA, R. STROM, AND V. SUOMI 1982. A new look at the Saturn system: The Voyager 2 images. *Science* **215,** 504–537.

SMITH, B. A., L. SODERBLOM, R. BEEBE, J. BOYCE, G. BRIGGS, A. BUNKER, S. A. COLLINS, C. HANSEN, T. JOHNSON, J. MITCHELL, R. TERRILE, M. CARR, A. COOK, J. CUZZI, J. POLLACK, G. E. DANIELSON, A. INGERSOLL, M. DAVIES, G. HUNT, H. MASURSKY, E. SHOEMAKER, D. MORRISON, T. OWEN, C. SAGAN, J. VEVERKA, R. STROM, AND V. SUOMI 1981. Encounter with Saturn: Voyager 1 imaging results. *Science* **212,** 163–191.

STANDISH, E. M. JR. 1987. *Jet Prop. Lab. Interoffice Memo* **314.6-891.**

STANDISH, E. M. JR. 1990. The observational basis for JPL's DE 200, the planetary ephemerides of the Astronomical Almanac. *Astron. Astrophys.* **233,** 252–271.

STANDISH, E. M. JR., X X NEWHALL, J. G. WILLIAMS, AND D. K. YOEMANS 1992. Orbital ephemerides of the sun, moon, and planets. In *Explanatory Supplement to the Astronomical Almanac* (P. K. Seidelmann, Ed.), pp. 279–323. U.S. Naval Observatory, Washington, DC.

TAYLOR, G. E. 1983. I.A.U. Commission 20 working group on the prediction of occultations by satellites and minor planets, Bulletin 30, 1983, Feb. 21.

TYLER, G. L., E. A. MAROUF, R. A. SIMPSON, H. A. ZEBKER, AND V. R. ESHLEMAN 1983. The microwave opacity of Saturn's rings at wavelengths of 3.6 and 13 cm from Voyager 1 radio occultation. *Icarus* **54,** 160–188.

WARD, W. R. 1975. Tidal friction and generalized Cassini's laws in the solar system. *Astron. J.* **80,** 64–70.

WARD, W. R. 1981. Orbital inclination of Iapetus and the rotation of the Laplacian plane. *Icarus* **46,** 97–107.